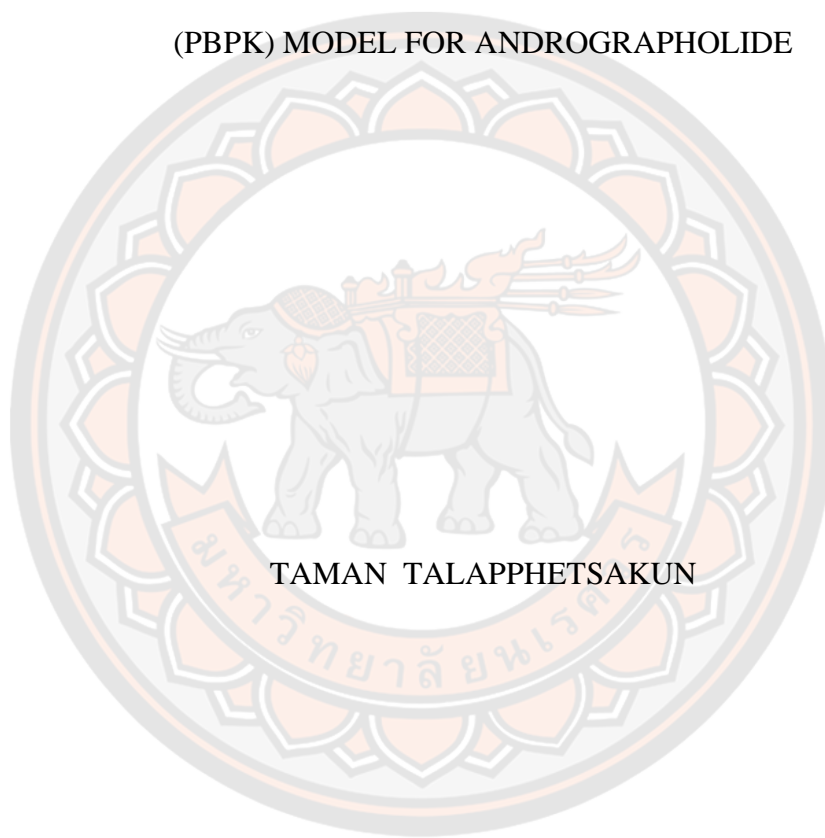DEVELOPMENT OF PHYSIOLOGICALLY-BASED PHARMACOKINETIC
(PBPK) MODEL FOR ANDROGRAPHOLIDE

TAMAN TALAPPHETSAKUN

A Thesis Submitted to the Graduate School of Naresuan University
in Partial Fulfillment of the Requirements
for the Master of Science in Pharmacology
2022

DEVELOPMENT OF PHYSIOLOGICALLY-BASED PHARMACOKINETIC (PBPK) MODEL FOR ANDROGRAPHOLIDE

TAMAN TALAPPHETSAKUN

A Thesis Submitted to the Graduate School of Naresuan University
in Partial Fulfillment of the Requirements
for the Master of Science in Pharmacology
2022

Thesis entitled "Development of Physiologically-Based Pharmacokinetic (PBPK)
Model for Andrographolide"

By TAMAN TALAPPHETSAKUN

has been approved by the Graduate School as partial fulfillment of the requirements

for the Master of Science in Pharmacology of Naresuan University

Oral Defense Committee

.... Chair
(Assistant Professor Siriluk Jaisue, Ph.D.)

.... Advisor
(Professor Jarupa Viyoch, Ph.D.)

.... Co Advisor
(Assistant Professor Pakawadee Sermsappasuk, Ph.D.)

.... Internal Examiner
(Assistant Professor Sarawut Oo-puthinan, Ph.D.)

                                          Approved

                         ....
                         (Assistant Professor Krongkarn Chootip, Ph.D.)

                              Dean of the Graduate School

Title	DEVELOPMENT OF PHYSIOLOGICALLY-BASED PHARMACOKINETIC (PBPK) MODEL FOR ANDROGRAPHOLIDE
Author	TAMAN TALAPPHETSAKUN
Advisor	Professor Jarupa Viyoch, Ph.D.
Co-Advisor	Assistant Professor Pakawadee Sermsappasuk, Ph.D.
Academic Paper	M.S. Thesis in Pharmacology, Naresuan University, 2022
Keywords	Andrographolide, Pharmacokinetics, Physiologically Based Pharmacokinetic (PBPK) model, COVID-19, SARS-CoV-2

ABSTRACT

The coronavirus disease 2019 (COVID-19) that is caused by the severe acute respiratory syndrome coronavirus 2 (SARS-CoV-2) has become an urgent crisis of global health. Andrographolide is a major natural compound found in a Thai plant namely *Andrographis paniculata* (Burm.f.) Wall. Ex. Nees. This phytochemical has been demonstrated a potent antiviral effect for COVID-19 treatment. A present, the *in vivo* studies of andrographolide regarding the anti-SASR-CoV-2 effect are still invisible. The purpose of this study was to develop a physiologically based pharmacokinetic (PBPK) animal model using available published data. Additionally, the model was further scaled up to humans to predict andrographolide concentrations in the lungs. This is significant because it may be critical to demonstrate an appropriate dosage regimen of andrographolide for COVID-19 treatment. The developed PBPK model with perfusion-limited assumption comprised of five tissue compartments including lung, liver, fat, slowly perfused organ and rapidly perfused organ. The feature of the developed PBPK model was integrating hepatic UGT2B7-mediated metabolism in the mouse liver. The Michaelis-Menten equation with the extrapolated maximum velocity of 626.5 mmol/h was used to describe the metabolism in humans. The saturation of the metabolism occurred after multiple oral receiving 12 g q 8 h of andrographolide that could not be used therapeutically. Using Monte Carlo simulation, most of the simulated subjects who orally receiving of 200 mg q 8 h andrographolide could provide a free drug at a steady state over the reported IC_{50}

value against SARS-CoV-2 in the lungs for the majority of healthy humans. Based on the reported CC_{50} value, the toxicity did not occur at the therapeutic dosage. Once additional data, the PBPK would be needed to recalibrate to gain understanding in a dose-response relationship and optimization of dosage regimens of andrographolide. Last, our developed model also featured a preliminary assess the possible herb-drug interaction based on the EMA guideline and the US FDA criteria. The model predicted could imply that the possible interaction caused by andrographolide is unlikely to appear after multiple oral administrations of 1400 mg.

ACKNOWLEDGEMENTS

I would like to express my deep gratitude to the Center of Excellence for Innovation in Chemistry (PERCH-CIC) for providing me with a great opportunity to pursue my Master's degree in the Faculty of Pharmaceutical Sciences, Naresuan University.

I would like to express my deepest appreciation to my advisor Professor Jarupa Viyoch who was generous in helping me to have the opportunity to do this project and my co-advisor Assistant Professor Dr. Pakawadee Sermsappasuk who was the contributor of academic knowledge, generously giving valuable advice and self-study approach. I could not have succeeded in finishing my thesis and taken on the journey to be a researcher without her help and advice.

I would like to give special thanks to the committee members Assistant Professor Dr. Sarawut Oo-Puthinan and the external committee Assistant Professor Dr. Siriluk Jaisue who sacrificed precious time to give good advice honestly and gave me some constructive criticism. My special thanks would be given to Miss. Ya Kimheang and Miss Pajaree Mongkhon gave me good advice regarding modelling, moral support, and writing academic knowledge.

I wish to deeply appreciations to my parents for their unconditional love, the best encouragement, advice, and support. Over the course of almost half a decade, they sacrificed their body and soul to drive me to success. There is no greater love than the parents' love. I appreciate every obstacle that keeps pushing me down so that I can learn to get up and keep going. I would like to give special thanks to a wonderful girl who stood by my side in good times and bad times. She is like the nectar that will nourish my mind when weary. Lastly, I would like to express my gratitude to Phra Rattanatri, may all benefactors always stay safe everywhere.

TAMAN TALAPPHETSAKUN

TABLE OF CONTENTS

Page

CONTENT OF TABLE

Page

CONTENT OF FIGURE

CHAPTER I

INTRODUCTION

Statement of purpose

Currently, coronavirus disease 2019 (COVID-19) has been caused by severe acute respiratory syndrome coronavirus 2 (SARS-CoV-2) and has been an urgent crisis of global health. COVID-19 has produced severe diseases including severe acute respiratory syndrome (SARS) and the Middle East respiratory syndrome (MERS) (1). More than one million deaths caused COVID-19 globally at the end of December 2020 (2) and more than 2 million deaths since the outbreak began. At present, the effective drugs or vaccines against this virus are not successfully developed (1, 3, 4).

Andrographolide is a major bioactive constituent in *Andrographis paniculata* Burm.f Wall. Ex. Nees *A.paniculata*, which is widely found in Southeast Asia and India (5, 6) . Various studies have shown it to possess many promising pharmacological properties including being an antipyretic, anti-inflammatory, antioxidant, antihyperglycemic, antimalarial, antitumor, antifertility, cardio-protective, and hepatoprotective agent (7-15). The interested pharmacological potential of purified andrographolide (Andro) is anti-virus such as influenza virus, human immunodeficiency virus (HIV), severe acute respiratory syndrome coronavirus 1 (SARS-CoV-1), especially, SARS-CoV-2 (1, 16, 17). In 2020, there is a few studies reported that Andro has a promising future in the treatment of the COVID-19 (18, 19). Main protease (M^{pro}) is essential for the life cycle of SARS-CoV-2. Since it plays an important role in the production of functional polyproteins required for viral replication. Andro can directly inactive the SARS-CoV-2 viral replication through the M^{pro} inhibition (19). Using SARS-CoV-2 infected human lung epithelial cells (Calu-3), the viral replication and viral release of SARS-CoV-2 have been relatively high inhibited by Andro when compared to remdesivir which is a current drug for SARS-CoV-2 treatment (20, 21). The half-maximal inhibitory concentration (IC_{50}) of Andro for the inhibition of the production of infectious virions was 0.034 μM with the

selectivity index value of 380 (20). Despite Andro demonstrated a relatively high against SARS-CoV-2 potential in *in vitro* studies, the treatment of COVID-19 in *in vivo* still needs to prove.

According to the outbreak of COVID-19 and a rapidly increasing number of infected COVID-19 patients in Thailand, the Department of Thai Traditional and Alternative medicine recommends the use of either *A. paniculata* powder or *A. paniculata* extract for COVID-19 treatment. In the asymptomatic COVID-19 patients, the recommended dose is equivalent to Andro 60 mg q 8 h for 5 days in a row (22). Recently, only one published clinical trial of Andro in humans is found. In small clinical trials in humans, Andro has been demonstrated to benefit HIV-positive patients (17) but did not benefit patients with active progressive multiple sclerosis (23) and symptomatic adenomyosis (24). The dosages of Andro in the clinical trials were between 2-10 mg/kg/day. However, no evidence of the efficacy and safety of *A. paniculata* extract or Andro in patients with COVID-19 has been published. The dosage regimen of Andro in patients with COVID-19 is still unknown. In order to design an appropriate dosage regimen of Andro for COVID-19 treatment, the understanding of the pharmacokinetics of Andro, especially the uptake of Andro from plasma into the lung which is a target site of SARS-CoV-2 infection is important.

Base on *in vitro* and animal studies, Andro has low oral bioavailability (9, 25, 26) and might be passively transported through the gastrointestinal tract (27-30). The low solubility profiles (31, 32), efflux by P-glycoprotein (25, 26), and high intestinal-first pass metabolism of Andro (25, 26) might contribute to low oral bioavailability of less than 10% (9, 25, 33). The unbound fraction of Andro in plasma can distribute into several organs such as the heart, lung, liver, kidneys, spleen, and brain (25, 34, 35). Andro might be mainly metabolized in the liver while approximately 10% of the unchanged form of Andro is eliminated *via* the kidneys in rats following oral administration of *A. paniculata* extract (36). UGT2B7 has been the major enzyme involved in Andro metabolism in mice, beagle dogs, and humans (37) while the major metabolism enzyme in rats is still unclear. The saturation of Andro metabolism was observed in healthy Thai volunteers after oral intakes of *A. paniculata* extract tables at a high dose which is equivalent to 88.56 mg of Andro

(38), however, the study regarding the saturation of form of Andro metabolism is not still conducted.

There are many approaches to predict the dosage regimen in the clinical study such as a dose-by-factor method, a pharmacokinetically-guided method, and a similar drug method (39). Unfortunately, the dosage regimen of Andro could be not predicted using such methods due to lack of the published information on Andro relating to *in vivo* data including the no observed adverse effect levels (NOAEL) and pharmacological activity dosages (PAD). The pharmacokinetic/pharmacodynamics (PK/PD) modeling method has been a useful tool for dosage regimen prediction. However, the prediction of drug levels in the target organ seemed to be beyond the limitation (39).

A physiologically based pharmacokinetic) PBPK (model has been an alternative approach to predict the dosage regimen to save time and cost in animal studies (40, 41). The PBPK model is an *in-silico* study that consists of a series of differential equations based on *in vitro* and *in vivo* pharmacokinetic data, physiology and anatomy, physicochemical properties, and drug biological properties (42, 43). Pharmacodynamic parameters (e.g., IC_{50}, EC_{50}, GI_{50}, MIC, and MEC) might reflect the mechanism of action as well as the biomarker mechanisms. It is essential in building a mechanism-based PBPK model (44). It is important to note that the PBPK model can predict the plasma and tissue drug concentration-time profiles. This model can be used to design a dosage regimen to maintain drug concentrations above the threshold of efficacy but below the anticipated threshold for adverse effects (44). Therefore, this study aims to develop a PBPK model of Andro using *in vitro* and *in vivo* data to understand tissue distribution of Andro before scaling it up from animals to humans. Additionally, the ultimate goal of this study is to predict Andro concentration in the lung for preliminary determination of the appropriate dosage regimen for COVID-19 treatment.

Research aims

1. To develop a physiologically based pharmacokinetic (PBPK) model of Andro in animals using *in vitro* and *in vivo* from published data.

2. To evaluate the developed model with the independent dataset and extrapolate the model from animals to humans.

3. To apply the developed model to predict the appropriate dosage regimen for COVID-19 treatment and other indications.

Research significance

Although several *in vitro* and animal studies have shown several promising pharmacological properties of Andro, the dosage regiment of Andro and clinical studies on pharmacokinetics in humans are still unknown. Therefore, this study aimed to create a PBPK model of Andro to predict plasma and tissue concentration-time courses as well as the pharmacokinetics of Andro in animals and humans. Additionally, the developed PBPK model is applied to predict appropriate dosages regimen based on the threshold theory leading to a better therapeutic outcome. Last, this model can also be applied to preliminary assess the possible herb-drug interaction caused by Andro.

Research scope

This study was *in silico* experiment that was performed on a computer. The PBPK model was developed based on *in vitro* and *in vivo* information relating to pharmacokinetic studies. The ADAPT5 software (version 5.0.58) was used to develop a PBPK model of Andro for understanding the pharmacokinetics in animals and humans. Last, the appropriate dosage regiment of Andro was designed using the developed PBPK model.

Keywords

Andrographolide; Pharmacokinetics; Physiologically based pharmacokinetic (PBPK) model; tissue distribution; COVID19; SARs-CoV-2; simulation; metabolism

CHAPTER II

LITERATURE REVIEWS

Andrographis paniculata (Burm.f.) Wall. Ex.Nees., (Family Acanthaceae) (Thai name Fa-Tha-lai-Chon; Namlai Pangpon; Sam Sip Di, English name-King of Bitters, Tamil name-Nalavempu) is an annual herbaceous plant (45). According to the Thai herbal pharmacopeia 2018, this plant can grow up to 1 high meter, is erect and its stem is acutely quadrangular. Its leaves are simple, opposite, glabrous, lanceolate, 2 to 12 cm long, 1-3 cm wide, acute, and entirely slightly undulating. The inflorescence is terminal and axillary in the panicle, 10-30 mm long with small bracts and short pedicels. The flowers are calyx-5-partile, small, and linear. The corolla tubes are narrow (about 6 mm long), bilabiate, the limbs are not shorter than the tubes, the upper lip is oblong and white with a yellowish top, and the lower lip is broadly cuneate, 3-lobed (trifid), and white with violet markings. Two stamens are inserted in the throat and are another basally bearded. The ovary is superior, 2-celled, with a far exerted style. The fruit capsule is erect, linear-oblong, 1-2 cm long, compressed, and longitudinally furrowed on broad faces with thin glandular hairs. The seeds are very small (45, 46).

Figure 1 Illustration of *A*. *paniculata* (Burm.f.) Nees; (1) flowering and fruiting plant, (2) difference views of flowers (a-d), (3) fruits in different stages (e), and dehiscent fruit showing seeds (f)

Source: Adapted from Thai herbal pharmacopeia, (46)

World Health Organization (WHO) monographs on selected medicinal plants have reported, *A*. *paniculata* being used as a medicinal plant in many countries. This plant has responded to many pharmacological activities (6). In addition, *A*. *paniculata* has been used to treat many diseases including the common cold, gastroenteritis, infectious diseases, and inflammatory lung diseases (i.e., asthma). These have also been supported by clinical data from WHO monographs on selected medicinal plants (6, 47) and a review by Shahid Akbar et al. (48). Moreover, two reviews have reported *A.paniculata* as a safe and efficacious plant to relieve the symptoms of upper respiratory tract infection (URTI) (49, 50). The possible mechanisms of action have been described in previous studies by Shahid Akbar et al. (48) and Kuntal Maiti et al. (47, 51).

Currently, *A*. *paniculata* extract has been used in varying dosage forms in China as shown in Table 1. According to Indian pharmacopeia, there were 26 Ayurvedic formulations (45). In Thailand, the dried part of *A*. *paniculata* powder (crude drug) has been made into Andrographis capsules. There were four dosages, including 250, 300, 350, and 500 mg available. Administration of 0.5 to 2 g of Andrographis capsules four times per day after meals and at bedtime has been used

for antidiarrheal treatment. In addition, administration of 0.75 to 1.5 g four times a day after the meal and at bedtime has been used for laryngitis treatment (46).

Table 1 Summary of the current dosage forms of *A. paniculata* in China

Country	Name	Dosage form	Reference
China	Kan Jang		(45)
	Chuanxinlian	Tablets	
	Xiaoyan Lidan		
	Chuanxinlian antiphologistic	Pills	
	Yamdepieng		
	Chuanxinlian Ruangs	Injection	

A. paniculata has been shown to contain diterpene, diterpenoid lactone, flavonoid, alkanes, ketone, and aldehydes. More than 12 flavonoids and 14 diterpenoids have been found in the aerial part (46, 52-54), but only 7 diterpenoids (free and glycoside forms) were major phytoconstituents (55-57). However, there have been only four major active diterpenoid lactones, including (1) andrographolide, (2) 14-deoxy-11, 12-didehydro-andrographolide, (3) neoandrographolide, and (4) deoxy-andrographolide (31, 58).

Andro was a major diterpenoid lactone that drove a broad range of pharmacological activities of *A. paniculata* (59). Powdered crude drugs from the aerial parts of *A.paniculata* contained not less than 6% diterpenoid lactones, calculated as Andro (6, 60). In addition, the leaves of *A.paniculata* contained 2.5-3.0% w/w of Andro (61).

Physicochemical properties

Andrographolide is a diterpenoid lactone as shown in Figure 2. It consisted of three hydrogen bond donors and five hydrogen bond acceptors with molecular weight (MW) 350.45 g/mole (62). Andro was considered a neutral compound since its solubility does not change significantly in a pH range (63). Besides, this diterpenoid was a lipophilic compound since it's the logarithms of the partition coefficient between n-octanol and water (log P) equal to 2.51 (64) and low water solubility (32).
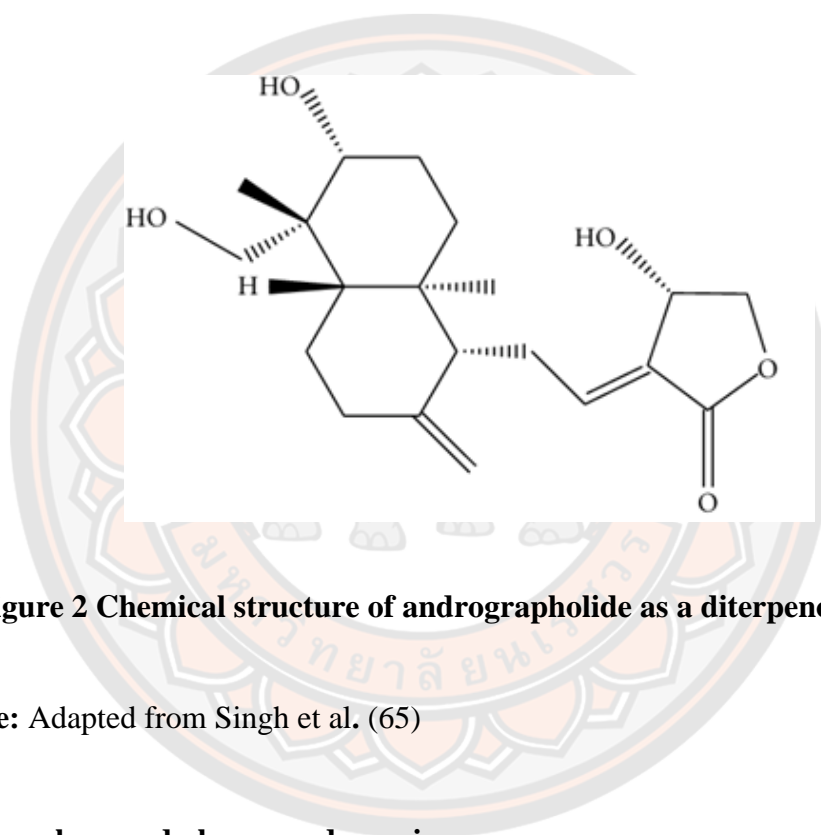
Figure 2 Chemical structure of andrographolide as a diterpenoid lactone

Source: Adapted from Singh et al**.** (65)

Pharmacology and pharmacodynamic

Andro has been a diterpenoid lactone with various pharmacological effects. The studies related to the pharmacological activities, mechanism of action, and pharmacodynamic (PD) parameters of Andro were retrieved from three databases to design the appropriate dosage regiment. The pharmacological activity detail of Andro (Standard andrographolide >98%) was described below and summarized in Table 2.

  1. **Anti-SARs-CoV-2 activity**

Currently, coronavirus disease 2019 (COVID-19) has been caused by severe acute respiratory syndrome coronavirus 2 (SARS-CoV-2) and has been an urgent crisis of global health. Whilst the effective vaccines against this virus are not

successfully developed (1, 3, 4). COVID-19 has produced severe diseases including severe acute respiratory syndrome (SARS) and the Middle East respiratory syndrome (MERS) (1).

Coronaviruses have been a single-stranded positive-sense RNA virus and can infect terrestrial animals and humans (3, 4). This virus is classified into the β-coronavirus group and has 80-96% similar genomic of SARS-CoV (1, 4). The main protease (M^{pro}) is the viral protease that plays an important role in the production of functional polyproteins required for viral replication. Therefore, M^{pro} is essential for the life cycle of SARS-CoV-2. Besides, this protease has been no human homolog of proteins exists. Hence, M^{pro} inhibition becomes to be a target-based therapeutics and an effective treatment for SARs-CoV-2 (1). Although HIV protease inhibitors, including lopinavir and ritonavir, have been used against SARS-CoV-2, it has limited efficacy in COVID-19 treatment and caused adverse effects, including gastrointestinal intolerance, and hepatoxicity (1).

According to Shi et al., Andro suppressed the activities of SARS-CoV and SARS-CoV-2 with IC_{50} of 5.00 ± 0.67 µM and 15.05 ± 1.58 µM, respectively. Whilst disulfiram (SARS-CoV M^{pro} inhibitor) had shown the inhibition on SARS-CoV-2 M^{pro} with IC_{50} of 5.61 µM. These results suggested that it could be beneficial against COVID-19 (1). Based on a plaque assay, *A. paniculata* extract, Andro, and remdesivir significantly inhibited the production of infectious virions with IC_{50} of 0.036 µg/mL, 0.034 µM, and 0.086 µM, respectively in SARS-CoV-2 infected the lung epithelial (Calu-3) cells (20). The IC_{50} and CC_{50} values have been illustrated in Table2. However, the application of Andro on COVID-19 treatment must further investigate in the clinical trials (1).

2. Anti-influenza A virus activity

The influenza A virus has been a cause of respiratory disease that generates high morbidity and mortality rates in either animals or humans. The high pathogenicity H5N1 influenza A virus could transmit from birds to humans. At present, the mechanism of action against the influenza virus of the current drugs has been divided into three major classes such as M2 ion channel inhibitors, neuraminidase inhibitors, and inosine monophosphate dehydrogenase inhibitors (66). Currently, the new functions of the sphingolipid signaling/metabolism during virus

infection have been uncovered. The virus could increase the level of sphingosine kinase (SK) 1 for progeny virus. The mechanism involves the regulation of NF-κB signaling pathways. This resulting to the amplification of influenza viral RNA synthesis and production of viral ribonucleoprotein (RNP) complex. Thus, NF-κB inhibitor might be an alternative way to design a new drug (67).

Based on a plaque reduction assay, Andro exhibited low effectiveness against H9N2, H5N1, and H1N1 viral activities with IC$_{50}$ values of 94.30, 121.70, and 110.00 µM, respectively (Table 2). The mechanism of action was not involving with blocking viral binding to red blood cells but involves inhibition NF-κB activation by binding to the reduced cysteine 62 of p50, thus, inhibiting the binding of NF-κB to DNA. However, the new synthesized compound namely 14-α-lipoyl- Andro showed high potent against H9N2, H5N1, and H1N1 viral activities with IC$_{50}$ values of 8.40, 15.20, and 7.20 µM, respectively. Whereas a positive control (ribavirin) showed the effect of anti-H9N2, H5N1, and H1N1 activities with IC$_{50}$ values of 30.00, 42.90, and 39.60 µM, respectively. The mechanism of action of 14-α-lipoyl- Andro is hypothesized that it may act by i) inhibiting NF-κB activation, and ii) blocking H9N1, H5N2, and H1N1 viral binding to red blood cells with MIC value of 7.10, 16.80, and 5.30 mM, respectively (66).

3. Anti-HIV activity

The human immunodeficiency virus (HIV) has been grouped into the genus Lentivirus within the family of Retroviridae. The complex protein-protein interactions have been characterized as the initial steps of infection of a cell. When the gp120, a surface glycoprotein that plays a role of attachment the virus to the target cell, binds to the CD4 receptor on the host cell, all CD4-positive cells (e.g., T-helper cells, macrophages, dendritic cells, and astrocytes) are susceptible to HIV. After attachment to the CD4 molecule, a conformational change in CD4 and gp120 will occur, resulting in increasing of the site for gp120 to enable binding to the co-receptors on the cell surface. When binding of gp-120 to CD4 completely, the virus can insert into the plasma membrane of the target cell. If the fusion of cell membranes and viral envelop, the infection process is completed (68). Base on *in vitro* study, Andro inhibited gp120- mediated cell fusion of HL2/3 cells and TZM-bl cells with an IC$_{50}$ value of 0.59 µM while the IC$_{50}$ value of suramin has been 0.04 µM (69). The

therapeutic index (TI) value 2875 suggested was considered a relatively safe compound when TI value greater than 10 (16). The IC_{50}, CC_{50}, and TI_{50} values has been shown in Table 2. In a small clinical trial, Andro exhibited the potential increase of the mean CD4 lymphocyte levels in 13 HIV subjects following oral administration of 10 mg/kg Andro (17). In such experiments, this compound could be regarded as a compound to develop new molecules for anti-HIV treatment.

4. Immunomodulatory

T cell-mediated immune responses play a role against tumors. Of several subsets of T cells, cytotoxic T lymphocytes (CTL) play a critical role in the immune system and protection from tumors (70). Intraperitoneal administration of 0.2 mg/kg Andro in mice significantly increased the CTL production in both *in vitro* and animal models. The life span (%ILS) of tumor induced EL4 cells mice was increased to 64.2% by Andro when compared to a control group. Besides, the treatment of Andro with 10 doses also increased %ILS from 35.8% to 77.4%. Based on animal studies, Andro exhibited the enhancement of cytokines including interleukin-2 and interferon-γ. Hence, Andro may be considered to further develop as an alternative anti-tumor growth agent (70).

5. Anti-platelet activation

Base on *in vitro* studies, the IC_{50} values ranging from 1 to 100 µM in a concentration-dependent manner (58, 71, 72) as shown in Table 2. Whilst, the PAF-antagonists including Ginkgo extract and Aspirin were 2 and 177 µM respectively (71, 73). Lu et al. reported that Andro has dilated the blood vessels *via* stimulation of eNOS expression, nitric oxide (NO) releasing, and vasodilator-stimulated phosphoprotein (VASP) phosphorylation, respectively. Otherwise, when eNOS was simulated by Andro, the cyclic GMP will be increased and result in two ways of inhibiting platelet aggregation. First, the cyclic GMP has inhibited PLCγ2 and IP3, respectively. Next, the dense tubular system (DTS) was inhibited to release calcium (Ca^{2+}) and, finally, inhibited platelet aggregation. Second, the cyclic GMP has inhibited and PI3 kinase/Akt cascades and p38 MAPK, respectively. Next, the catalyzing arachidonic acid (AA) and thromboxane A2 (TxA_2) were inhibited, resulting in reducing Ca^{2+} levels and platelet aggregation (58, 71, 72, 74). The hypothetical mechanism was shown in Figure 3. Further, Andro was not only

effective in *in vitro* studies but also in an animal study. Base on animal studies, Andro reduced the mortality rate in adenosine diphosphate; ADP-induced acute pulmonary embolism mice from 90% to 60-50% at dose 22-55 µg/kg intravenously (58). Besides, Andro could protect the cardiovascular by down-regulation of the inducible nitric oxide synthase (iNOS), which is the cause of reactive oxygen species (ROS) generation, endothelial dysfunction, and inflammation, expression, and up-regulate of eNOS expression in hyperlipidemia-rats following oral administration of 25-100 mg/kg Andro for five consecutive days (75).
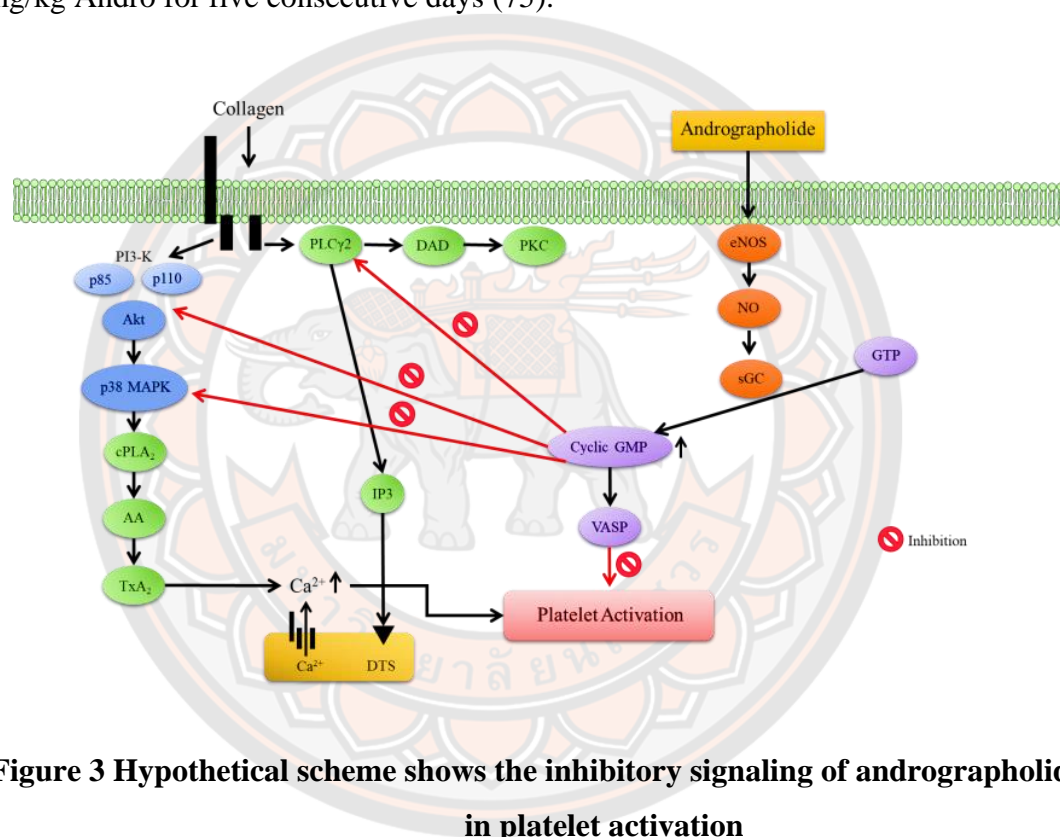
Figure 3 Hypothetical scheme shows the inhibitory signaling of andrographolide in platelet activation

Abbreviation: PLCɤ2 is phospholipase C gamma 2; DAG is diacylglycerol; PKC is protein kinase C; IP3 is inositol triphosphate; AA is arachidonic acid; TxA2 is thromboxane A2; sGC soluble guanylate cyclase; VASP vasodilator-stimulated phosphoprotein (plays a role in negatively regulating secretory and adhesive events in platelet cells), DTS dense tubular system**.**

Source: Adapted from Lu et al. (58)

6. Anti-hyperglycemia activity

Type 2 diabetes mellitus is a chronic metabolic disorder characterized by high blood sugar, insulin resistance, and a relative lack of insulin (76). Based on *in vitro* studies, Andro can be an alternative candidate for the management of type 2 diabetes mellitus. The α-glucosidase and α-amylase are inhibited by Andro with IC_{50} values of 31.39 mM and 2.24 mM, respectively (Table 2). Whilst the acarbose, which is a current anti-diabetic drug, has been inhibiting the α-glucosidase and α-amylase with IC_{50} values of 9.60 and 23.08 mM (77). The possible mechanism of action in the anti-hyperglycaemic activity of Andro has consisted of four pathways including decreasing glucose absorption (77, 78), increasing insulin secretion (79), increasing glucose uptake into the muscle (80), and prevention of insulin resistance (79, 81).

7. Anti-malaria activity

Malaria is a disease caused by *Plasmodium* parasites that are transmitted to humans and other animals by bites from the female Anopheles mosquitoes (82). Based on *in vitro* and animal studies, Andro has shown good anti-malaria activity (11, 83, 84). Andro has been against the erythrocytic stages of *Plasmodium falciparum* with an IC_{50} value of 9.1 μM while the artesunate, which is a medication used to treat malaria, has an IC_{50} value of 0.05 μM (11). Besides, Andro has been found anti-malaria activity as blood schizontocial activity and gametocytocidal with IC_{50} values of 34.70 and 10.30 μM respectively (84). Their values were shown in Table 2. In malaria mice infected by *Plasmodium berghei*, alone Andro administration *via* intraperitoneal daily, the parasitemia level is detected as 46% and 33% for artesunate administration. Whilst, all the mice died after attaining the parasitemia level 80% in the control group (11). In addition, orally dosing of 5 mg/kg Andro in mice also produced significant ($p<0.05$) inhibition as ~72.7%. Whilst, chloroquine produced 100% inhibition at the dose of 10 mg/kg (83). Based on the analysis of the docking study, Andro may be a protease inhibitor against malaria parasites (85).

8. Anti-inflammatory activity

Nitric oxide (NO) has been a pro-inflammatory mediator that plays a role in the pathogenesis of inflammation. Over-production of NO in abnormal situations had induced inflammation. The high concentration of NO caused by the inducible nitric oxide synthase (iNOS) could generate the pathogenesis of inflammatory

disorders of the joints, gut, and lung. Selective NO biosynthesis inhibitors which inhibit the iNOS have been considered as an alternative to inflammatory therapy (86). Based on *in vitro*, Andro has inhibited NO synthesis by reducing the expression of the iNOS protein with IC_{50} value of 7.9 µM in a concentration-dependent manner (87, 88). Whilst the IC_{50} value of diclofenac sodium, a reference drug, has been 0.02 µM (89). In those studies, the hypothetical mechanisms of action were prevention of the *de novo* protein synthesis and decreasing the protein stability *via* a post-transcriptional mechanism. Besides, Andro inhibited tumor necrosis factor-α (TNF-α) and granulocyte-macrophage colony-stimulating factor (GM-CSF) which are the non-specific and allergic inflammatory cytokines with IC_{50} value of 0.6 µM and 3.3 µM respectively in a concentration-dependent manner (90). In animal studies, Andro significantly (p<0.05) inhibited the elevation of bronchoalveolar fluid (BAF) levels of TNF-α and GM-CSF in asthmatic mice following intraperitoneal injection 3-30 mg/kg/day (90). Further, Andro attenuated ovalbumin-induced lung tissue eosinophilia and airway mucus production, mRNA expression of E-selectin, chitinases, Muc5ac, and iNOS in lung tissues, and airway hyperresponsiveness to methacholine at dose 0.1-1 mg/kg intraperitoneally (91). Table 2 has been a summary of anti-inflammation efficacy parameters. In such evidence, Andro may use as an important therapeutic advance in the management of inflammatory disorders.

9. Anti-microbial activity

Globally, over 50% of all deaths in hospitals were caused by infectious diseases (92) and multiple drug resistance among the human pathogenic microorganisms had increased due to widespread and indiscriminate use of common antimicrobial drugs against infectious diseases, results in limited therapeutic options (93). *Staphylococcus aureus* (*S. aureus*) has causes a mostly intravascular catheter-related bacteremia and endocarditis that represents a challenging situation for clinical management (94). Based on *in vitro* study, Andro exhibited the potential against six-gram positives and three-gram negative microbial activities. The minimal inhibition concentration (MIC) of Andro has shown in Table 2. Among those, *Staphylococcus aureus* (*S. aureus*) was found to be most sensitive with a minimal inhibitory concentration value of 0.10 µM which was identified as bacteriostatic (95). Whilst, the IC_{50} values of amoxycillin, ampicillin, cefatazime, and gentamicin have been 32,

32, 8, and 8 µM, respectively (96). Besides, specific inhibition of intracellular DNA biosynthesis and the biofilm formation of *S. aureus* were decreased by Andro in a concentration-dependent manner (95). Andro might be considered as a promising lead for new antibacterial drug development (95).

10. Anti-pyretic and analgesic

In Asian countries, *A.paniculata* has been widely used for its antipyretic and analgesic effect (59). Based on an animal study, intraperitoneal administration of 4 mg/kg Andro in Baker's yeast-induced fever rats did not significantly produce antipyretic activity. Whilst intraperitoneal administration of 4 mg/kg Andro in mice significantly produces the analgesic effect and reduces paw volume which represents an anti-inflammatory effect (97). Those results were in line with a published by Lin et al. (98). In the writing test (analgesic effect), the male mice were fed Andro at 25, 50, 100 mg/kg before intraperitoneal injection of 0.8% acetic acid solution to induce the pain. Next, the mice were kept in individual cages to observe and record the number of writhing and stretching movements. The results showed that oral dosing of 25, 50, and 100 mg/kg Andro in mice significantly reduced the number of writes in a dose-dependent manner. Whereas morphine, which is commonly used as a positive control, at 5 mg/kg demonstrated a high analgesic effect. In order to investigate the anti-edema effect, the rats were included edema using carrageenan injection. The rats were intraperitoneally injected with Andro at 50, 75, 100 mg/kg while another group was received 10 mg/kg of indomethacin which is a commercial anti-inflammatory drug. The results showed that the prevention of paw edema of Andro was observed at a high dose (100 mg/kg) while 10 mg/kg indomethacin could prevent rats from edema (98).

11. Anti-fertility

In ancient Indian literature, several plants have been reported to have fertility-regulating properties and tested the ant-fertility activity in laboratory animals (66). Oral administration of 25-50 mg/kg/day Andro in rats for 48 days reduced spermatogenesis, degenerative changes in the seminiferous tubules, regression of Leydig cells, and regressive and/or degenerative changes in the epididymis. This study also confirms that Andro might be used for male contraception (13).

12. Anti-cancer activity

Despite the discovery of numerous drugs of natural origin, searching for new anticancer agents has been necessary to provide a drug that is less toxic as well as more effective (66). Base on *in vitro* studies, various cancer cells such as breast MCF-7/ADR cells, Colon SW 620 cells, Lung H22, Ovarian SK OV3, Prostate DU145, and Renal A498 were inhibited by Andro (99) as summarized in Table 2. Besides, cell proliferation and migration, as well as cell cycle arrest at G2/M phase of HepG2 human hepatoma cells, were inhibited by Andro with an IC_{50} value of 40.2 μM after 48 h treatment (100). In that published, Andro also induced apoptosis through a capase-independent pathway (100). Using human endothelial cells, the E-selectin, which plays an important role in cancer cell adhesion to endothelial cells, activity was significantly reduced and inhibited the E-selectin mRNA expression. These results leading to the suppression of the adhesion of gastric cancer cells (101). Base on animal study, seven cell lines were moderately inhibited activity by Andro at 50 mg/kg and good activity at 100 mg/kg dose (99).

13. Hepatoprotective

Liver diseases are still a serious health problem and a major cause of mortality. Herbs and plants play a vital role in managing several liver disorders while reliable hepatoprotective drugs in modern medicine have absented. In Ayuravate medicine, *A.paniculata* has long been used as a hepatoprotective agent (59). A recent study showed that Andro, which is a major bioactive in *A.paniculata*, attenuated concanavalin A (Con-A)-induced liver injury and inhibited hepatocyte apoptosis in mice at intraperitoneal dose 30-500 mg/kg in a dose-dependent manner (102, 103). Oxidative stress has generated several chronic human diseases such as cardiovascular disease, cancer, neurodegenerative diseases as well as liver diseases. When the balance between antioxidation and oxidation was disrupted, oxidative stress will be generated. Under this condition, the reactive oxygen species (ROS) were over-generated, resulting in the oxidation of cellular macromolecules and damage to cellular functions (9). There has been 4 inherent antioxidant defense system including vitamin E, glutathione (GSH), vitamin C, and antioxidant enzymes (9). Based on animal study, oral dosing of 30-50 mg/kg/day Andro for 5 consecutive days up-regulated several antioxidant enzymes including superoxide dismutase (SOD)-1,

heme oxygenase (HO)-1, and glutathione (GSH) S-transferase (GST) in liver, heart, and kidney. The activity of SOD, GST, and GSH reductase enzymes was also increased in rats (9). Besides, pre-treatment of 30-50 mg/kg Andro suppressed carbon tetrachloride (CCI$_4$)-induced plasma aminotransferase activity and hepatic lipid peroxidation. Those results suggested that Andro protects chemical-induced oxidative damage by up-regulating the activity of antioxidant enzymes in various tissues (9).

14. Anti-hyperlipidemia

A high level of low-density lipoproteins (LDL) can cause plaque to grow over time and develop obstructions in blood flow. If obstruction occurred in the coronary arteries and the brain could result in a heart attack and a stroke respectively (59, 104). Andro has reduced the triglyceride, total cholesterol, and LDL level while high-density-lipoproteins (HDL) were increased in hyperlipidemia-mice following oral dosing of 25-100 mg/kg (75, 105). These findings imply the promising use of Andro as an alternative to anti-hyperlipidemia.
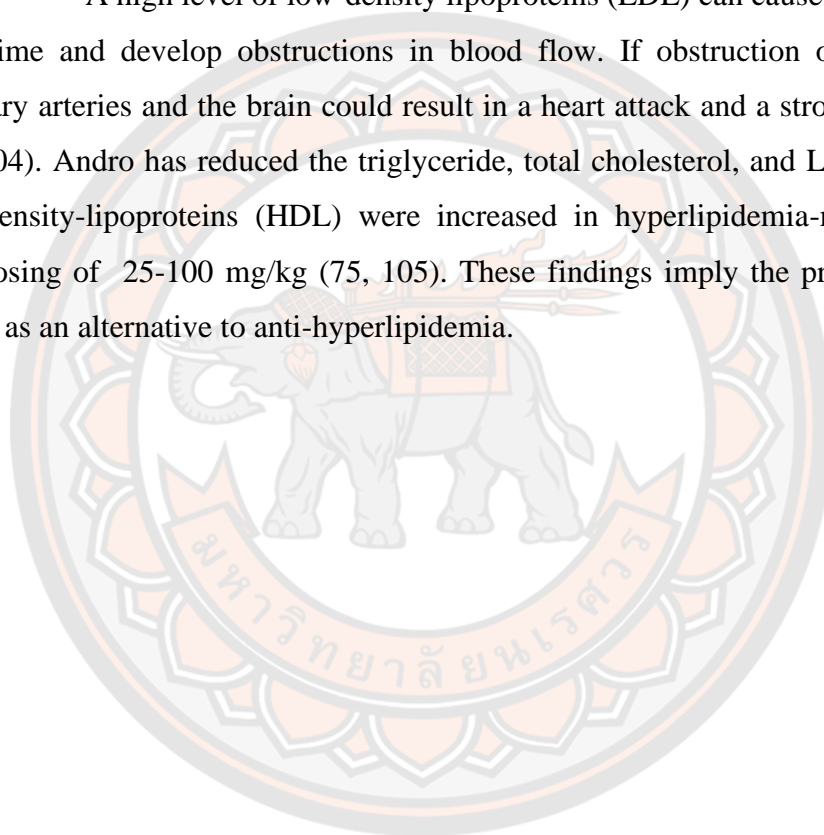
Table 2 Summary of pharmacological activities as well as pharmacodynamic parameters

Pharmacological activity	Experimental model	Results	Reference
Anti-SARs-CoV-2	*In vitro* - Cleavage assay using BL21 *E. coli* strain as a model	- Andro suppressed the activity of SARs-CoV-2 with IC_{50} of 15.05 µM. A possible mechanism of action is inhibition of protease namely M^{pro}.	(1)
	In vitro - Plaque assay using Calu-3 cells as a model	- Andro inhibited the production of infectious virions with IC_{50} of 0.034 µM.	(20)
Anti-influents viral	*In vitro* H9N2, H5N1, and H1N1 virus cultured in Madin Darby canine kidney (MDCK) cells	- Low anti-H9N2, H5N1, and H1N1 virus with EC_{50} values of 94.3, 121.7, and 110.0 µM, respectively. - CC_{50} value reported as 3085 µM, so the selective index (SI) for H9N2, H5N1, and H1N1 virus were 33, 25, and 28, respectively. - MIC values for H9N2, H5N1, and H1N1 virus on viral binding to Chicken RBCs were 236, 294, and 308 µM respectively, which indicated low.	(66)
	In vivo Mice infected by H9N2, H5N1, and H1N1 virus	- Low protection to mice infected with influenza H9N2 and H5N1 virus following oral dosing 500-2000 mg/kg/day for 7 days. A 90% and 70% survival rate were achieved after infection with the A/H1N1 virus at 500 and 1000 mg/kg/day for 7 days respectively.	

Pharmacological activity	Experimental model	Results	Reference
	In vitro	- Inhibited gp120-mediated cell fusion of HL2/3 cells (expressing gp120 on its surface) with TZM-bl cells (expressing CD4 and co-receptors CCR5&CXCR4).	
	- TZM-bl cells	- CC_{50}, IC_{50}, and IT value equal 1696, 0.59 µM, and 2875, respectively.	(16)
	- HL2/3 HeLa derived cells	- CC_{50}: The cytotoxic concentration of the compound leading to a 50% reduction in cell viability.	
		- IC_{50}: Inhibitory concentration of the compound leading to 50% inhibition in HIV infection.	
		- TI: Therapeutic Index, (CC_{50}/IC_{50})	
Anti-HIV	Clinical trial		
	- 13 HIV positive patients	- Significantly increase of the mean $CD4^+$ lymphocyte levels in HIV subjects following oral dosing of 10 mg/kg Andro.	(17)
	- 5 HIV uninfected (healthy volunteers)		
	- Dose: 5, 10, 20 mg/kg (po t.i.d.)		

Pharmacological activity	Experimental model	Results	Reference
Immunomodulatory	*In vivo* - Winn's Neutralization Test in BALB/c mice - Dose: 0.2 mg/kg (i.p.)	- Increased antibody production. - Decreased delayed-type hypersensitivity response.	(70)
Anti-platelet	*In vitro* Rat platelet	- Inhibited rat platelet aggregation with IC_{50} values ranging from 1 to 100 µM.	(72)
		- Inhibited human platelet aggregation with an IC_{50} value of 5 µM in a dose-dependent manner.	(71)
	In vitro Human platelet	- Inhibited human platelet aggregation with an IC_{50} value of 35 µM.	(58)
		- Decreased Platelet-activating factor (PAF). - Increased eNOS-NO/cyclic GMP pathway. - Decreased PLCγ2-PKC and PI3 Kinase/Akt-MAPKs.	(58) (74)
Anti-hyperglycemia	*In vitro* - Porcine α-amylase Yeast α-glucosidase	- Inhibited α-amylase with IC_{50} value of 31.4 mM. - Inhibited α- glucosidase with IC_{50} value of 32.2 mM.	(77)

Pharmacological activity	Experimental model	Results	Reference
Anti-hyperglycemia	*In vivo* - Alloxan-induced diabetic mouse Dose: oral single 50 mg/kg	- Increased insulin secretion from pancreatic β-cells plays a role in insulin secretion. - Decreased NF-κB in insulin secretion, resulting in the prevention of insulin resistance.	(79)
	In vivo - STZ-induced diabetic rats Dose: oral single 1.5 mg/kg	- Increased glucose uptake into muscle by an increment in the glucose transporter (GLUT4) production, resulting in decreased blood glucose level.	(80)
	In vitro Chloroquine resistant strain of *Plasmodium falciparum*	- Inhibited parasites activity with IC_{50} value of 9.1 µM.	(11)
Anti-malaria	*In vitro* - Not available	- Inhibited *Plasmodium falciparum* activity as blood schizontocial activity and gametocytocidal with IC_{50} values of 34.70 and 10.30 µM, respectively.	(84)
	In vivo - Mice infected by *Plasmodium berghei* Dose: single intraperitoneal 50 mg/kg	- The parasitemia level was detected as 46% and 33% respectively.	(11)

Pharmacological activity	Experimental model	Results	Reference
	In vitro RAW 246.7 macrophages stimulated with LPS plus IFN-γ	- Inhibited NO synthesis by reducing the expression of iNOS protein with the IC$_{50}$ value of 17.4 μM. - Mechanism: (1) prevention of the *de novo* protein synthesis and (2) decreasing the protein stability *via* a post-transcriptional mechanism.	(87)
	In vitro Macrophage cells	- Suppressed NO production in a concentration-dependent manner in the concentration range from 0.1-100 μM. - Inhibited NO production with IC$_{50}$ value of 7.9 μM.	(88)
Anti-inflammatory	*In vitro* Macrophage cells	- Inhibited TNF-α and GM-CSF releasing (induced by LPS) in a concentration-dependent manner. - IC$_{50}$ values were 0.6 μM and 3.3 μM for TNF-α and GM-CSF respectively.	(90)
	In vitro - Human cell lines of transformed embryonic kidney 293 cells - Promyeloid cells	- Decreased NF-κB *via* the covalent modification of reducing Cys62 of p50 with IC$_{50}$ value of 15 μM. - Decreased TNF-α with an IC$_{50}$ value of 10 μM in a dose-dependent manner.	(106)

Pharmacological activity	Experimental model	Results	Reference
	In vivo - Male ICR mice Dose: 5-50 mg/kg/day (p.o.)	- Andro did not significantly reduce NO production in mice following oral dosing of 5-50 mg/kg/day Andro.	(88)
	In vivo - Asthmatic mice Dose: 3-30 mg/kg/day (i.p.)	- Significantly inhibited the elevation of bronchoalveolar fluid (BAF) levels of TNF-α and GM-CSF in a dose-dependent manner.	(90)
Anti-inflammatory	*In vivo* - Female BALB/c mice sensitized and challenged with ovalbumin (OVA) developed airway inflammation Dose: 0.1-1 mg/kg (single i.p.)	- Attenuated OVA-induced lung tissue eosinophilia and airway mucus production, mRNA expression of E-selectin, chitinases, Muc5ac, and iNOS in lung tissues, and airway hyperresponsiveness to methacholine.	(91)

Pharmacological activity	Experimental model	Results	Reference
		- Against three gram-negative bacterial strains including *Escherichia coli* AG100A, *Escherichia coli* D22, and *Klebsiella pneumoniae* ATCC 33495 with MIC values of 0.250, 0.125, and 1.00 µM, respectively.	
Anti-microbial	*In vitro* - 21 bacterial strains	- Against six gram-positive bacterial strains including *Staphylococcus aureus* MTCC 96, *Staphylococcus aureus* ATCC BAA 1717, *Streptococcus pneumoniae* ATCC 49619, *Streptococcus pneumoniae* ATCC BAA 255, *Enterococcus faecalis* ATCC 29212, *Bacillus subtilis* ATCC 27370 with MIC values of 0.10, 1.00, 0.250, 0.500, and 0.250 µM, respectively. - Decreased biofilm formation by *S. aureus* MTCC96 with concentration-dependent manner.	(95)

Pharmacological activity	Experimental model	Results	Reference
	In vivo - Writhing test in male ICR mice (analgesic) - Carrageenan-induced paw edema test in rats (anti-inflammation effect)	- Andro decreased the number of writhes at oral doses 25, 50, and 100 mg/kg in a dose-dependent concentration. - Andro at 100 mg/kg showed significant prevention the paw edema.	(98)
Anti-pyretic and analgesic	*In vivo* - Baker's yeast-induced fever test in rats (antipyretic effect) - The hot plate test in male ICR mice (analgesic) - Writhing test in male ICR mice (analgesic) Carrageenan-induced paw edema test in rats (anti-inflammation effect)	- Andro did not significantly (p <0.05) produce antipyretic activity in rats following intraperitoneal injection of 4 mg/kg. - Andro significantly (p <0.05) produce an analgesic effect in mice following intraperitoneal injection of 4 mg/kg. - Andro did not reduce the writhing response at dose 4 mg/kg i.p. - Andro was shown to significantly reduced paw volume at dose 4 mg/kg i.p.	(97)

Pharmacological activity	Experimental model	Results	Reference
Anti-fertility	*In vivo* - Albino Rats - Dose: 25-50 mg/kg/days for 48 days (p.o.)	- Decreased spermatogenesis. - Decreased degenerative changes in the seminiferous tubules, regression of Leydig cells, and regressive and/or degenerative changes in the epididymis, seminal vesicle. - Decreased ventral prostate, and coagulating glands.	(13)
	In vitro Mouse myeloid leukemia cell line	- Increased Cell differentiation.	(107)
Anti-cancer	*In vitro* - Breast MCF-7/ADR cells - CNS U251 cells - Colon SW620 cells - Lung H522 - Ovarian SK OV3 - Prostate DU145 Renal A498	- Decreased various Proliferation of cancer cells. - The concentration for 50% of maximal inhibition of cell proliferation (GI_{50}) values for Breast MCF-7/ADR, CNS U251, Colon SW620, Lung H522, Ovarian SK OV3, Prostate DU145, and Renal A498 cells were 15, 3, 10, 17, 15, 20, and 30 µM respectively.	(99)

Pharmacological activity	Experimental model	Results	Reference
	In vitro HepG2 human hepatoma cells	- Inhibited cell proliferation, migration, and cell cycle arrest at G2/M phase of HepG2 cells with IC$_{50}$ value of 40.2 μM after 48 h treatment.	(100)
	In vitro Human endothelial cells	- Reduced E-selectin expression of activated endothelial cells and inhibited the E-selectin expression mRNA level, resulting in suppression of the adhesion of gastric cancer cells.	(101)
Anti-cancer	*In vivo* - Hollow fiber assay in Swiss Albino mice	- Against 7 cell lines with moderate activity at 50 mg/kg and good activity at 100 mg/kg doses.	(99)
	A review	- Decreased Janus tyrosine kinases-signal transducers and activators of transcription, phosphatidylinositol 3-kinase and NF-κB signaling pathways, suppression of hsp 90, cyclins, and cyclin-dependent kinases, MMPs, and growth factors.	(108)
Anti- hyperlipidemia	*In vivo* - Hyperlipidemia-mice Dose: 25-100 mg/kg (p.o.)	- Reduced TC, TG, and LDL. - Increased HDL.	(75, 105)

Pharmacological activity	Experimental model	Results	Reference
	In vivo - Hepatitis-induced concanavalin A (Con-A) mice - Dose: 62.5, 125, 250, and 500 mg/kg (i.p.)	- Significantly decreased enzymatic from tissues homogenate including glutamate oxaloacetate transaminase (GOT), glutamate pyruvate transaminase (GPT) acid phosphatase (ACP), alkaline phosphatase (ALP), and lipid peroxidation (LP) at dose 500 mg/kg (i.p.).	(102)
Hepatoprotective	*In vivo* - Hepatitis-induced concanavalin (Con-A) mice	- Andro prevents Con-A-induced liver injury and reduced the hepatic oxidative stress response at doses 30-100 mg/kg in a dose-dependent manner.	(103)

Toxicity

In a previous study, Andro did not produce cytotoxic effects on human platelets. In this lactate dehydrogenase (LDH) study concentrations of Andro between 35 and 150 µM did not produce any toxicity or cytolysis in human platelets (58). In addition, the cytotoxicity profiles of Andro were evaluated by MTT assay using six human cell lines. The 50% cytotoxic concentration (CC_{50}) values of Andro on liver cells (HepG2), kidney cells (HK-2), intestine cells (Caco-2), lung cells (Calu-3), and brain cells (SH-SY5Y) were 81.52, 34.11, 52.30, 58.03, and 13.19 µM, respectively. The selectivity index (SI), which was a ratio that measures the window between cytotoxicity, was calculated from CC_{50} values divided by IC_{50} value. The higher SI values suggested a higher anti-viral effect with low cytotoxicity. Considering the anti-SAR-CoV-2 effect with the IC_{50} of 0.034 µM Andro, this diterpene lactone showed the considerably low-to-no cytotoxic effect on HepG2, HK-2, Caco-2, Calu-3, and SH-SY5Y cells with SI values of 2398, 1003, 1538, 1707, and 388 respectively (20).

Andro is practically non-toxic even at high doses. In an acute toxicity test in male and female mice by Bothiraja et al. oral doses greater than 5 g/kg oral dose did not produce death or hazardous signs. This LD_{50} level of Andro by oral treatment was greater than 5 g/kg body weight in mice (109). According to the Hodge and Sterner toxicity scale, a chemical substance with an LD_{50} value greater than 5 g/kg is considered practically non-toxic (110).

In sub-acute tests in Wistar rats, 250 and 500 mg/kg (LD_5 and LD_{10}) of Andro did not result in significant changes in body weight gain, food intake, behavior, mortality, hematological, biochemical, vital organ weight, and histopathology. Therefore, Andro was recommended for clinical testing as a pharmaceutical agent (109). A summary of Andro toxicity is shown in Table 3.

Table 3 Summary of toxicity of Andro

Dosage/duration/route	Experimental models	Toxic effects	References
25-75 µM	Human platelets	No cytotoxicity	(58)
10 mg/kg for 3 weeks	Human	No	(111)
5 g/kg single oral dose	Mice	No	
250-500 mg/kg orally for 21 days	Rats	No	(109)

Pharmacokinetics

The *in vitro, in situ,* and *in vivo* information related to the pharmacokinetic properties of Andro (Standard andrographolide >98%) was collected and summarized from several international sources. In this section, the pharmacokinetics of Andro was divided into four main parts including Absorption, Distribution, Elimination, and Interaction & drug-metabolizing enzymes.

1. Absorption

Andro was relatively quickly absorbed into the systemic circulation after a single oral administration of *A. paniculata* extract and Andro at T_{max} less than 140 min in animals and humans as shown in Table 4. Based on an *in situ* study, the highest absorption site of Andro was the duodenum jejunum followed by the ileum and colon (26). These results were in line with previous studies by Ye et al (25) and Yen et al. (112, 113). Andro might be passively transported thorough the gastrointestinal tract because the saturation of absorption was not observed in a parallel artificial membrane permeability (PAMPA) assay. In accordance with Daodee et al. (30), Andro exhibited passive transportation across the artificial membrane at pH 2 and 7. The time course of Andro transport across the artificial membrane (Figure 4) exhibited the cumulative amount of Andro increased with time in a zero-order fashion. Also, when the initial concentrations of Andro were increased, the transport rate of Andro increased almost in a parallel fashion. Whereas, the transport rate

constant of Andro was constant among pH 7 and 2 of medium (Table 5) because Andro was an unchanged neutral compound (30). Besides, Andro also retained a neutral charge in a pH range lower than 10 (114). Although a study conducted by Yang et al. reported the temperature could affect the transportation of Andro using Caco-2 cells and suggested transport of Andro was mediated by the carrier and energy need to be consumed (26), the study regarding to the uptake transporters of Andro is still lack.
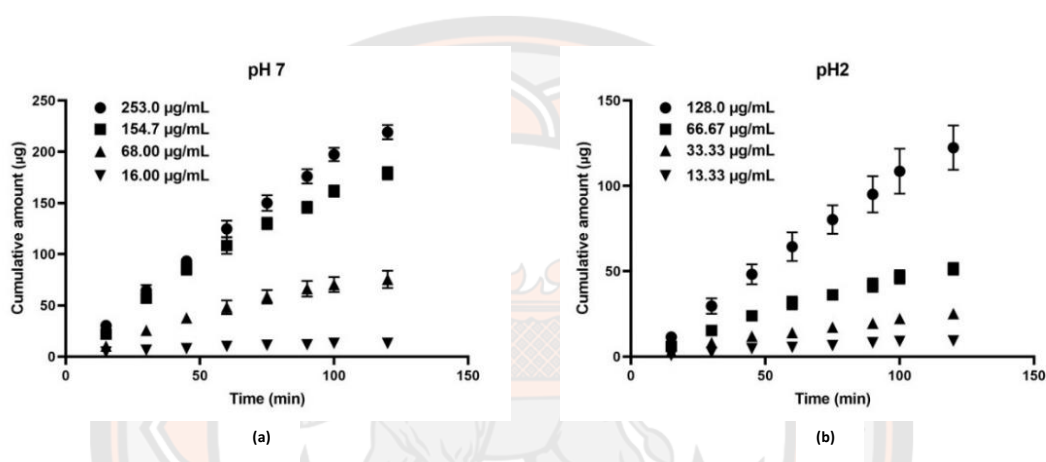
Figure 4 Transport profile of andrographolide from the simulated; (a) intestinal fluid which pH7 and (b) gastric fluid which pH2 across an artificial membrane. Each value represents the mean ±SD (n=3)

Source: Adapted from Daodee et al. (30)

Table 4 Pharmacokinetic parameters after single oral administration of *A. paniculata* extract and Andro

Species	Dose (µmol)	Formulation	C_{max} (µM)	T_{max} (min)	Author (year)
***A. paniculata* extract suspension administration**					
Wistar rats	2.4 (mg)	Suspended in water	3.62 ± 0.6	144.6 ± 9.00	Panossian *et al.* (2000) (36)
	24 (mg)	Suspended in water	8.56 ± 1.7	100.2 ± 18.0	
Andro solution administration					
Wistar rats	11.41	Water	0.15 ± 0.03	66.6 ± 13.80	Ma *et al.* (2018) (115)
Wistar rats	11.41	Solvent is unknown	0.04 ± 0.01	233.3 ± 127	Chen *et al.* (2018) (116)
Wistar rats	20.55	Solvent is unknown	0.33 ± 0.05	45.00 ± 17.4	Bera *et al.* (2014) (35)
Wistar rats	85.60	20% (w/w) β-cyclodextrin aqueous	0.66 ± 0.14	29.75 ± 0.50	Ye *et al.* (2011) (25)
Andro suspension administration					
Wistar rats	3.21	0.5% sodium carboxymethy cellulose	4.62 ± 0.31	59.69 ± 3.61	Suo *et al.*(2007) (117)
Wistar rats	4.99	Suspension (Solvent is unknown)	2.38 ± 0.86	30.00 ± 2.40	Parveen *et al.* (2014) (118)
Wistar rats	6.28	0.3% carboxymethyl cellulose	2.37 ± 0.14	60.00 ± 3.60	Chellampillai *et al.* (2011) (119)

Species	Dose (μmol)	Formulation	C_{max} (μM)	T_{max} (min)	Author (year)
Andro suspension administration					
Wistar rats	12.48	0.3% carboxymethyl cellulose	19.38 ± 1.54	150.00	Maiti et al. (2018) (115)
Sprague Dawley rats	14.27	Distilled water	5.91 ± 0.77	61.67 ± 14.72	Ren et al. (2009) (120)
Sprague Dawley rats	27.39	Solvent is unknown	0.22 ± 0.06	28.75 ± 12.00	Qiao et al. (2017) (29)

Table 5 The transport rate constant of andrographolide at varying pH and initial concentrations

	Transport rate ($\mu g/min^{-1}$)	Initial concentration($\mu g/mL$)
Intestinal fluid	0.094 ± 0.0017	16.0
(pH 7)	1.757 ± 0.0058	253.0
Gastric fluid	0.077 ± 0.0018	13.3
(pH 2)	1.053 ± 0.1134	128.0

Source: Adapted from Daodee et al. (30)

Despite Andro was rapidly absorbed in the intestine (26), the absolute oral bioavailability (F_{oral}) in animals is very low (12) (9, 25). Based on pharmacokinetics studies, the F_{oral} values were 9.27% and 0.03, 1.19, and 2.67% in mice and rats respectively (9, 12, 25, 112). Whilst the F_{oral} value in humans has been unknown. Four factors might contribute to low F_{oral} of Andro including (i) low solubility, (ii) intestinal chemical instability, (iii) efflux transport, and (iv) high first-pass metabolism.

The parameters of permeability and solubility have been allowed by the biopharmaceutical classification system (BCS) to predict intestinal drug absorption (121). Andro has been high permeability (25, 26, 29). The flux of Andro from the apical side (AP) to the basolateral side (BL) in a Caco-2 cell monolayer had high. Based on Caco2-cell experiments, the appearance permeability (P_{app}) values were less than 8×10^{-6} cm/s (25, 26, 29). This result was suggested completely intestinal absorption when the P_{app} value larger the 1.0×10^{-6} cm/s (70%-100% absorbed) (27, 28). The summary of P_{app} for Andro from AP to BL and from BL to AP was shown in Table 6. Andro has demonstrated low solubility because dose solubility volumes (DSV) of Andro are greater than 250 mL (DSV = dose in mg/solubility in mg/mL at 37 °C) (28). Meili Chen et al. reported that the water solubility of Andro was 1.86×10^{-1} mmol/L (0.065 mg/mL) at 35 °C and pH 7 (32). According to USP and BP solubility criteria, Andro has also been demonstrated as sparingly soluble, as

solubility has ranged from 30 to 100 parts of solvent required/part of solute (121).In addition, a dissolution test of Andro from *A. paniculata* capsule in three physiologically relevant media revealed that Andro dissolved most at pH 6.8 (86.92% at 100 minutes and 65.40% at 30 minutes) and lowest at pH 4.5 (75.31% at 100 minutes and 61.70% at 30 minutes) (31). In addition, the dissolution test of Andro standard exhibited a maximum of 30% release in four hours (122). Although Andro has been high permeability (25, 26, 29), it also low solubility (31, 32), thus, it might be classified as BCS class II. Hence, the low F_{oral} of Andro might be limited by its solvation rate.

Table 6 Summary of the permeability (P_{app}) of Andro from the apical side (AP) to the basolateral side (BL) and from BL to AP

In vitro model	P_{app} (cm/s)		Efflux Ratio	Reference
	AP $\rightarrow$ BL	BL $\rightarrow$ AP	$P_{app,BL \rightarrow AP}/P_{app,AP \rightarrow BL}$	
Caco2-cell	1.14×10^{-5}	4.94×10^{-5}	4.33	(25)
MDR1-MDCKII cell	5.93×10^{-6}	23.8×10^{-6}	4.01	
Caco2-cell	7.99×10^{-6}	45.5×10^{-6}	5.70	(26)
Caco2-cell (Andro + VER)	16.9×10^{-6}	18.2×10^{-6}	1.07	
Caco2-cell	1.69×10^{-6}	-	-	(29)

The MDR1-MDCKII cells were Madin–Darby canine kidney II cells overexpressing human P-gp; VER was Verapamil (P-gp inhibitor)

Chemical instability in low pH media might be one cause of very low F_{oral} values in animals. Zhao et al. reported that Andro remained neutral when the pH was lower than 9. The recovery of Andro was satisfactory (>85%) over the pH range of 5.0 to 8.0. Thus, when pH was above 9, Andro was recovered less due to hydrolysis of the lactone ring under basic conditions. In addition, Andro was recovered

minimally in pH less than 4 due to the dehydration of allyl alcohol (114). These results were in line with a degradation study conducted by Chanchal et al. (123).

Andro was effluxed *via* P-glycoprotein (P-gp). In a Caco-2 cell model, the P_{app} value of Andro from BL to AP was higher than the P_{app} value from AP to BL by about 4.0 to 5.7-fold (25, 26) as shown in Table 6. These results indicated efflux transporters were involved when the efflux ratio was larger than 1.5 (124). Besides, when the verapamil (P-gp inhibitor) and indomethacin (MRP2 inhibitors) concentration were increased, the P_{app} values of Andro also increased. These results suggested that P-gp and MRP2 might be participating in the mediated secretary efflux transport of Andro (26). However, there was empirical evidence that supported that MRP2 did not participate in the mediated secretary efflux transport. Based on *in situ* studies, a P-gp inhibitor (cyclosporine) and MRP2 inhibitor (probenecid) did not significantly suppress the efflux transport of Andro in the proximal intestine, which was a high expression of the MRP2 region. Whilst alone cyclosporine significantly suppressed the efflux transport of Andro in the distal intestine, which was a high expression of P-gp region. These results indicated that MRP2 did not affect the efflux transport of Andro (30). Furthermore, an *in situ* study conducted by Ye et al. (25) ongoing revealed that MRP2 and the breast cancer resistance protein (BCRP) did not affect the efflux transport of these diterpenoid lactones.

Andro has shown high first-pass metabolism. Furthermore, the rapid metabolism of Andro in the duodenum did not involve CYP450 and bacterium in the duodenum. Yang et al. boiled blank duodenal Kreps-Ringer perfusate for 30 min to inactivate the activity of CYP450 and bacteria. These results showed that Andro was still metabolized (26). Based on *in situ* study, approximately 70.0 - 86.4% of Andro was rapidly metabolized into 14-deoxy-12-sulfo-Andro in a duodenum segment within 60-120 min. An approximately 15% and 10% of 14-deoxy-12-sulfo-Andro were observed in the jejunum and ileum respectively (25, 26). The rapid metabolism of Andro did not occur from the biological instability of lactones because the sulfate metabolite was still found in the blank duodenum and jejunum perfusate. Ye et al. hypothesized that blank perfusate may have contained enzymes sloughed off from epidermal cells (25). A bio-distribution study revealed that 14-deoxy-12-sulfo-Andro was mainly present in blood, liver, and kidneys (25).

Currently, no studies have been published to imply whether the kinetics behavior of Andro is non-linear or linear pharmacokinetics. However, Panossian et al. found that Andro almost totally (F_{oral}~90%) absorbed into the blood circulation after oral administration of 20 mg/kg *A. paniculata* extract. When increasing the dose by 10 times (200 mg/kg), the F_{oral} value decreased from 90% to 20%, and the AUC value increased just 2-fold. Whilst other pharmacokinetic parameters were almost the same. Those results suggested that Andro might not saturate in the absorption process (36).

2. Distribution

Andro has high human plasma protein binding. Based on equilibrium dialysis assay, approximately 55% of Andro bound with human blood plasma protein (HBPP) at 4 h. The researcher ongoing revealed that Andro is mainly bound with albumin in human blood. In addition, approximately 20% and 60% of Andro bound to bovine serum albumin (BSA) at 4 h and 24 h respectively after incubation. There had no substantial difference in protein binding was found after 24 h (36). Additionally, there was a relatively low accumulation of Andro in red blood cells because the blood plasma ratio (R_{bp}) was found to be 0.93 (35).

Andro has a high volume of distribution and is widely distributed in many tissues after intravenous and oral administration. Following the published pharmacokinetic studies, The V_d values for Andro in animals were relatively high when the V_d value was greater than the total body water in rodents (~74.0% – 74.7% in mice and rats) (125). As the V_d value of Andro **is** equal to 28.17 mL/g in mice (12) and 24.13 – 62.66 mL/g in rats (26, 126)**.** Based on animal studies, the amount of Andro was mainly distributed in the kidney (AUC_{0-inf} = 189.47 nmol min/mL), liver (AUC_{0-inf} = 90.31 nmol min/mL), lungs (AUC_{0-inf} = 0.43 nmol min/mL), spleen (AUC_{0-inf} = 0.43 nmol min/mL), and heart (AUC_{0-inf} = 0.37 nmol min/mL) in mice following intravenous injection of 500 mg/kg (34). Furthermore, Andro was found in kidneys, liver, lung, spleen, heart, as well as brain in rats following repeated dosing orally for 28 days (35).

3. Elimination

The urinary and biliary excretion might not be the major way to eliminate Andro. In accordance with Panossain et al., only 8.75% of unchanged Andro was eliminated by urinary excretion in rats after an oral administered dose of *A. paniculata* extract. Thus, more than 90% of Andro might be eliminated *via* other ways (36). Besides, Ye et al. ongoing reported that approximately 5% of Andro was excreted in bile (25). The bile flow was little increased in rats following oral administration (127). Following UPLC/MS/MS and FTICR-MS analysis results, the possible metabolic pathway of Andro in rats, dogs, and human liver microsomes (RLMs, DLMs, and HLMs) was revealed as shown in Figure 5 (128). Besides, there were eight and eleven metabolites found in RLM and HLM, respectively. The summary of *in vitro* metabolism of Andro was shown in Table 7. Based on animal studies, nine metabolites were found in rat faces and urine after oral administration of Andro (129-131). Also, 15 metabolites were found in rat and human faces and urine after consuming Andro orally (132-135). The summary of metabolites found in rats and humans was gathered in Table 8.

Andro has been rapidly metabolized using RLMs. Approximately 95% of Andro was rapidly metabolized *via* dehydration, hydrogenation, and deoxidation reaction with the intrinsic clearance (CL_{int}) value of 94.4 µL/min/mg proteins. This value was 15-fold higher than the *in vitro* intrinsic clearance acquired from HLMs (128). The sulfonates were the major metabolite, namely 14-deoxy-12(*R*)-sulfo-Andro, in rats following oral administration (129-131). This metabolite was produced in the small intestine in rats because it did not detect in the bile product (131).

The major metabolite in humans was glucuronide and some sulfate. The metabolite namely 19-*O*-*β*-*D*-glucuronide-Andro was accounted for over 80% of total metabolites in human urine (37, 132-135). In accordance with Tian et al., this metabolite was produced by UDP-glucuronosyltransferase 2B7 (UGT2B7) and was produced in liver microsomes from pigs, dogs, monkeys, mice, and humans except for rats (37). Based on a kinetic characterization test, the UGT2B7 had the highest affinity for Andro. The *in vitro* Michaelis-Menten constant (K_m) values for UGT2B7 and UGT1A2 were 1.46 µM, and 1,020 µM, respectively. Whilst the K_m value for UGT2B4 was not detected. These results suggested the UGT2B7 might be a major

metabolizing enzyme for Andro (37). Despite the saturation of metabolism of Andro did not publish, the saturation of metabolism of this diterpenoid is likely to occur after oral administration of *A. paniculata* tablets at the high dose in healthy volunteers (38).

Figure 5 The possible metabolism pathway of andrographolide in rat, dog, and human liver microsomes

Source: Adapted from Zhao et al. (128)

Table 7 Summary of metabolites of Andro using rat and human liver microsome

Metabolite No.	Possible Metabolite name
Phase I	
M1-1	6,7-dehydro-andrographolide [a]
M1-2	14-deoxy- andrographolide [a]
M1-3	3-dehydro-andrographolide or 19-dehydro-andrographolide [b]
M1-4	14-dehydro-andrographolide [a, b]
M1-5	12-hydrogenated-andrographolide [a, b]
M1-6	9- hydrogenated-andrographolide [a, b]
M1-7	14-dehydro-12-hydrogenated-andrographolide [a, b]
M1-8	12,13-dehydro,14-deoxy-andrographolide [b]
Phase II	
M2-1	3-glucuronide-andrographolide [b]
M2-2	glucuronide-M1-8 [b]
M2-3	glucuronide-M1-8 [b]
M2-4	14-glucuronide-andrographolide [a, b]
M2-5	19-glucuronide-andrographolide [a, b]

[a] Metabolites od Andro could be identified in rat liver microsome

[b] Metabolites od Andro could be identified in human liver microsome

Source: Adapted from Zhao et al. (128)

Table 8 Summary of metabolites detected in rats and human faces as well as urine after oral administration of Andro

Metabolite No.	Possible Metabolite name	Reference
Phase I		
M1-9	Isoandrographolide [a]	(130)
M1-10	14-deoxy-andrographolide [a]	
Phase II		
M2-6	Andrographolide-3-O-sulfate [b]	(132)
M2-7	Isoandrographolide-3-O-sulfonate [b]	
M2-8	14-deoxyandrographolide-3-O-sulfate [b]	
M2-9	14-deoxy-12-(cysteine-S-yl)-andrographolide-3-O-sulfate [b]	
M2-5	Andrographolide-19-O-β-D-glucuronide [b]	(133)
M2-10	Isoandrographolide-19-O-β-D-glucuronide [b]	
M2-11	Andrographolide-19-O- [6′-methyl-β-D-glucuronide] [b]	(134)
Phase I and phase II		
M3-1	14-deoxy-12(*R*)-sulfo-andrographolide [a]	(129, 131)
M3-2	14-deoxy-12(*S*)-sulfo-andrographolide [a]	
M3-3	14-deoxy-12(*R*)-sulfo-9(*S*)-andrographolide [a]	
M3-4	14-sulfo-isoandrographolide [a]	
M3-5	14-deoxy-12(*R*)-sulfo-andrographolide 3-sulfate [a]	
M3-6	14-deoxy-12(*S*)-sulfo-andrographolide 3-sulfate [a]	(130)
M3-7	14-deoxy-11,12-didehydroandrographolide [a]	
M3-8	14-deoxy-12-hydroxy-andrographolide-19-O-β-D-glucuronide [b]	
M3-9	14-deoxy-12(13)-en-andrographolide-19-O-β-D-glucuronide [b]	(133)
M3-10	14-deoxyandrographolide-19-O-β-D-glucuronide [b]	
M3-11	3-oxoandrographolide-19-O-β-D-glucuronide [b]	
M3-12	14-deoxy-12-carbamido-andrographolide [b]	
M3-13	14-deoxy-12-carbamido-andrographolide-19-O-sulfate [b]	(134)
M3-14	14-deoxy-12(R/S)-carbamido-andrographolide-19-O-β-D-glucuronide [b]	
M3-15	14-deoxy-12(S/R)-carbamido-andrographolide-19-O-β-D-glucuronide [b]	

[a] Metabolites od Andro could be identified in rat liver microsome

[b] Metabolites od Andro could be identified in human liver microsome

Interaction and drug-metabolizing enzyme

Several *in vitro* studies revealed that Andro induced and inhibited many CYP450 isoforms and UGT2B7 as shown in Table 9. In addition, *in vivo* studies have resulted in the drug interaction between Andro and CYP1A2, 3A2, 2C9 substrates being published and shown in Table 10. Thus, co-administration of Andro and such medicine might be the cause of herb-drug interaction, therapeutic failure or increase toxicity of conventional drug therapy.

Furthermore, Andro has been a weak P-gp inhibitor. According to Li et al., Andro could inhibit digoxin transportation by 25.35% from BL to AP in multidrug resistance protein 1-Madin-Darby canine kidney cells. Similarly, MDR1-MDCKII cells demonstrated an inhibition effect by verapamil of 90.75%. These results were in line with a caco-2 cell model where the inhibitory effect of Andro on digoxin transport was 35.80% while verapamil was 77.75% (136).
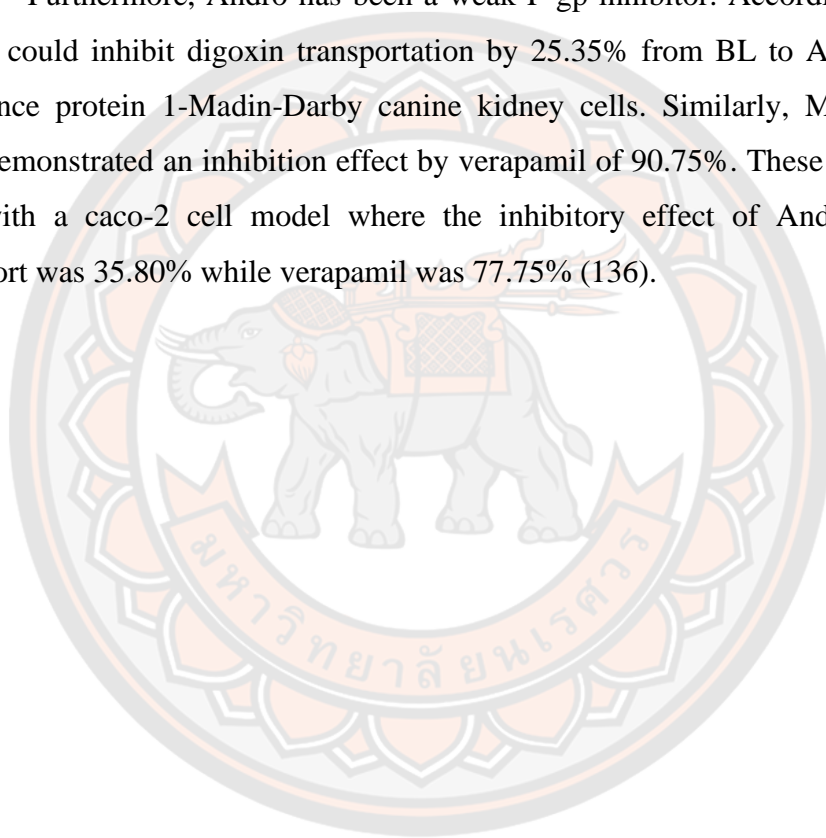
Table 9 The effect of andrographolide on CYP450 mediated metabolism and the other drug metabolizing enzymes in *in vitro* studies

Author	Year	Studies	CYP450 / Other enzymes	Concentration	Results
Effect of andrographolide on phase I metabolism					
Jaruchotikamol et al.(137)	2007	Mice hepatocyte	CYP1A1	12.5 – 50.0 µM	Induction
			CYP1A2		
Pekthong et al. (138)	2009	Rats and human hepatocyte	CYP3A4	50.0 – 60.0 µM	Inhibition
Ooi et al. (139)	2011	HepG2 cell	CYP3A4	50.0 – 60.0 µM	Inhibition
Pekthong et al.(138)	2009	Rats and human hepatocyte	CYP2C9	50.0 µM	Inhibition
Effect of andrographolide on the other drug-metabolizing enzymes					
Abdullah et al. (140)	2014	HLMs	UGT1A1	>100 µM	Inhibition
			UGT1A4	>100 µM	Inhibition
			UGT2B7	0.01 – 100 µM	Non-competitive inhibition (IC_{50} = 1.7 ± 0.3 µM; Ki = 2.8 µM)
Ma et al. (141)	2014	HLMs	UGT2B7	100 µM	Inhibition (Ki = 6.1 µM)
Uchaipichat et al. (142)	2018	PHLMs	UGT2B7	1 – 500 µM	Inhibition (IC_{50} = 4.4 – 21.6 µM; Ki = 2.4 – 3.1 µM)
Abdullah et al. (143)	2018	RLMs and HLMs	UGT2B7	1 – 100 µM	Inhibition (IC_{50} = 6.2 ± 1.27 µM)
Chang et al. (144)	2008	Rats hepatocyte	GST	10 – 20 µM	Induction

RLMs is rat liver microsomes; HLMs is human liver microsomes; PHLMs is pooled human liver microsomes; HepG2 cell is human liver cancer cell line; GST is Glutathione S-transferase.

Table 10 Summary of the effect of Andro on cytochrome P450 mediated metabolism in *in vivo* studies

Author	Year	Animal model	Victims	CYP isoform	Results
Chie et al. (145)	2010	Rats	Theophylline	CYP1A2	CL +136%, AUC −133%, $t_{1/2}$ +108%, MRT +120%
Balap et al. (146)	2017	Rats	Nabumetone	CYP1A2	CL +150%, AUC −145%, $t_{1/2}$ +145%, MRT +105%
Balap et al. (62)	2016	Rats	Etoricoxib	CYP1A2	CL +200%, AUC −219%, $t_{1/2}$ +226%, MRT +166%
Samala et al. (147)	2016	Rats	Glyburide	CYP2C9	CL −149%, AUC +149%, $t_{1/2}$ +109%, MRT +109%
Zhang et al. (148)	2018	Rats	Warfarin	CYP2C9	AUC +195%, $t_{1/2}$ +159%, MRT +113%
Wongnawa et al. (149)[a]	2012	Human	Midazolam	CYP3A4	CL/F = −102%, AUC = +107%, $t_{1/2}$ +102%

[a] used *A. paniculata* extract in a study

Determination of the dosage regiment

In order to determine the dosage regimen, there were many approaches: 1) a dose-by-factor (based on no observed adverse effect levels; NOAELs); 2) a pharmacokinetically-guided approach; 3) a minimal anticipated biological effect levels (MABEL) approach; 4) a pharmacokinetic/pharmacodynamics (PK/PD) model; 5) similar drug approach, and 6) microdosing (39). The details of each of these approaches are shown below.

1. **Dose-by-factor**

The dose-by-factor method is frequently used to determine dosage. This method focuses on the NOAEL of the drug from the dose-response curve of a well-designed animal toxicological study. The NOAEL (assessed in animals) adjusted with allometric factors is used to estimate the maximum recommended starting dose (MRSD) for clinical investigation in healthy human subjects. The MRSD is determined by assuming that there is a 1:1 relation between species when the body surface area is normalized. Information such as preclinical data, pharmacologically active doses (PADs), toxicological profiles, and pharmacokinetics is considered when using this method. In order to determine the MRSD, the following five steps must be considered: (1) determine NOAEL, which is the highest dose level that does not cause a significant adverse effect. The NOAEL values should be identified using three or more animal species and one of which should be nonrodent, (2) conversion of the NOAEL to human equivalent dose (HED) that based on the body surface area using scaling factors, (3) selection of species based on the similar of the ADME processes between animal and human, (4) applying a safety factor to conduct the safe dose in first clinical dose, and (5) consideration of PAD, which is the minimum dose tested in an animal species with the expected pharmacological activity, by comparing to the MRSD, which obtained from step four. The PAD value can be used to estimate the HED also. The estimated HED can be used to compare to the MRSD. If the HED is lesser than the MRSD, it is recommended to reduce the clinic dose for scientific reasons. The started dose is recommended lower than the MRSD (39).

The advantage of this approach is that it is easy to use. However, it is not appropriate when; 1) drug administration is *via* intramuscular, subcutaneous, and intranasal routes; 2) vaccines and drugs are applied to endogenous hormones used at physiological concentrations; 3) drugs are limited in non-linear pharmacokinetics (39).

2. Pharmacokinetically-guided approach

This approach is based on pharmacokinetic properties. The starting dose is calculated following equation: the starting dose in mg = AUC_{animal} (mg.h/mL) x CL_{human} (L/h) where AUC_{animal} is the area under the curve in animals obtained from a NOAEL study, and CL_{human} is the scaled-up human clearance using animal data. In most instances, a safety factor value is applied to further calculate the starting dose following equation: the starting dose (mg)/the safety factor value which is ranged from 1 to 10.

This approach is generated based on two assumptions: 1) only the parent compound is active; 2) the drug shows identical pharmacological activity or toxicity in human and animal species at equal plasma concentrations. Thus, it is become to be the first limitation. In addition, the neglection of interspecies differences becomes to be the second limitation of this approach (39).

3. Minimal anticipated biological effect levels

This approach is based on pharmacological facts and is expected to produce a biological effect in a clinical trial. This is an improved approach to dose selection through a pharmacological threshold that begins with the lowest active dose and ends with the highest safe dose. A factor of safety is applied to reduce toxicity in humans. The factor influencing risk has been the information related to the mode of action, the type of the target, and/or the applicability of animal models. The minimal anticipated biological approach could be used when the factors influencing risk are identified. However, this approach has been useful for both bio-therapeutics and small drug molecules but requires extensive mechanistic data (39).

4. Pharmacokinetic-pharmacodynamics modeling using animal data

This is a mathematical approach that simulates a human dose exposure relationship using data from animal species. A human PK-PD profile is predicted using the data from animal species. In brief, a human dose is estimated *via* four steps:

1) establishing the concentration-effect relationships to determine PD parameters (e.g. EC_{50}, IC_{50}) then develop PD model in animals; 2) identifying the interspecies variations in the concentration-response profiles, for both anticipated and adverse effects; 3) establishing the PK model and predicting human pharmacokinetic parameters and plasma concentration-time profiles; 4) integrating human PK and PD models to estimate human dose-response relationships. The dosage regimen is designed to maintain plasma drug concentrations over the threshold of efficacy but below the threshold of adverse effects. The major limitation of this approach is that it requires a lot of effort to establish PK–PD models and also needs data from different sources for model validation (39).

5. Similar drug approach

This approach can be used when the human PK-PD data is available for another drug under a similar pharmacological category such as the mechanism of action, physiologic effect, and chemical structure. The starting dose will be estimated if the information related to the NOAELs of a new drug, a similar drug, and the dose of a similar drug is available. Generally, a safety factor is also applied to calculate the estimated dose to avoid toxicity (39). The equation for determination of the starting dose of a new drug is described following (the starting dose of a similar drug/NOAEL to a similar drug) / (starting dose of new drug/NOAEL to new drug). Followed this, the safety factor is applied to calculate a starting dose of a similar drug (39). For instance, the NOAEL value of a new drug in mice is 3 mg/kg/day while the similar drug the NOAEL value is 10 mg/kg/day, and the starting dose of a similar drug is 5 mg/kg/day. Therefore, the starting dose of a new drug is 1.5 mg/kg/day (=5/10 x 3). If a human weighing is 60 kg, the calculated dose will be 90 mg. Then, a safety factor of 10 is applied, thus, the starting dose in humans will be 9 mg (=9/10). The main limitation of this approach is that (1) using a cross-species dosing ratio for one drug to another drug, and (2) assumption that the difference of PK and PD between animals and humans are the same for both drugs (39).

6. Microdosing

This approach determines a starting dose using $1/100^{th}$ of the dose determined for a pharmacological effect on mg/m^2 basis, however, the specific dose cannot be $1/1,000^{th}$ of the minimum toxic effect dose as assessed from toxicology studies using a single dose. This approach is appropriate for drugs with the main pharmacological effect that cannot be shown in animal species (39).

According to limitations on the pharmacokinetic properties of Andro and the lack of the necessary data from *in vivo* studies (e.g., NOEAL, PAD), determination of the FIH dose of Andro could not be performed *via* such approaches, and *in vivo* studies require a lot of the budget and time. To save cost and time in this process, the physiologically based pharmacokinetic model provided a more appropriate approach.

Physiologically based pharmacokinetic (PBPK) model

PBPK is a mathematical approach that can predict the concentration-time profile in plasma and many organs. This model is constructed using a series of differential equations based-on pharmacokinetics, physiological parameters, necessary physicochemical properties, and drug biological properties. Therefore, this model allows us to better predict concentration-time profiles in plasma and many organs across different species when compared to classical pharmacokinetic models (43).

The PBPK model can precisely predict the pharmacokinetic parameters and provides a mechanistic framework to understand the kinetics behavior of the target drug in animals and humans. Also, this model estimates the dosage across species, population, and disease states. These advantages allow the PBPK model to be widely used in the early stage of drug development and the clinical stage. At a 2014 meeting on the PBPK model hosted by the US Food and Drug Administration, the PBPK model for FIH dose predictions was reported as being mainly useful for drug developers to estimate the appropriate starting dose for humans. Notably, there are many publications from industry groups confirming the predicted FIH dosages using the PBPK model. Also, this model is used in environmental toxicology and risk assessment (40, 41).

However, the limitation of this model is that it requires massive amounts of information related to physiological, biochemical, physicochemical, and pharmacokinetics. To obtain those data, the modelers must gather the data from different sources. Furthermore, some of those data might be not available and some laboratory experiments must be performed to improve the model (150).

Initially, the model should be structured minimally but retain the essential elements within the system and was still reflect real physiology. Besides, the model should be consistent with the current state of knowledge. In order to construct a minimalistic model, tissues exhibiting closer blood flow rates are lumped together such as either rapidly or slowly perfused tissue (151). However, the model complexity and capability should be consistent with the intended purpose or assumption and underlying data (152, 153). Therefore, this model should consist of many compartments representing each tissue which are linked by blood flow. In addition, the blood flow and volume of each tissue depended on the body weight (154). Typically, each tissue was described by the degree of either limitation in perfusion rate or permeability rate (43) as shown in Figure 6
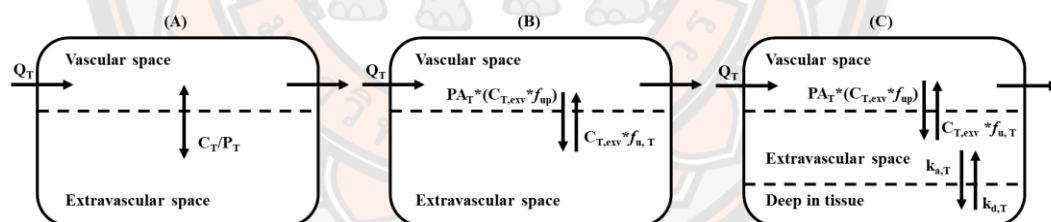
Figure 6 Model structures that describe the perfused-limited model (a), permeability-limited model (b), and permeability-limited with binding deep in tissue (c)

As the perfusion rate-limited kinetics, this kind of kinetics is used for small lipophilic molecules where the blood flow to the tissue is the limiting process. This type of model is termed "perfusion-limited model" or "blood flow-limited model". It assumes a steady state and that the total drug concentration in the tissue is in equilibrium with the total drug concentration in the systemic circulation. The tissue drug concentration (C_T) is described by the partition coefficient of tissue to plasma

(P_T); ($C_T = C_T/P_T$) where C_T is the drug concentration in the tissues. Thus, two compartments are used to write the mass balance equation (43, 155). Equation 1 describes the perfusion-limited model, which provide the change in the amount of drug over time after drug administration, where Q_T was blood flow of tissues; C_{Pl} is the concentration of the drug in plasma; C_T is the concentration of the drug in tissues; P_T is the tissue to plasma partition coefficient; and A_T is the amount of the drug in the tissue.

$$\frac{dA_T}{dt} = Q_T \times \left(C_{pl} - \frac{C_T}{P_T}\right) \qquad \textbf{equation 1}$$

As the permeability rate-limiting kinetic, this kind of kinetics is used for large polar molecules where the permeability across the cell membrane is the limiting process. This type of model is termed a "permeability-limited model" or "diffusion-limited model". In this model, the tissue is separated into two sub-compartments, including the vascular space of the tissue within the capillary membrane and the extravascular tissue space outside the capillary membrane. It is described by the permeability surface area coefficient of a tissue (PA_T). The only free drug could cross in and out of the tissue. The free drug in the vascular space is calculated by $C_{T, vas}$ multiplied by f_{up} where $C_{T, vas}$ is the drug concentration in vascular space and f_{up} was the fraction of drug that is unbound in plasma. The free drug in extravascular space is calculated by $C_{T, exv}$ divided by P_T where $C_{T, exv}$ is extravascular space (43, 155). The mass balance inside tissue vascular space and extravascular space are described in equations 2 and 3.

$$\frac{dA_{T,vas}}{dt} = Q_T \times \left(C_{pl} - C_{T,vas}\right) - PA_T \times \left(\left(C_{T,vas} * f_{up}\right) - \left(C_{T,exv} \times f_{uT}\right)\right) \textbf{equation 2}$$

$$\frac{dA_{T,exv}}{dt} = PA_T \times \left(\left(f_{up} \times C_{T,vas}\right) - \left(C_{T,exv} \times f_{uT}\right)\right) \qquad \textbf{equation 3}$$

The following abbreviations are used in differential equations 2 and 3: $A_{T,\,vas}$ is the amount of drug in the vascular space of the tissue; $A_{T,\,exv}$ is the amount of drug in the extravascular space of the tissue; PA_T is the permeability surface area coefficient of the tissues; f_{uT} is the fraction unbound in tissues.

Last, the permeability-limited with deep binding in the tissues model also is described by PA_T value but the drug accumulation is described by the association $(k_{a,T})$ and dissociation $(k_{d,T})$ rate constants (155). This model is separated into three sub-compartments including the tissue vascular space, the tissue extravascular space, and the deep tissue compartment. The mass balance of the deep tissue compartment is described by equations 4 to 6.

$$\frac{dA_{T.vas}}{dt} = Q_T \times \left(C_{pl} - C_{T,vas}\right) - PA_T \times \left(\left(C_{T.vas} \times f_{up}\right) - \left(C_{T,exv} \times f_{uT}\right)\right) \qquad \textbf{equation 4}$$

$$\frac{dA_{T.exv}}{dt} = PA_T \times \left(\left(C_{T,vas} \times f_{up}\right) - \left(C_{T,exv} \times f_{uT}\right)\right) - \left(k_{a,T} \times \left(C_{T,exv} \times f_{uT}\right) \times V_{T,exv}\right) + \left(k_{d,T} \times A_{T,D}\right) \qquad \textbf{equation 5}$$

$$\frac{dA_{T,D}}{dt} = \left(k_{a,T} \times \left(C_{T,exv} \times f_{uT}\right) \times V_{T,exv}\right) - \left(k_{d,T} \times A_{T,D}\right) \qquad \textbf{equation 6}$$

The following abbreviations are used in differential equations 4 to 6: $A_{T,\,D}$ is the amount of Andro in the deep in tissue; $V_{T,\,exv}$ was the volume of tissue extravascular space; $k_{a,\,T}$ is the association rate constant; $k_{d,\,T}$ is the dissociation rate constant.

1. Model Parameterization

The PBPK model consisted of many specific tissue compartments and require numerous input parameters to solve a series of differential equations. Their input parameters are divided into three main parameter groups; 1) physiological specific properties such as blood flow rate and tissue volume; 2) physicochemical specific properties such as drug fraction binding plasma protein and tissue to plasma partitioning; 3) biochemical properties such as membrane transporter, enzymatic activity, and rate of absorption.

1.1 Physiological parameters

Physiological parameters including the tissue mass balance, the volume fraction of blood in tissue, blood flow to tissue (Q_T), and cardiac output (Q_{CO}) are obtained from Brown et al. (156).

Tissue mass balance or the fraction volume of tissues (V_{TC}) and the volume fraction of blood in tissue ($V_{TC, vas}$) are used to converse into volume of tissue (V_T) and vascular space volume of tissue ($V_{T, vas}$) based on mass-to-volume conversion with assumption of unity density (volume = mass/density of tissue that was assumed equal to 1). These values represent as fraction or percentage of average body weight as presented in Table 11-12. The V_T or $V_{T, vas}$ values are calculated using following equation; V_T or $V_{T, vas}$ = V_{TC} or $V_{TC, vas}$ * BW (body weight in kilograms).

Blood cardiac output (Q_{CO}) values in mice, rats, dogs, and humans are calculated based on allometric relationship, as follows: $Q_{CO, mice}$ (L/h) = 16.5*(BW)$^{0.75}$ (body weight in kilogram); $Q_{CO, rats}$ (L/h) = 14.1*(BW)$^{0.75}$ (body weight in kilogram); $Q_{CO, dogs}$ (L/h) = 0.063*(BW)$^{0.75}$ (body weight in gram); $Q_{CO, humans}$ (L/h) = 15*(BW)$^{0.74}$ (body weight in kilogram). The tissue blood flow rates (Q_T) presented as percentage of the Q_{CO} value as shown in Table 13. The perfusion of tissue can be used to determine the rapidly and slowly tissues using following equation; perfusion of tissue = Q_T/V_T (156).

Table 11 A summary of the mean of tissue mass balance of each species for conversion into a percentage of tissue volume values for use in the PBPK model

Tissue	Mice	Rats	Dogs	Humans
Adipose	~7.0	~7.0	~15.0	21.4
Bone	10.7	7.3	8.1	14.3
Brain	1.7	0.6	0.8	2.0
Gastrointestinal Tract	4.2	2.7	3.7	1.7
Heart	0.5	0.3	0.8	0.5
Kidney	1.7	0.7	0.5	0.4
Liver	5.5	3.4	3.3	2.6
Lungs	0.7	0.5	0.8	0.8
Muscle	38.4	40.4	45.7	40.0
Skin	16.5	19.0	9.1	3.7
Gastrointestinal Tract Contents	5.7	~5.0	4.3	1.4
Blood	4.9	7.4	8.2	7.9
Rest of body	2.5	5.7	0	3.3

Source: Adapted from Brown et al. (156)

Table 12 Summary of the mean of volume fraction of tissues of animals and humans such as adrenal, adipose, bone, and brain

	Mice		Rat		Dogs		Human	
	Mean	Range	Mean	Range	Mean	Range	Mean	Range
Adrenal	0.03	-	0.24	-	-	-	-	-
Adipose	-	-	-	-	-	-	0.02±0.01	0.02-0.03
Bone	0.11	-	0.04	-	-	-	0.04	-
Brain	0.03	-	0.03	0.02-0.04	0.01	-	0.04±0.01	0.03-0.10
Heart	-	-	0.26	-	0.07	-	1	-
Kidney	0.24	0.12-0.34	0.16	0.11-0.27	0.08	-	0.36±0.01	0.22-0.50
Liver	0.31	0.23-0.36	0.21	0.12-0.27	0.15	-	0.11	-
Lung	0.50	0.40-0.62	0.36	0.26-0.52	0.30	-	-	-
Muscle	0.04	0.03-0.05	0.04	0.01-0.09	0.01	-	0.01	-
Skin	0.03	-	0.02	-	-	-	0.08	-
Spleen	0.17	0.17-0.19	0.22	0.17-0.28	0.51	-	-	-
Thyroid	-	-	0.18	-	-	-	-	-

Source: Adapted from Brown et al. (156)

Table 13 Summary of regional blood flow distribution mean percentage cardiac output of animals and humans

Tissue	Mice	Rats	Dogs	Humans
Adipose	9[a]	7.0	-	5.2
Adrenals	-	0.3	0.2	-
Bone	-	12.2	-	4.2
Brain	3.3	2.0	2.0	11.4
Heart	6.6	5.1	4.6	4.0
Kidney	9.1	14.1	17.3	17.5
Liver (Total)	16.1	18.3	29.7	22.7
Hepatics Artery	2.0	2.1	4.6	-
Portal Vein	14.1	15.3	25.1	18.1
Lung	0.5	2.1	8.8	-
Muscle	15.9	27.8	21.7	19.1
Skin	5.8	5.8	6.0	5.8
Thyroid	-	-	-	1.6

[a]Data from Lyons et al. (157)

Source: Adapted from Brown et al. (156)

1.2 Physiochemical parameters

Tissues to plasma partition coefficents or P_T are necessary parameters to develop the PBPK model. The P_T value is the ratio of tissue drug concentration to the concentration of the drug in plasma. This value is obtained from *in vitro* and *in vivo* approaches. For example, the *in vivo* P_T of each tissue was calculated using the following equation (158):

$$P_T = \frac{AUC_{tissue,0-t}}{AUC_{plasma,0-t}} \qquad \textbf{equation 7}$$

where $AUC_{tissue,\ 0-times}$ is the area under the concentration-time curve in tissue from zero to a given time, and $AUC_{plasma,\ 0-times}$ is the area under the concentration-time curve in plasma from zero to a given time.

Where *in vivo* data is not available, the P_T value was calculated from *in vitro* data. For instance, when the drug is distributed homogeneously mainly by passive diffusion into the tissues, equations 8 and 9 were used to predict the tissue to plasma coefficient (159, 160).

$$P_{T,nonadipose} = \frac{Pow\ (f_{nlT}+0.3f_{plT})\ +(f_{wT}+0.7f_{plT})}{Pow\ (f_{nlP}+0.3f_{plP})+(f_{wP}+0.7f_{plP})} \times \frac{f_{up}}{f_{uT}} \qquad \textbf{equation 8}$$

$$P_{T,adipose} = \frac{Dow\ (f_{nlT}+0.3f_{plT})\ +(f_{wT}+0.7f_{plT})}{Dow\ (f_{nlP}+0.3f_{plP})+(f_{wP}+0.7f_{plP})} \times \frac{f_{up}}{1} \qquad \textbf{equation 9}$$

$$f_{uT} = \frac{1}{(1+\left(\frac{1-f_{up}}{f_{up}}\right)*0.5} \qquad \textbf{equation 10}$$

The fractional volume contents of neutral lipid, phospholipids, and water in plasma or in tissue are represented by f_{nl}, f_{pl}, and f_w respectively. Neutral phospholipids are assumed to be a mixture of 30 % neutral lipids and 70% water (161). The fraction unbound in tissues (f_{uT}) is calculated *via* equation 10 (160). The fractional composition of certain tissues in animals and humans presents in Table 14.

However, sometimes the calculated P_T value showed low accuracy, possibly because of unexpected distribution and clearance processes under *in vivo* conditions. This limitation can be overcome for estimation using PBPK models by assuming a homogeneous distribution of the drug into each tissue by a process of passive diffusion and/or the metabolic clearance mainly present in the liver (160).

1.3 Biochemical parameters

Biochemical parameters such as the absorption rate constants, metabolic parameter (i.e., first-order or second-order, Michaelis-Menten kinetic), and transporter activity were obtained from published experimental studies or estimations. These parameter values can be either scaled up from *in vitro* studies to *in vivo* values or estimate from *in vivo* studies (162, 163). The metabolism rate can be described by either Michaelis-Menten kinetic or hepatic intrinsic clearance (CL_{int}). The maximum velocity of metabolism (V_{max}) and CL_{int} values are varied depending on the experiment system. These *in vitro* values require scaling up before running the model.

The *in vitro-in vivo* extrapolation method is used to scale it up from *in vitro* data to whole tissue with scaling factors (i.e., microsomes, hepatocytes, or liver weight in a gram of body weight) which is species-dependent (163). Whereas the Michaelis-Menten constant (K_m) value, which is expressed as a concentration in venous at equilibrium with the liver, is used directly with conversion to correctly units for running the model (164).

Table 14 Fractional composition of tissues in animals and humans

Tissues	Water (f_w)			Neutral Lipids (f_{nl})			Phospholipids (f_{ph})		
	Mice	Rats	Humans	Mice	Rats	Humans	Mice	Rats	Humans
Adipose	-	0.120	0.180	-	0.8530	0.7900	-	0.0020	0.00200
Bone	-	0.446	0.439	-	0.0273	0.0740	-	0.0027	0.00110
Brain	0.710	0.788	0.770	0.0310	0.0392	0.0510	0.0500	0.0533	0.05650
Gut	0.700	0.749	0.718	0.0320	0.0292	0.0487	0.0150	0.0138	0.01630
Heart	0.780	0.779	0.758	0.0170	0.0140	0.0115	0.0140	0.0118	0.01660
Kidneys	-	0.771	0.783	-	0.0123	0.0207	-	0.0284	0.01620
Liver	-	0.705	0.751	-	0.0138	0.0348	-	0.0303	0.02520
Lung	0.810	0.790	0.811	0.0218	0.0219	0.0030	0.0162	0.0140	0.00900
Muscle	0.670	0.756	0.760	0.0167	0.0100	0.0238	0.0273	0.0090	0.00720
Skin	-	0.651	0.718	-	0.0239	0.0284	-	0.0180	0.01110
Spleen	0.790	0.771	0.788	0.0120	0.0077	0.0201	0.0107	0.0136	0.01980
Plasma	0.960	0.960	0.945	0.00260	0.00147	0.0035	0.0032	0.00083	0.00225

Source: Adapted from Poulin et al. (160, 165)

2. Model Estimation and Selection

Estimation is a process that attempts to find a set of parameters to explain a given set of data (166). The estimated parameters are shown as the percentage coefficient of variation (%CV), when this value is not over 30%, indicating high precision and reasonably estimated parameters (158). Whereas simulation is a process that looks forward in time. In brief, given a model and a set of parameters, what happens if the input is varied (166).

During the PBPK model development processes, there are many generated PBPK models. To determine the "better" model, it is necessary to compare it with another alternatively developed model. The word "better" is employed because it denotes semi-quantitative words that one intuitively has a feeling (not real) as being defined. Therefore, prior assessment of the model is by visual inspection or graphical analysis (166).

Model selection should be based on biology, physiology, and plausibility. In addition, the Akaike information criteria (AIC) provides a tool that can be used for data analysis and model selection. The model with the smallest AIC value reflects the lowest degree of lost information between the true model and the approximating model. Also, there are a few other factors such as residual plots, goodness of fit plots, precision and plausibility of parameters, reasonable and valid model assumptions, and proper judgment (166).

3. Model Evaluation

The model evaluation has been performed to establish confidence in the model and the quality of the input parameters. In addition, this process could express the ability of the model whether how well the model simulations correspond to the experimental data. This can be judged through several methods such as visual inspection, discrepancy tests, and statistical methods which included linear regression analysis, residual plot, and mean absolute percentage error calculation. The qualitative method termed "visual inspective" refers to examine how well the model simulation replicates the observed pharmacokinetic profile (167, 168). According to World Health Organization (WHO) guidelines, the n-fold metric system has been used as the model evaluation criteria also. This method could judge the reasonable of the model. Typically, the model is considered reasonable and validated when the proportion of

the predicted pharmacokinetic parameters such as AUC and C_{max} is within 2-fold of observed values (167). However, 3-fold predicted error could be acceptable for drugs with high variability (169).

The model evaluation could perform in many ways. First, the model is evaluated by comparing the result of model simulation to an independent dataset which is a different dataset in a different study from other laboratories with similar study design (i.e., same or similar animal species, dose level, exposure route, measurement methodology, etc.) (167, 168). Usually, the PBPK model evaluation with an independent dataset is required to develop a validated and reliable. Second, the model should evaluate by comparing the model simulated to the different datasets which used different study designs such as in different animal species (interspecies extrapolation), at different dosage (dose extrapolation), *via* different exposure routes (route-to-route extrapolation), and for different exposure duration (duration extrapolation) (168).

Sensitivity analysis is a tool for quantitative evaluation of how input parameters influence the model output. Also, it is used to describe the relative importance of each input parameter that impact of change in individual parameters on the model output. A sensitivity ratio of 1 is defined that a 1% change in the input parameter value led to a change by 1% in model output (i.e., AUC, C_{max}, and C_{plasma}). This indicates the output is sensitive to that input parameter under the conditions evaluated (167).

4. Monte Carlo Simulation

Monte Carlo (MC) analysis is a developed analysis method that uses to obtain a probabilistic approximation to the solution of a mathematical equation or model using statistical sampling techniques. However, in this context, MC simulation is the process of approximating the model output through repetitive random application of a mathematical model (170).

Uncertainty refers to lack of knowledge about specific parameters (i.e., measurement errors, sampling errors, systematic errors), models (i.e., uncertainty due to necessary simplification of real-world processes, misspecification of the model structure, use of inappropriate surrogate variables), or scenario (i.e., descriptive errors, aggregation errors, errors in professional judgment, incomplete analysis) (170). The

MC method also is a form of uncertainty analysis (168, 171). The variance in the model output is estimated through the random sampling of input parameters (168).

Typically, the MC simulation randomly samples model parameters from defined either normal or log-normal distribution. The fraction tissue blood flow and volumes are assumed to have normal distribution while the partition coefficients and kinetic parameters are assumed to have a log-normal distribution. The body weight, cardiac output, and ventilation rate have been represented by both normal and log-normal distribution. A uniform distribution may be used if they are more appropriate for a parameter in which any value would be as equally likely as another (168).

Determination of the means, standard deviation (SD), and bounds for distributions are important for MC simulation. These values may be found from various available published sources (168). The means for distribution should be either based upon the population to be simulated or the population represented by the current model parameters. When we talk about the mean values, we should think of the SD values. The variation in the parameter often presents as a coefficient of variation (CV) (168, 172). If the SD and CV values cannot be found, a value for a similar tissue may be used or a CV representing moderate variation (i.e., CV of 20-30%) may be used (172). These values could be calculated using the equation follows: SD = Mean/CV. In order to avoid biologically implausible or extreme outlier values, certain distributions should be undertaken. Generally, the distribution may be truncated at 2-fold, 2.5-fold, or 3-fold of SD values to represent 95%, 97%, or 99% of the population, respectively (168).

CHAPTER III

RESEARCH METHODOLOGY

This section presents the methodology employed in this study. To create the PBPK model, a narrative review of Andro pharmacokinetics was undertaken. This information is provided in the literature review section. Following this, the PBPK model was developed based on available pharmacokinetic datasets identified from previously published studies.

Data Source Collection

Studies related to Andro tissue distribution were researched from three databases, PubMed, Scopus, and the Web of Science, from their inception to January 2021. The following search terms were used "andrographolide" AND "pharmacokinetics OR tissue distribution OR plasma concentration". Published studies were included for model development and evaluation if 1) studies reported plasma or tissue concentrations versus time of the Andro; 2) studies using healthy animals and humans; 3) studies providing sufficient information on sampling time, sample sites, analytical method, routes of administration, and dosage regimen. The exclusion criteria were: 1) studies not written in the English language; 2) review articles, surveys, and case reports; 3) assay was not selective to andrographolide; 4) modified release dosage form was used.

Of the 1,682 articles identified from the three databases, title and abstract screening left, 53 studies fitted the eligibility criteria. Exclusion criteria removed 26 of these leaving 27 studies for this electronic search as shown in the flow diagram in Figure 18. Among these 27 collected articles, one and one reported Andro plasma and tissue concentration-time profiles following intravenous injection in mice (34) and repeated oral administration in rats (35), respectively. In mice, one study reported the %F_{oral} value (9.27%) and plasma concentration over time following intravenous and oral administration of Andro solution (33). Twenty studies reported plasma concentration over time of Andro in rats. Of these twenty studies, five used

intravenous administration and fifteen used oral administration (9, 25, 26, 29, 35, 62, 112, 113, 115-120, 173-177). In addition, of twenty studies, only one study reported plasma concentration over time after intravenous and oral administration (25). The %F_{oral} values in rats were reported as 1.19%, 2.67%, and 3.00% (9, 25, 112). In addition, among the 27 collected studies, two studies reported plasma concentration-time profiles following oral administration in rabbits and one study in beagle dogs (174, 178, 179). Also, two studies reported plasma concentration-time profiles in humans, however, the F_{oral} value was not reported (180, 181).

The Selected Studies

   The detail of the studies used for model development, evaluation and extrapolation were summarized in Table 15. Except for the raw data reported in a table (34), the mean concentration-time profiles of each study were captured from figures by computer digitization (Digitizelt® version 2.3.3) (182). The studies without the reported animal's weight were excluded from this study because the actual dosage regimen could be not calculated. According to the literature review, there have no the metabolism parameters such as CL_{int}, V_{max}, and K_m of rabbit is reported, thus, the pharmacokinetics studies of Andro in rabbit did not include in this study. Although there are two pharmacokinetics studies of Andro that were conducted in humans and report the plasma concentration-time profiles, one study was excluded due to some of Andro levels in plasma on the terminal elimination phase were below a lower limit of quantification (LLOQ). Therefore, only 24 studies were enrolled. Two studies reported tissue distribution of Andro, and other studies reported only plasma concentration-time profiles.

   1. Tissue Distribution Data

    A tissue distribution study following intravenous injection of 500 mg/kg Andro in mice was used for the development of a PBPK model that described the disposition of Andro (34). The other study that described tissue distribution following oral administration of Andro in rats could represent all exposure scenarios and species that the model intends to predict (168). Thus, a study conducted by Bera et al. was a major study that was used for model evaluation after the extrapolation of the developed model to a rat PBPK model (35).

2. Plasma Concentration-Time Data

In mice, only one study reported plasma concentration-time profiles of the Andro (12). It was used for model evaluation after intravenous and oral administration. In rats, only four studies reported plasma concentration-time profiles after intravenous administration (25, 126, 183, 184), whereas no plasma concentration-time profile after intravenous administration was reported in dogs and humans. For oral administration, fifteen, one and one studies reported the profiles in rats, dogs, and humans, respectively (9, 12, 25, 26, 29, 51, 112, 113, 115, 116, 118, 119, 180, 185-187). The plasma concentration-time profiles in rats, dogs, and humans were used to evaluate the extrapolated PBPK models.
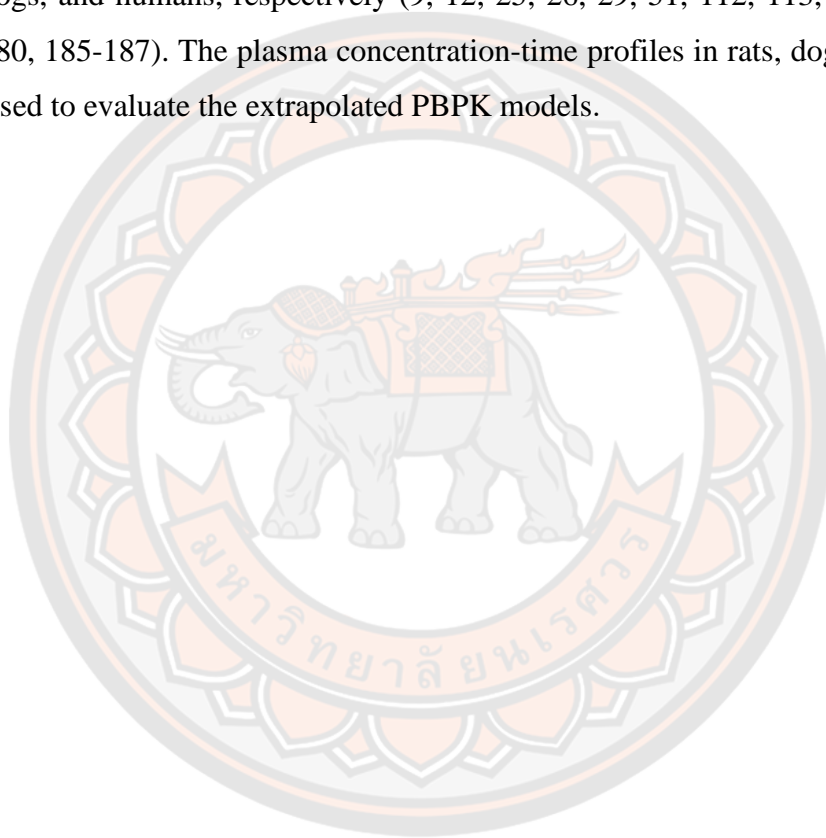
Table 15 experimental data reported on the pharmacokinetics of Andro

Animal	Weight (g)	Formulation	Dose vehicle	Dose (mg/kg)	Route of administration	Sample	Author
PBPK model development in mice (major study)							
NIH mice	18-22	Solution	ethanol	500	iv	Plasma Lung Heart Liver Kidney Spleen	Tu et al. (2014)
Model evaluation in mice (major study)							
Female BALB/c mice	19-22	Solution	10%DMSO, 10%cremophor, 80% 1/15M Na$_2$HPO$_4$	5 50	iv oral	Plasma	Banerjee et al. (2016)
Model evaluation and extrapolation to rats (major study)							
Wistar rats	150-200	Solution	0.5% (w/v) sodium-carboxymethyl cellulose solution in water containing 0.025% v/v Tween 80	30 (mg/kg) 100 (mg/kg/day)	Single oral dose Multiple oral dose	Plasma Lung Heart Liver Kidney Brain	Bera et al. (2014)
Model evaluation and extrapolation to dogs (major study)							
Beagle dog	9-11 (kg)	Pellets filled in capsules	administered with 200 mL water	15	Single oral dose	Plasma	Zhang et al. (2015)
Model evaluation and extrapolation to humans (major study)							
Chinese volunteers	NR	Tablets	NR	2.86	Single oral dose	Plasma	Xu et al. (2009)

Animal	Weight (g)	Formulation	Dose vehicle	Dose (mg/kg)	Route of administration	Sample	Author
External model evaluation to rats							
SD rats	200-240	Solution	DMSO	2	iv	Plasma	Jiang et al. (2014)
Wistar rats	180-220	Solution	Deionized water	5	iv	Plasma	Yang et al. (2013)
Wistar rats	230-270	Solution	Water and DMSO (1:1)	5	iv	Plasma	Yen et al. (2018)
SD rats	200-300	Solution	20% (w/w) beta-cyclodextrin	24	iv	Plasma	Ye et al. (2011)
Semi-external model evaluation							
Wistar rats	180-220	Suspension	NR	10	po	Plasma	Xu et al. (2016)
Wistar rats	200-240	Suspension	0.3% carboxy methyl cellulose	10	po	Plasma	Chellampillai et al. (2011)
Wistar rats	150-200	Suspension	NR	10	po	Plasma	Praveen et al. (2014)
Wistar rats	180-220	Solution	Water	20	po	Plasma	Ma et al. (2018)
Wistar rats	180-220	Solution	NR	20	po	Plasma	Chen et al. (2018)
SD rats	180-220	Suspension	Distilled water	25	po	Plasma	Ren et al. (2009)
Wistar rats	150-200	Solution	Distilled water with 0.3 g/kg CMC	25	po	Plasma	Maiti et al. (2010)
SD rats	220-240	Suspension	0.5% sodium carboxy methyl cellulose	40	po	Plasma	Qiao et al. (2017)
SD rats	220	Suspension	0.5% aqueous methyl cellulose	50	po	Plasma	Chen et al. (2014)
Wistar rats	200-250	Suspension	Physiological saline solution	50	po	Plasma	Song et al. (2019)
Wistar rats	180-220	Solution	NR	60	po	Plasma	Balap et al. (2016)
Wistar rats	230-270	Suspension	NR	100	po	Plasma	Yang et al. (2013)
SD rats	200-300	Solution	20% (w/w) beta-cyclodextrin	120	po	Plasma	Ye et al. (2011)
Wistar rats	230-270	Suspension	Water and DMSO (1:1)	300	po	Plasma	Yen et al. (2018)
SD rats	180-220	Suspension	Water	300	po	Plasma	Yen et al. (2020)

PBPK Model Development

In this study, the PBPK model construction processes consisted of two stages, including 1) the single-organ model construction which followed a PBPK model study conducted by Kagan et al. (155), and 2) whole-body PBPK model development.

The single organ model construction stage was carried out to assess drug distribution in each organ before this was applied to create the PBPK models. The Andro plasma concentration-time profile was described by a bi-exponential equation, while the other compartments were investigated by three different structure models described in Figure 6. The mathematical presented in the single organ model has been shown in the Appendix B section. As the result, a perfusion-limited model structure could perfectly describe the shape of plots and the estimated parameters in kidneys, heart, lungs, and spleen compartments. The liver concentration-time profile could be described by a perfusion-limited model, permeability-limited model, and permeability-limited with deep in tissue (please see in Appendix B section Figure 17 and Table 20).

In the PBPK model development stage, initially, all organ structure was assumed to fit into a perfusion-limited model before the liver model structure was modified to improve the model fitting profiles (please see in Appendix C section Figure 18 and Table 21). In this stage, numerous PBPK models were generated. Thus, the best fit model was selected based on visual inspection of the model fitting profiles and the AIC values. The reasonability of estimated parameters was assessed by the %CV of individual parameter estimates (158).

The final PBPK model consists of five different physiological organ compartments in the body: (1) lungs, (2) fat, (3) liver, (4) slowly perfused tissues, and (5) rapidly perfused tissues which were connected by blood circulation as demonstrated in Figure 7. Those tissues in this model were included because of their important role in the pharmacokinetics of Andro. Lungs were selected because they are an important target of action of Andro for COVID-19 treatment. Due to the lipophilicity properties of Andro (the partition coefficient between n-octanol and water (log P) = 2.51) (64), the accumulation of Andro in fat was expected. Therefore, the fat compartment was added to the model. Although, no concentration of Andro in

fat was available, adding the fat compartment into the model improved the goodness of fit by reducing AIC from 283 to 262 and still provide relatively good reliability of parameter estimation. The slowly perfused organ lumped together were from skin, bone, and muscles, whereas the rapidly perfused tissues lumped together were from the brain, gut, heart, kidneys, spleen, and the rest of the body. The liver is selected because Andro is mainly metabolized by the phase II enzyme in the liver. A perfusion-limited model was used to describe Andro distribution into each tissue. Next, the model with first-order oral absorption was developed by using the same disposition parameters as in the disposition PBPK model. However, the gut compartment was not included in the model because adding the gut compartment into the model increases the uncertain parameters over the data generating process. Additionally, the predicted concentration-time profile in the gut may be inaccurate because the concentration of Andro in the gut was unavailable.
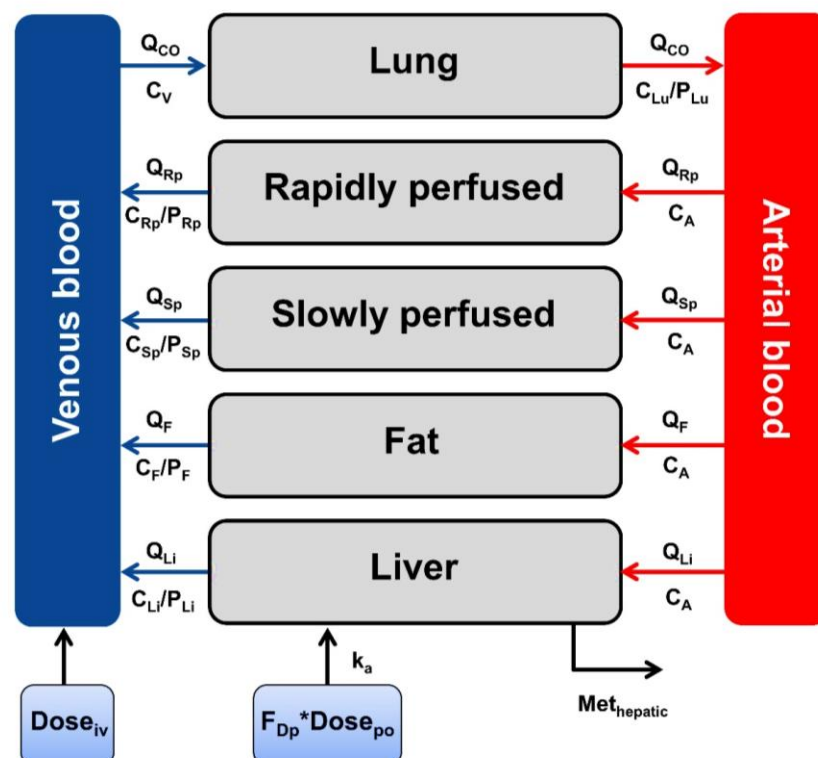
Figure 7 A physiologically based pharmacokinetic (PBPK) model for andrographolide

Abbreviations: Q, C, and P are tissue blood flow rate, andrographolide concentration, and partition coefficient for tissue to blood, respectively. The subscriptive including CO, Lu, Li, Rp, Sp, F, A, and V are cardiac output, lung, liver, rapidly perfused organ, slowly perfused organ, fat, arterial blood, and venous blood, respectively. $Dose_{iv}$ and $Dose_{oral}$ is a dose of andrographolide after iv and oral administration, respectively; F_{Dp} is Fraction dose reaching the hepatic portal vein; k_a is first-order absorption rate constant; Met_{Andro} is the mass of andrographolide metabolized *via* liver.

1. Mathematical Representations of the PBPK model of andrographolide

The plasma and tissue concentration-time courses of Andro in the model were described by differential equations and first-order kinetic equations. The blood flow that connected different compartments and volume were calculated from Brown et al. (156). The following equations were used to describe the PBPK model structure for Andro after intravenous and oral administration.

1.1 Venous compartment for intravenous administration

$$\frac{dA_V}{dt} = \left(Q_{Li} \times \frac{C_{Li}}{P_{Li}}\right) + \left(Q_{Rp} \times \frac{C_{Rp}}{P_{Rp}}\right) + \left(Q_{Sp} \times \frac{C_{Sp}}{P_{Sp}}\right) + \left(Q_F \times \frac{C_F}{P_F}\right) - (Q_{CO} \times C_V) \quad \textbf{equation 11}$$

Venous blood concentrations (C_v): $C_V = \left(\frac{A_V}{V_V}\right)$ **equation 12**

Venous plasma concentrations ($C_{v,p}$): $C_{V,p} = \left(\frac{A_V}{V_V}\right)/R_{b:p}$ **equation 13**

Where Q_{Li}, Q_{Rp}, Q_{Sp} and Q_F are blood flow rate to the liver, rapidly perfused tissues, slowly perfused tissues, and fat, respectively; Q_{CO} is cardiac output; C_{Li}, C_{Rp}, C_{Sp}, and C_F, are the andrographolide concentrations in liver, rapidly perfused tissues, slowly perfused tissues, and fat, respectively; P_{Li}, P_{Rp}, $P_{Sp,}$ and P_F are liver/blood partition coefficient, rapidly perfused tissues/blood partition coefficient, slowly perfused tissues/blood partition coefficient, fat/blood partition coefficient, respectively; A_v is the amount of andrographolide in venous blood; V_v is a volume of venous blood; $R_{b:p}$ is the blood to plasma ratio.

1.2 Arterial compartment

$$\frac{dA_A}{dt} = \left(Q_{CO} \times \frac{C_{Lu}}{P_{Lu}}\right) - ((Q_{Li} + Q_{Rp} + Q_{Sp} + Q_F) \times C_A) \qquad \textbf{equation 14}$$

$$C_A = \left(\frac{A_A}{V_A}\right) \qquad \textbf{equation 15}$$

Where C_{Lu} and C_A are the andrographolide concentration in the lungs and arterial blood; A_A is the amount of andrographolide in arterial blood; V_A is a volume of arterial blood; P_{Lu} is lung/blood partition coefficient.

1.3 Liver compartment for oral administration

In mice, dogs, and humans, Andro metabolism was described by the Michaelis-Menten equation.

$$\frac{dA_{Li}}{dt} = \left(Q_{Li} \times \left(C_A - \frac{C_{Li}}{P_{Li}}\right)\right) - \left(\frac{V_{max} \times \left(\frac{C_{Li}}{P_{Li}} \times f_{up}\right)}{K_m + \left(\frac{C_{Li}}{P_{Li}} \times f_{up}\right)}\right) + (F_{Dp} \times k_a \times Dose_{oral}) \qquad \textbf{equation 16}$$

$$\frac{dA_{Gut}}{dt} = -k_a \times Dose_{oral} \qquad \textbf{equation 17}$$

$$C_{Li} = \left(\frac{A_{Li}}{V_{Li}}\right) \qquad \textbf{equation 18}$$

Where A_{Li} is the amount of andrographolide in the liver; V_{Li} is a volume of the liver; V_{max} is the maximum velocity of the metabolic reaction of andrographolide; K_m is the binding affinity of andrographolide; f_{up} is fraction unbound in plasma; F_{Dp} is a fraction of dose reaching the portal vein; k_a is first-order absorption rate constant; $Dose_{oral}$ is oral dose.

Because of no reported values of V_{max} and K_m of Andro in rats, V_{max} and K_m were replaced by the hepatic intrinsic clearance of Andro (CL_{int}) under conditions of first-order elimination. Therefore, equation 16 was rewriting as equation 19 for the rat PBPK model.

$$\frac{dA_{Li}}{dt} = \left(Q_{Li} \times \left(C_A - \frac{C_{Li}}{P_{Li}}\right)\right) - \left(CL_{int} \times \left(\frac{C_{Li}}{P_{Li}} \times f_{up}\right)\right) \qquad \textbf{equation 19}$$

Non-elimination organs i.e., fat, slowly perfused tissues, and rapidly perfused tissues:

$$\frac{dA_T}{dt} = \left(Q_T \times \left(C_A - \frac{C_T}{P_T}\right)\right) \qquad \textbf{equation 20}$$

$$C_T = \left(\frac{A_T}{V_T}\right) \qquad \textbf{equation 21}$$

Where Q_T is blood flow rate to tissues; C_T is the andrographolide concentration in tissues; A_T is the amount of andrographolide in tissues; V_T is a volume of tissues; P_T is tissue/blood partition coefficient.

1.4 Lung compartment

$$\frac{dA_{Lu}}{dt} = \left(Q_{CO} \times \left(C_V - \frac{C_{Lu}}{P_{Lu}}\right)\right) \qquad \textbf{equation 22}$$

$$C_{Lu} = \left(\frac{A_{Lu}}{V_{Lu}}\right) \qquad \textbf{equation 23}$$

2. Model Parameterization

The physiological parameters of body weight, volume, and blood flow fraction of each organ compartment were calculated using a study by Brown et al as presented in Table 16 (156). The body weight of mice, rats, dogs, and humans were assumed to be 0.02, 0.225, 10, and 70 kg, respectively.

2.1 Species-Specific Physiological Parameters

The physiological parameters of cardiac output, volume, and blood flow fraction of each organ compartment were listed in Table 16 (188, 189). Note that, the fraction of volume of slowly perfused organ (V_{SpC}) was the sum of volume of muscle, bone, and skin, whereas the fraction of volume of rapidly perfused organ (V_{RpC}) was equal to 1- V_{SpC}. The fraction of blood flow of slowly perfused organ

(Q_{SpC}) was the sum of blood flow of muscle, bone, and skin, whereas the fraction of blood flow of rapidly perfused organ (Q_{RpC}) was equal to 1- Q_{SpC}. Blood cardiac output (Q_{CO}) values in mice, rats, dogs, and humans are calculated based on allometric relationship, as follows: $Q_{CO, mice}$ (L/h) = 16.5*(BW(kg))$^{0.75}$; $Q_{CO, rats}$ (L/h) = 14.1*(BW(kg))$^{0.75}$; $Q_{CO, dogs}$ (L/h) = 0.063*(BW(g))$^{0.75}$; $Q_{CO, humans}$ (L/h) = 15*(BW(kg))$^{0.74}$. For interspecies scaling, the tissue blood flow (Q_T) and the tissue volume (V_T) for each species was calculated by mass-to-volume conversion using equation 24 and 25, respectively (188).

$$Q_T(L/h) = Q_{TC} \times Q_{CO} \qquad \text{equation 24}$$

$$V_T(L) = V_{TC} \times BW(kg) \qquad \text{equation 25}$$

Table 16 Species-specific physiological used in the development of the PBPK model of andrographolide in mice, rats, dogs, and humans

Description of parameters	Symbol	Mice	Rats	Dogs	Humans	Authors
Cardiac output (L/h)	Q_{CO}	0.878	4.606	63.000	347.908	Brown et al.
Fraction blood flow						
Rapidly perfused	Q_{RpC}	0.410	0.289	0.226	0.430	
Slowly perfused	Q_{SpC}	0.339	0.458	0.407	0.291	Brown et al.
Fat	Q_{FC}	0.090	0.070	0.070	0.052	
Liver	Q_{LiC}	0.161	0.183	0.297	0.227	
Fraction volume						
Lung	V_{LuC}	0.007	0.005	0.008	0.008	
Rapidly perfused	V_{RpC}	0.163	0.150	0.098	0.093	
Slowly perfused	V_{SpC}	0.656	0.667	0.629	0.580	
Fat	V_{FC}	0.070	0.070	0.150	0.214	Brown et al.
Liver	V_{LiC}	0.055	0.034	0.033	0.026	
Venous	V_{VC}	0.037	0.0555	0.062	0.059	
Arterial	V_{AC}	0.012	0.0185	0.021	0.020	

2.2 Chemical Specific Parameters

All chemical-specific parameters used in the PBPK model were summarized in Table 17.

2.2.1 Partition Coefficient

The f_{up} value, which was obtained from Panossian et al., (36) was reported as 0.45 and used to calculate the initial P_T values of lungs, fat, liver, slowly perfused organ, and rapidly perfused organ in mice based on equations 8-10. Next, these values were estimated using the plasma and tissue concentration-time profiles reported by Tu et al. (34). For interspecies scaling, the estimated P_T values from the mice PBPK model were used across species.

2.2.2 Metabolism Parameters

In this study, *in vivo* K_m values for mice, dogs and humans were assumed to be equal to *in vitro* K_m those were reported for the corresponding species by Tian et al. (190). The V_{max} for mice was estimated from the intravenous data in the model development process. For the estimation, an initial value of V_{max} was extrapolated from the mice liver microsome (MLM) by using equation 26. Due to the limitation of tissue distribution data of other species after intravenous administration, the metabolism parameters were not estimated. The CL_{int} of rat and V_{max} values of dog and human used in the PBPK model were extrapolated from the previously reported corresponding values from rat liver microsome (RLM), dog liver microsome (DLM), and human liver microsome (HLM) by using equation 26-27 (128, 190).

$$V_{max} = V_{max,in\ vitro} \times MPPGL\ \left(mg\ \frac{protein}{g} liver\right) \times Liver\ mass\ (g\ per\ kg\ BW) \times BW\ (kg)$$

equation 26

$$CL_{int} = CL_{int,in\ vitro} \times MPPGL\ \left(mg\ \frac{protein}{g} liver\right) \times Liver\ mass\ (g\ per\ kg\ BW) \times BW\ (kg)$$

equation 27

The rat microsomal intrinsic clearance ($CL_{int, rat}$) was reported as 0.0944 mL/min/mg protein (128). The microsomal V_{max} values were reported as 1.56, 0.77, and 0.21 nmol/min/mg protein for mice, dogs, and humans, respectively (190). The microsomal protein content per gram of liver (MPPGL) values of mice, rats, dogs, and humans was reported as 45, 45, 45, and 39.46 mg protein/g liver, respectively (191-193). The liver weight for mice, rats, dogs, and humans were 87, 36, 30, and 18 g/kg, respectively (188, 193).

2.2.3 Absorption Parameters

According to the result of the sensitivity analysis in the Results section, both fraction of an orally administered dose that reaches the hepatic portal vein (F_{Dp}) and k_a had a high impact on the predictive performance to predict AUC of Andro (Table 19 in the Results section). Additionally, k_a had a high impact on the simulated C_{max}. However, the values of k_a and F_{Dp} were unknown in most of the studies and were affected by formulations in each study. In the case of F_{oral}, there were reported only in mice and rats, but the reported values were in the range of 0.0119-0.0927 (9, 12, 25, 184). It was a 9-fold difference and implied the high variation of the value among the studies. Therefore, the values of k_a and F_{Dp} of each study were estimated while the values of the disposition parameters were fixed as the values demonstrated in Table 17.

Subsequently, the F_{oral} of each study in Table 17 was calculated using the following equation: $F_{oral} = F_{Dp}*F_H$ where F_H was the fraction of the dose that escaped hepatic first-pass metabolism. The F_H value was calculated as one minus the hepatic extraction ratio (E_H), which was obtained using the following equation: $E_H = (f_{up}*CL_{int})/(Q_{Li}+f_{up}*CL_{int})$ where f_{up} is the fraction unbound in plasma.

Parameter Estimation

For the iv PBPK model, the disposition parameters were estimated in mice as described in the model parameterization section. Initially, the biochemical parameter of V_{max} was scaled up from *in vitro* value to *in vivo* value using equation 26. Next, it was estimated, while the binding affinity of Andro (K_m) was fixed as 68.70 µmol/L (37).

For the oral PBPK model, the estimated disposition values from the iv PBPK model in mice were used across species. The metabolism parameters for rats, dogs, and humans were mentioned previously. The k_a value was unknown and was affected by the formulation. The F_{oral} were reported only in mice (0.0927) and rats (0.0267-0.0300), whereas dogs and humans have no report. In addition, it was a 9-fold difference and implied the high variation of the value among the studies. Therefore, the absorption parameters of each study were estimated by fixing the values of disposition and metabolism parameters.

The blood, plasma, and tissue concentration-time data were fitted simultaneously using maximum likelihood in ADAPT5 with the additive and proportional variance model as shown in equation 28.

$$Var(t) = (\sigma_1 + \sigma_2 * Y(t))^2 \qquad \textbf{equation 28}$$

Where Var(t) is the variance associated with the model output, σ_1 and σ_2 are the additive and proportional variance parameters. The goodness of fit was assessed by visual inspection and on the AIC. The reliability of parameter estimation was assessed by the asymptotic coefficients of variation of individual parameter estimates.

Model Evaluation

In this study, the predictive performance of the PBPK model was evaluated based on the visual inspection and factor of two. The predicted Andro levels in plasma and/or tissues should be around the center of the observed dataset and should be within the standard deviation of the observed dataset, but not excess 1.96-fold of the observed dataset (95% confidence intervals). The proportion of the predicted pharmacokinetic parameters (e.g., area under the curve (AUC), and maximum concentrations (C_{max})) should be within 2-fold of the observed values (194-196). The performance of the PBPK model in mice was evaluated using the independent experimental intravenous and oral dataset which was available in mice (Table 15).

Interspecies extrapolation has been another way to perform the model evaluation. Thus, the extrapolated PBPK models to rat, dog, and human were evaluated using the reported data set from each species as shown in Table 15. Note that the PBPK model for oral administration was semi-external evaluated which the absorption parameters were estimated as mentioned in the previous section.

Sensitivity Analysis

In this PBPK model, the local sensitivity analysis (SA) was used to assess parameter uncertainty and to identify sensitive model parameters that had an impact on two model outputs including area under the curve and maximum concentration in blood or plasma and lung (170, 197). Each parameter was increased by 0.1% and those model outputs were computed. A normalized sensitivity analysis (NSC) was calculated using equation 29 (198).

$$NSC = \frac{\frac{A-B}{B}}{\frac{C-D}{D}}$$ **equation 29**

Where A is the simulated model output resulting from a 1% increase in parameter value, B is the model output resulting from the original parameter value, C is the parameter value increased by 1% and D is the original parameter value.

If the absolute value of NSC (|NSC| is greater than 1, it suggests amplification of parameter error (198). The relative influence of each parameter on the model output was categorized as |NSC| >0.5 was high impact, |NSC| = 0.2-0.5 was moderate impact and |NSC| < 0.2 was low impact (199).

***In silico* GastroPlus® Simulation**

A commercial PBPK model, the ACAT (advanced compartmental absorption and transit) with perfusion-limited PBPK model in GastroPlus® version 9.8 was used to compare the simulated plasma concentration-time profile with an observed profile from the evaluation study in humans (Table 15). The parameterization and parameter values used in the GastroPlus® simulation has been described in Table S3.

The simulation was conducted assuming immediate release formulation. The dissolution rates of the formulation were predicted using a modification of the Nernst-Bruner dissolution equation which is the default in GastroPlus® (200). The default log D model in GastroPlus® was used to model the passive absorption rate of dissolved substance from the gut lumen to enterocytes. The Log D calculation has been described in the Appendix section. The *in vivo* intestinal effective permeability in humans ($P_{eff,human}$) was extrapolated from the rat permeability ($P_{eff,rat}$) using equation 30 (161). The $P_{eff,rat}$ was obtained from the study of Gao et al (201).

$$P_{eff,human} = 3.6 \times P_{eff,rat} + 0.03 \times 10^{-4} \qquad \textbf{equation 30}$$

According to the simulation, the fraction of dose absorbed that enters the enterocytes (F_A), the fraction of dose escaping gut metabolism (F_G), F_{Dp}, F_H and F_{oral} were predicted. Note that F_{Dp} is equal to F_A*F_G.

Herb-drug interaction assessment

In order to preliminary assess the possible herb-drug interaction caused by Andro, the maximum concentration of free Andro in human liver at a steady state ($C_{max\_Li\_u,\ ss}$) after multiple oral administration of 20 mg/kg q 8 h were predicted. This dosage was selected because it is 2 times higher than the effective dosage regimen for HIV treatment during a small clinical trial (17). The $C_{max\_Li\_u,\ ss}$ to the inhibition rate constant (Ki) proportional was used to judge the possible interaction follows the criterion by the European Medicines Agency (EMA) guideline and the United States Food and Drug Administration (US FDA) (202).

Based on the EMA guideline, the possible interaction occurred when a certain cut-off value (x) was ≥ 1. This was calculated by the following equation is fulfilled: ($C_{max\_Li\_u,\ ss}$ /Ki) ≥ x. Whilst the US FDA provided the R value as the criteria. If the R value was larger than 1.1, the herb-drug interaction was likely to appear. This value was calculated by the following equation is fulfilled: ($C_{max\_Li\_u,\ ss}$ /Ki)+1 (202).

Monte Carlo Simulation

MC simulation is a useful method for exploring the simulated pharmacokinetics and subsequence response due to inter-subject variation (170, 172). The use of MC simulation with the extrapolated PBPK model of Andro in humans was conducted to preliminary evaluate whether the proposed dosages of Andro in patients with COVID-19 can achieve the efficacy threshold of the free Andro in the lungs and will not reach toxicity thresholds in lung and liver. The proposed dosage regimens were including 60 mg q 8 h which was recommended by the department of Thai traditional and alternative medicine (22, 203), and 200 mg q 8 h. The efficacy thresholds were assumed to be the reported IC_{50} values of Andro in the lung cell line for the production of the SAR-CoV-2 virus (0.034 μM) (204). The toxicity thresholds were assumed to be the reported value of half-maximal cytotoxicity concentration (CC_{50}) of Andro in the lung (58.3 μM) and liver cell line (44.55 μM) (204)**.**

Influenza A virus is the cause of high morbidity and mortality rate in humans. The current therapeutics drugs have been limited by side effects and resistant viral strains (66). The alveolar epithelial cell, the epithelial covering of the bronchi, and bronchioles have been the targets of influenza infection (205). Based on an *in vitro*, Andro could inhibit the H9N2, H5N1, and H1N1 with IC_{50} values of 94.3, 121.7, and 110.0 μM, respectively (66). Although this demonstrated a low degree of inhibition effect when compared to ribavirin, the inhibition effect toward NF-κB of Andro might be beneficial. Since the mechanism of action of Andro involves decreasing NF-κB thorough the covalent modification of reducing cys62 of p50 with an IC_{50} value of 15 μM. Therefore, the predicted Andro levels in lungs should be over than the efficacy thresholds which was assumed to be the reported IC_{50} value of Andro inhibited NF-κB activation (15 μM) (206).

The inflammatory in the lung could be the cause of airways swelling and mucus-producing. This makes it more likely to develop asthma. Nitric oxide (NO) has been playing a role in the pathogenesis of inflammation. The excessive amount of NO caused by the inducible nitric oxide synthase (iNOS) could generate inflammatory disorders of the joints, gut, especially, lungs (86). The granulocyte-macrophage colony-stimulating factor (GM-CSF) and tumor necrosis factor-α (TNF-α) have been

two of many cytokines which are both the non-specific inflammation and the allergic inflammation. GM-CSF has been played an important role in the recruitment of eosinophils to produce the asthmatic lung. Whereas TNF-α also induced the general inflammatory response in the asthmatic airways (90). Andro has demonstrated relatively good anti-inflammatory in the lung when compared to the reference drug. This diterpenoid might be used for asthma therapeutic. Based on *in vitro*, Andro could inhibit NO synthesis by reducing the expression of the iNOS protein with an IC_{50} value of 7.90 µM (87, 88). In addition, Andro showed the inhibition potential of GM-CSF and TNF-α with IC_{50} values of 3.30 µM and 0.60 µM (90). Therefore, the Andro levels in the lungs should be over than the efficacy thresholds which was assumed to be the reported IC_{50} values of Andro inhibition GM-CSF and TNF-α activities.

Andro has been demonstrated a relatively high anti-platelet aggregation activity when compared to Ginkgo extract and Aspirin (71, 73). According to Lu et al., the platelet aggregation mechanism has been described as the pathway follows: the collagen binds to its receptors and then activates both the phospholipase C gamma 2-protein kinase C (PLC2γ2-PKC) and inositol triphosphate kinase (IP3K) /Akt-MAPKs cascades. Next, the p38 MAPK activated cPLA2 which catalyzes the production of arachidonic acid (AA). The catalyzed AA further produced the thromboxane A2 (TxA_2) formation and more released calcium ($Ca2^+$). This results in platelet activation and aggregation. The diterpenoid namely Andro could inhibit the platelet aggregation *via* the endothelial nitric oxide synthase (eNOS) pathway. In brief, when the eNOS was simulated by Andro, the amount of cyclic GMP will more be generated. The increase of cyclic GMP resulted in inhibition of both IP3K and TxA_2 production, thus, the $Ca2^+$ releasing was inhibited, and, finally, the platelet activity was inactivated (58). Based on the above information, it was assumed that the main mechanism of Andro play role in the plasma compartment. Therefore, the predicted Andro levels in lungs should be over than the efficacy thresholds which was assumed to be the IC_{50} value of Andro inhibited platelet aggregation (35 µM) (58).

Andro has shown relatively good anti-malaria activity when compared to artesunate. Using *in vitro* model, this diterpenoid is effective against *Plasmodium falciparum* erythrocytic stages with IC_{50} of 9.1 µM (11). Also, the blood schizontocial activity was inhibited by Andro with the IC_{50} of 34.70 µM, and the gametocyte was

killed by this diterpenoid with the IC_{50} of 10.30 µM (84). Therefore, we decided to simulate the Andro levels in plasma in order to predict the appropriate dosage for malaria treatment.

The MC method that involved random sampling was used to generate 1000 simulated concentration-time profiles of free Andro in the human plasma and lung for each dosage regimen (172). All parameters distribute randomly around their mean values were in Tables 16 and 17. Note that all parameters in our developed PBPK model were used in the MC simulation for the same dose (200 mg) using in the model evaluation in humans. The CV of each PBPK parameter was assigned to specify inter-subject variation as shown in Table S4. The CV of all physiological parameters, except BW, were used accordingly to the values suggested by Price et al (207). In order to avoid being underweight and overweight, the CV of BW was set to 10%. Based on the default values of previously published PBPK models, the CV values of partition coefficient were 20% and the CV of other chemical specific parameters was 30% (168). Fraction blood flow and fraction volume were randomly assigned values from normal distributions. Body weight, partition coefficient, and other chemical specific parameters were randomly assigned values from log-normal distributions. To avoid physiological implausible value, the distributions of the parameters were truncated at 3 standard deviations to represent 99% of the population (172).

Computer software

The observed Andro plasma and tissue concentration from each pharmacokinetic study were extracted using Digitizer software (version 2.3.3). The PBPK model development was performed using ADAPT5 (version 5.0.58). The SA and MC were conducted by using Berkeley Madonna version 8.3.18 (Berkeley Madonna Inc.). GastroPlus® software was used to compare the simulated plasma concentration-time profile with an observed profile in humans.

CHAPTER IV

RESULTS

This section represents the results of this study. The results were divided into three main sections as follows: 1) Development of mice PBPK model; 2) Model Evaluation; 3) Simulation of Dosage Regiment Design in Humans. The detail on each step is described below.

Development of mouse PBPK model

After the liver model structure was modified, a perfusion-limited model which is the simplest model was the best assumption to describe the drug distribution because modifying the liver model structure did not improve goodness of fit and did not provide relatively good reliability of the estimated parameter (please see in Table S2). The comparison model fitting plots have been shown in Figure 20.

The final PBPK model, which is developed based on an intravenous dataset in mice, consists of the lung, fat, liver, rapidly, and slowly perfused organ as shown in Figure 7. The estimated metabolism and disposition parameters showed relatively good precision. The scaled-up maximum velocity of Andro (V_{max}) from the mice microsomal study (37) was 7.33 µmol/h while the estimated V_{max} from iv PBPK model for mice was 12.96 µmol/h with %CV equal to 2.7%. The proportion of predicted and observed was 1.77. In addition, the P_T values of the lung, fat, liver, and slowly perfused organ with relatively good precision except for P_T value of the rapidly perfused organ as demonstrated in Table 17. Also, using the data by Tu et al., the *in vivo* partition coefficient ($AUC_{tissues}/AUC_{plasma}$) for lung and liver were 0.357 and 1.163, respectively (34). Whilst the estimated partition coefficient for lung and liver were 0.346 and 1.460, respectively. The proportion of the predicted and observed for P_{Lu} and P_{Li} are 0.97 and 1.26, respectively. A goodness of fit of the predicted Andro levels in plasma, lung, and liver over time is illustrated in Figure 8.
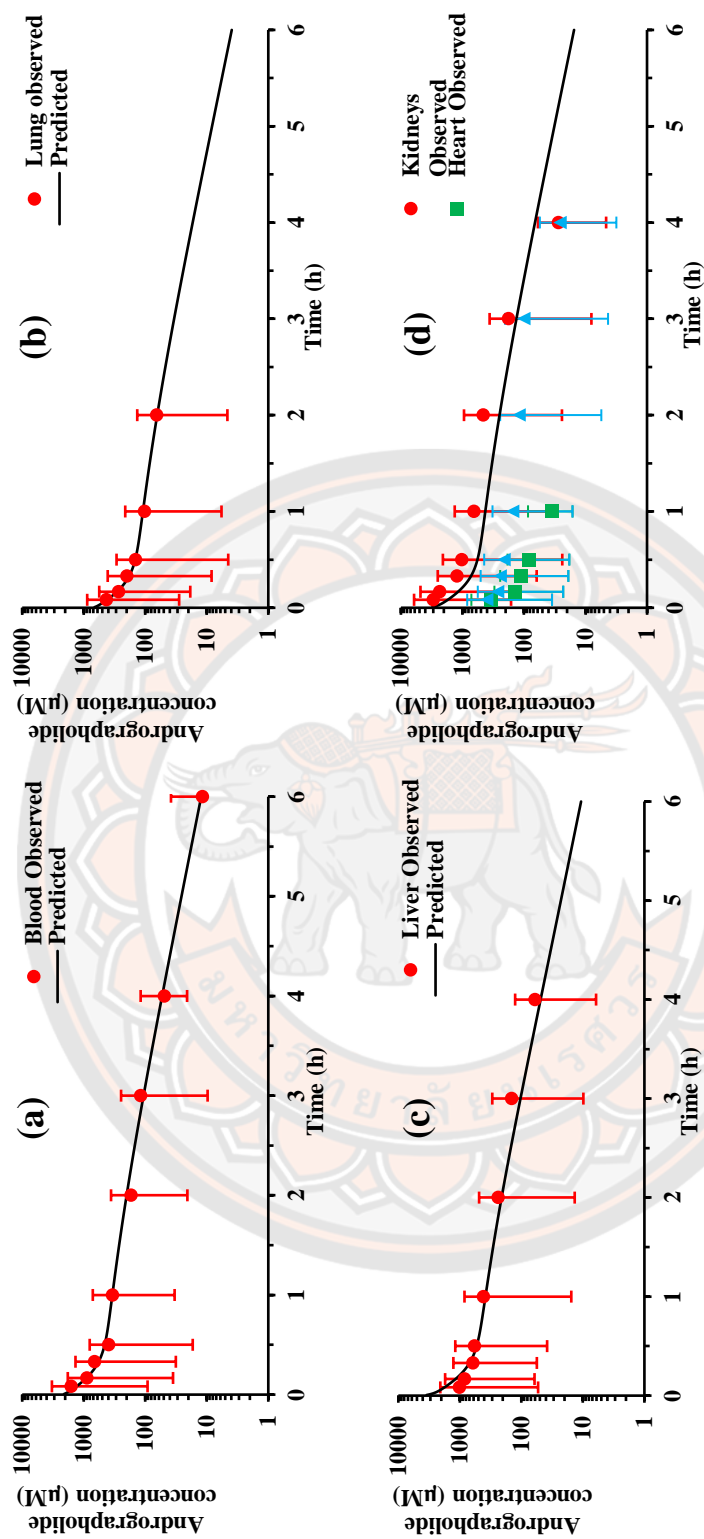
Figure 8 Predicted andrographolide concentration-time profiles in (a) plasma, (b) lung, (c) liver, and (d) rapidly perfused organs i.e., kidney, heart, and spleen following intravenous administration of 500 mg/kg andrographolide from the model-building data in mice (34). • - observed concentration, solid line- predicted concentrations, error bar - standard deviation of the observed data

Table 17 Estimation of the absorption, disposition, and metabolism parameters in the PBPK model in mice, rats, dogs, and humans

Description of parameters	Symbol	Mice	Rats	Dogs	Humans	Method/Reference
Partition coefficient tissue: plasma						
Lung	P_{Lu}	0.346[a] (5.0%)	-	-	-	Values in the mouse model were estimated by fitting the model to data reported by Tu et al., 2014 and the values were used in rats, dogs, and humans.
Rapidly perfused	P_{Rp}	1.326[a] (595.0%)	-	-	-	
Slowly perfused	P_{Sp}	0.424[a] (382.6%)	-	-	-	
Fat	P_F	27.040[a] (8.3%)	-	-	-	
Liver	P_{Li}	1.460[a] (10.1%)	-	-	-	
Protein binding						
fraction unbound in plasma	f_{up}	-	-	-	0.45	This value was acquired from Panossian et al., 2000
Blood to plasma ratio	$R_{b:p}$	-	0.93	-	-	This value was acquired from Bera et al., 2014
Metabolism parameters						
maximum velocity (μmol/h)	V_{max}	12.96[a] (2.7%)	NR	623.7[b]	626.5[b]	The V_{max} value for mice was estimated by fitting the model to data reported by Tu et al., 2014
binding affinity (μmol/L)	K_m	68.7[c]	NR	30.0[c]	3.06[c]	
Intrinsic clearance (L/h)	CL_{int}	0.189[d]	2.06[e]	20.79[d]	204.7[d]	
Hepatic extraction ratio	E_H	0.376	0.524	0.333	0.538	This value was calculated using equation follows; $E_H = (f_{up}*CL_{int})/(Q_H + f_{up}*CL_{int})$
Absorption parameters						
Absorption rate constant (h^{-1})	k_a	1.384[a] (14.8%)	0.770[a] (14.1%)	0.097[a] (16.6%)	0.245[a] (10.2%)	The k_a and F_{Dp} values for mice, rats, dogs, and humans were estimated by using the data reported by Banerjee et al.,2016, Bera et al., 2014, Zhang et al., 2015, and Xu et al., 2009 respectively.
Fraction dose reaching the hepatic portal vein	F_{Dp}	0.042[a] (9.3%)	0.050[a] (10.0%)	0.016[a] (12.4%)	0.137[a] (7.6%)	
Fraction of andrographolide that escaped hepatic first-pass metabolism	F_H	0.624	0.476	0.667	0.462	This value was calculated using the equation follows; $F_H = 1-E_H$ (hepatic extraction ratio)
Oral Bioavailability	F_{oral}	0.026	0.024	0.097	0.063	This value was calculated using the equation follows; $F_{oral} = F_{Dp}*F_H$

Q_{Li} = liver blood flow; and NR = no report

[a] is the estimated values with percentage coefficient of variation (%CV) were acquired from model estimation

[b] is the initial value of V_{max} for mice was calculated by equation 16 using V_{max} reported by Tian et al., 2015

[c] is the values of K_m for mice, dogs, and humans was reported by Tian et al., 2015

[d] is the CL_{int} value has been calculated from V_{max}/K_m

[e] is the CL_{int} for rats was calculated by equation 17 using CL_{int} obtained from the study of Zhao et al., 2013
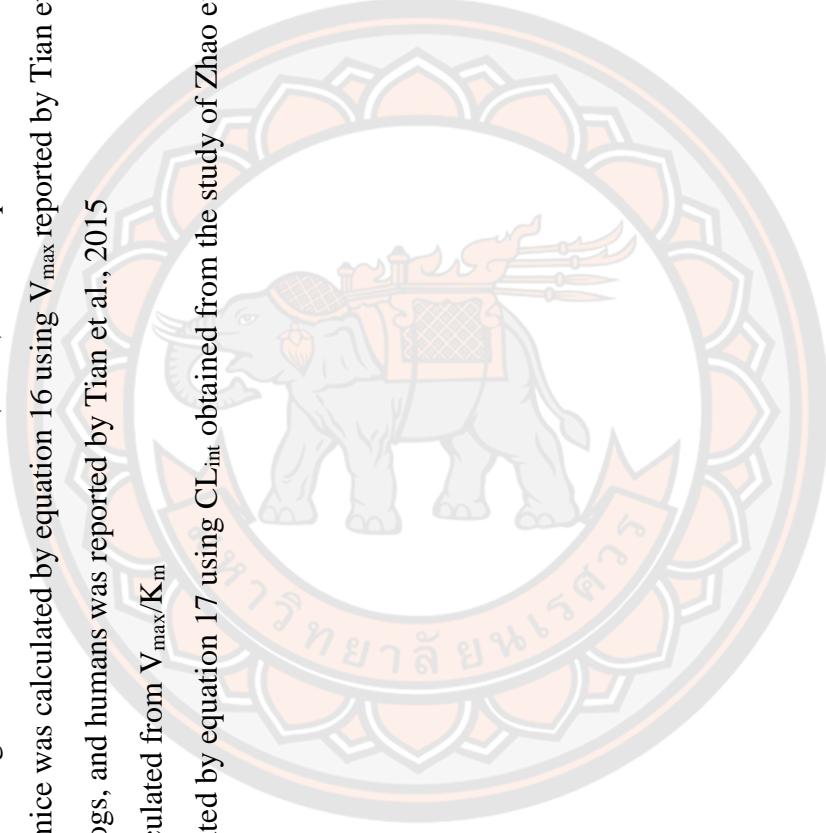
Model Evaluation

The performance of the PBPK model was evaluated by comparing model simulations with experimental plasma (independent dataset) and interspecies extrapolation.

1. Model Evaluation in mice

Using the evaluation dataset in mice, the PBPK model was reasonably described as the observed data, but the simulated lines showed some deviation as illustrated in Figure 9a. Additionally, the model was applied to predict Andro concentration-time profile in plasma mice after oral intakes at 50 mg/kg. The estimated metabolism and disposition parameters from the iv PBPK model were fixed, whereas the absorption parameters were estimated. The model predicted was in good agreement with the observed data from hour zero to sixth (Figure 9b). The predicted AUC and predicted C_{max} of the evaluation dataset in mice were within 2-fold of the observed values as illustrated in Table 18.

2. Extrapolation of the model to rats following intravenous injection

According to the studies in Table 17, the intravenous datasets in rats from four studies were used for externally model evaluation. The CL_{int} value for rats was obtained from Zhao et al. (128) and it was scaled up using equation 27, whereas the disposition parameters were obtained from the iv PBPK model. The mode simulated was satisfactorily described the observed data acquired from Yen et al., and Ye et al., whereas the simulated lines showed some deviation in the terminal phase of the observed data acquired from Jiang et al., Yang et al. (25, 112, 126, 173, 208). The comparison model simulated Andro plasma concentration-time courses in rats after single oral administration were illustrated in Figure 10. The proportional of predicted to observed AUC values were within 2-fold (Table 18). However, the proportional of predicted to observed C_0 value was more than 5-fold. These results might be explained by the variance between studies which may be caused by some errors during the experiment, thus, a 100-fold difference of C_0 value from the studies by Yang et al., and Yen et al. was observed after intravenous injection of Andro at 5 mg/kg.
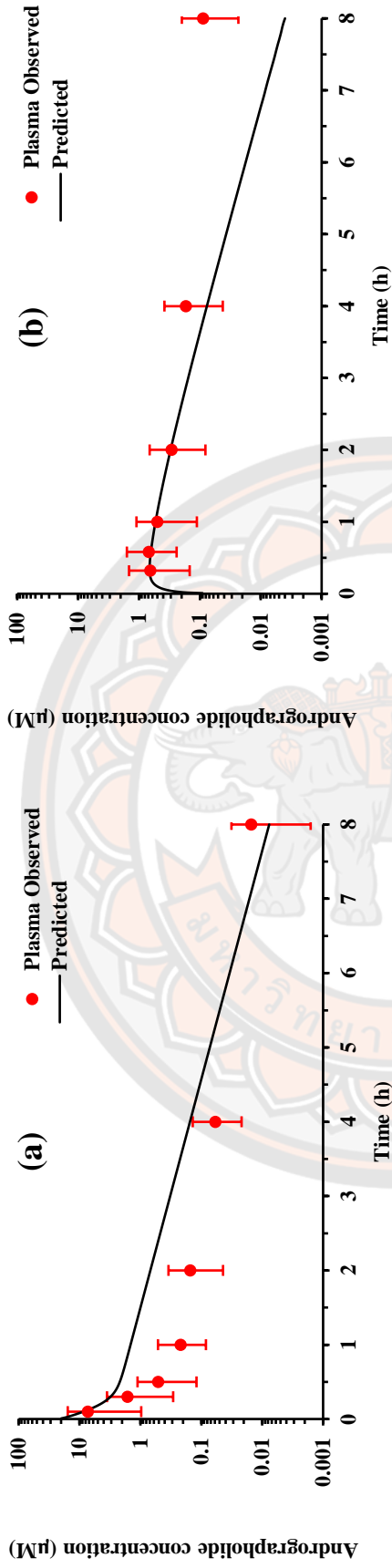
Figure 9 Predicted mice plasma concentration-time profiles of andrographolide following (a) intravenous injection of 5 mg/kg and (b) oral administration at 30 mg/kg from the validation data in mice (12). • - observed concentration, solid line- predicted concentrations, error bar - standard deviation of the observed data
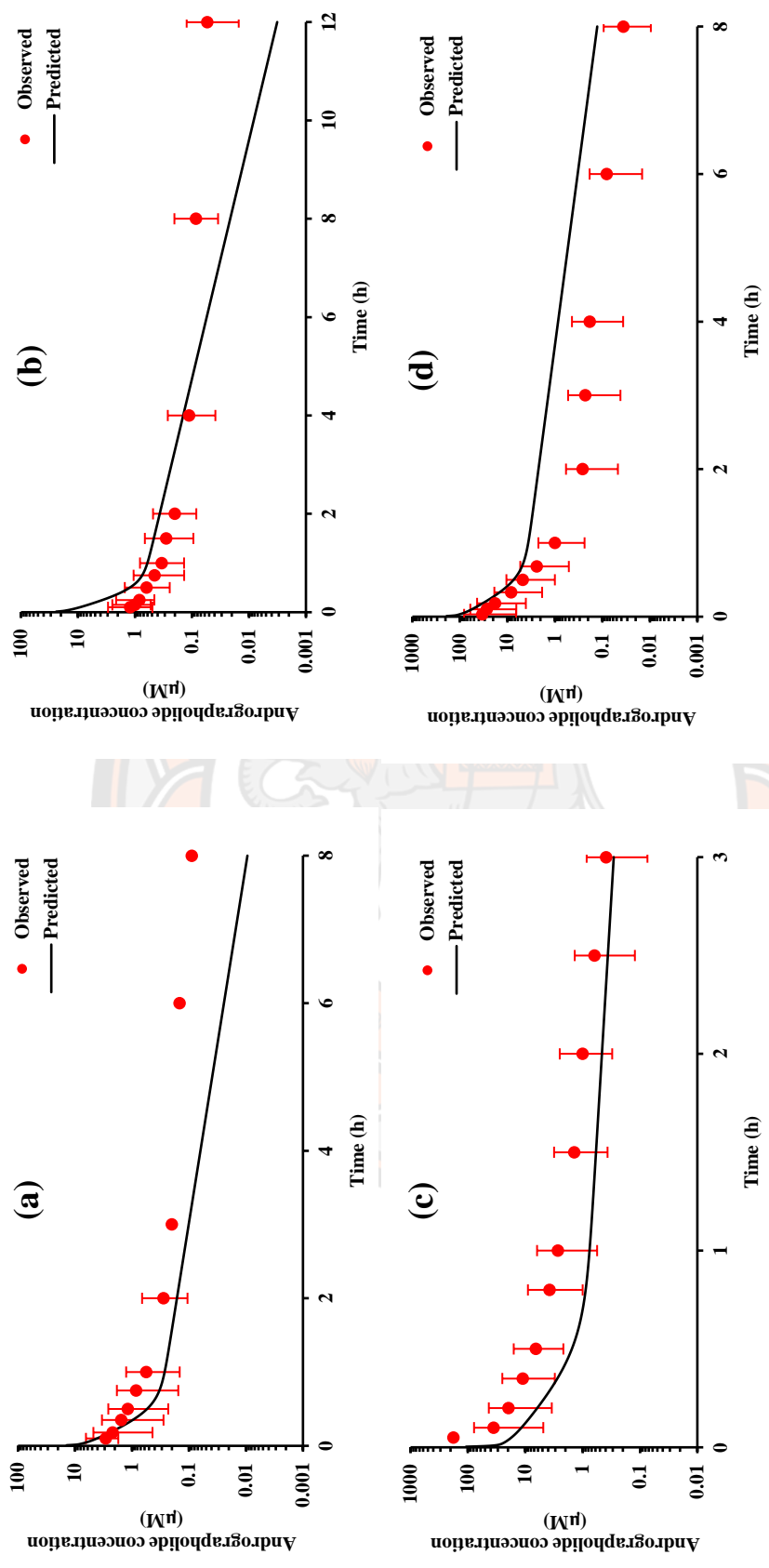
Figure 10 Predicted andrographolide concentration-time profiles from the externally model validation data set in rats. following intravenous injection at (a) 2 mg/kg, (b) 5 mg/kg, (c) 5 mg/kg, and (d) 24 mg/kg. following intravenous injection at (a) 2 mg/kg, (b) 5 mg/kg, (c) 5 mg/kg, and (d) 24 mg/kg. • - observed concentration obtained from (a) Jiang et al. (157), (b) Yang et al. (119), (c) Yen et al. (105), and (d) Ye et al. (22), solid line- predicted concentrations, error bar - standard deviation of the observed data

Table 18 Observed versus predicted pharmacokinetic parameters of Andro

Dose (mg/kg)	Route of administration	C_{max} or C_0 (µmol/L)			T_{max} (h)			Plasma $AUC_{0\text{-}inf}$ (µmol/L.h)			Authors (year)
		Observed	Predicted	P/O	Observed	Predicted	P/O	Observed	Predicted	P/O	
Model development in mice											
500	Single iv dose	2876.10[a]	1899.51[a]	0.66	-	-	-	1161.41[a]	1223.68[a]	1.05	Tu et al. (2014)
Model evaluation in mice											
5	Single iv dose	14.57[b]	16.67[a]	1.14	-	-	-	2.52[b]	6.14[a]	2.44	Banerjee et al. (2016)
50	Single oral dose	0.73[b]	0.66[a]	0.90	0.42[b]	0.25[a]	0.60	2.33[b]	1.51[a]	0.65	
Model evaluation and extrapolation to rats											
30	Single oral dose	0.33[b]	0.33[a]	1.00	0.75[b]	0.50[a]	0.67	0.79[b]	0.79[a]	1.00	Bera et al. (2014)
100	Multiple oral dose	0.82[a]	0.73[a]	0.89	1.00[a]	1.00[a]	1.00	3.42[b]	2.40[a]	0.70	
Model evaluation and extrapolation to dogs											
15	Single oral dose	0.09[b]	0.04[a]	0.44	3.29[b]	2.00[a]	0.61	0.86[b]	0.89[a]	1.03	Zhang et al. (2015)
Model evaluation and extrapolation to humans											
2.86	Single oral dose	0.17[b]	0.11[a]	0.65	1.60[b]	1.50[a]	0.94	0.81[b]	0.88[a]	1.09	Xu et al. (2009)
Externally model evaluation in rats											
2	Single iv dose	4.11[a]	7.86[a]	1.91	-	-	-	3.69[b]	2.04[a]	0.55	Jiang et al. (2014)
5	Single iv dose	1.77[a]	18.05[a]	10.20	-	-	-	2.67[b]	4.69[a]	1.76	Yang et al. (2013)
5	Single iv dose	178.63[a]	25.98[a]	6.88	-	-	-	28.53[b]	5.19[a]	5.50	Yen et al. (2018)
24	Single iv dose	36.95[a]	134.97[a]	3.65	-	-	-	10.81[b]	28.43[a]	2.63	Ye et al. (2011)

$AUC_{0\text{-}inf}$ is the area under the curve from zero to infinity; C_{max} is maximum concentrations; C_0 is concentrations at time zero;

T_{max} is time to C_{max} value; P/O predicted value over observed value.

[a] is the values calculated using PK solver software with non-compartment analysis mode.

[b] is the values acquired from the reported values of the pharmacokinetics studies.

3. Extrapolation of the model to rats, dogs, and humans following oral dosing

A study in rats conducted by Bera et al. was a major study that represent all exposure scenarios and species as described in Method section 2.1. The predicted plasma concentration-time course from the extrapolated PBPK model was in good agreement with the observed values from rats after single oral administration of Andro at 30 mg/kg. The predicted and observed proportional of the C_{max}, T_{max}, and AUC_{0-inf} were within 2-fold. Using the tissue distribution data in rats, the predicted Andro levels in plasma, lungs, and liver of the extrapolated PBPK model were in good agreement with the observed data following repeated oral dosing of Andro at 100 mg/kg/day. The observed and predicted C_{max} of Andro in plasma were 0.82 and 0.73 µmol/L, respectively. Additionally, the observed AUC in plasma, lungs, and liver were 3.42, 0.73, and 1.12 µmol/L.h, respectively whereas the predicted AUC plasma, lungs, and liver were 2.40, 0.83, and 2.22 µmol/L.h, respectively. These predicted values were within 2-fold of the observed data. The comparison model predicted was illustrated in Figure 11. The results of other studies in rats (Table 17) are demonstrated in the Appendix section (Figure 20-23).

In addition, the PBPK model was further extrapolated using the experimental dataset in beagle dogs by Zhang et al. (187). The ability of model prediction was satisfactorily described the observed data in dogs following single oral dosing of 15 mg/kg Andro as illustrated in Figure 12. The predicted and observed proportional of the C_{max}, and AUC was 0.44, and 1.03, respectively. Despite no studies that reported the %F_{oral} value for dogs has been undertaken, the extrapolated PBPK model predicted such a value of 9.70%.

In humans, the model predicted Andro levels in human plasma overtime after single oral administration at 2.83 mg/kg was satisfactorily described when compared to the experimentally observed dataset acquired from Xu et al. (209). The model fitting of plots was presented in Figure 12. The predicted C_{max} and AUC of the extrapolated dataset were within 2-fold of the observed values. Additionally, the percentage difference of C_{max} and AUC were calculated as 42.86% and 8.28%, respectively. To our knowledge, there is no report of the %F_{oral} value in humans, however, our developed model could predict the %F_{oral} value of 6.30%.
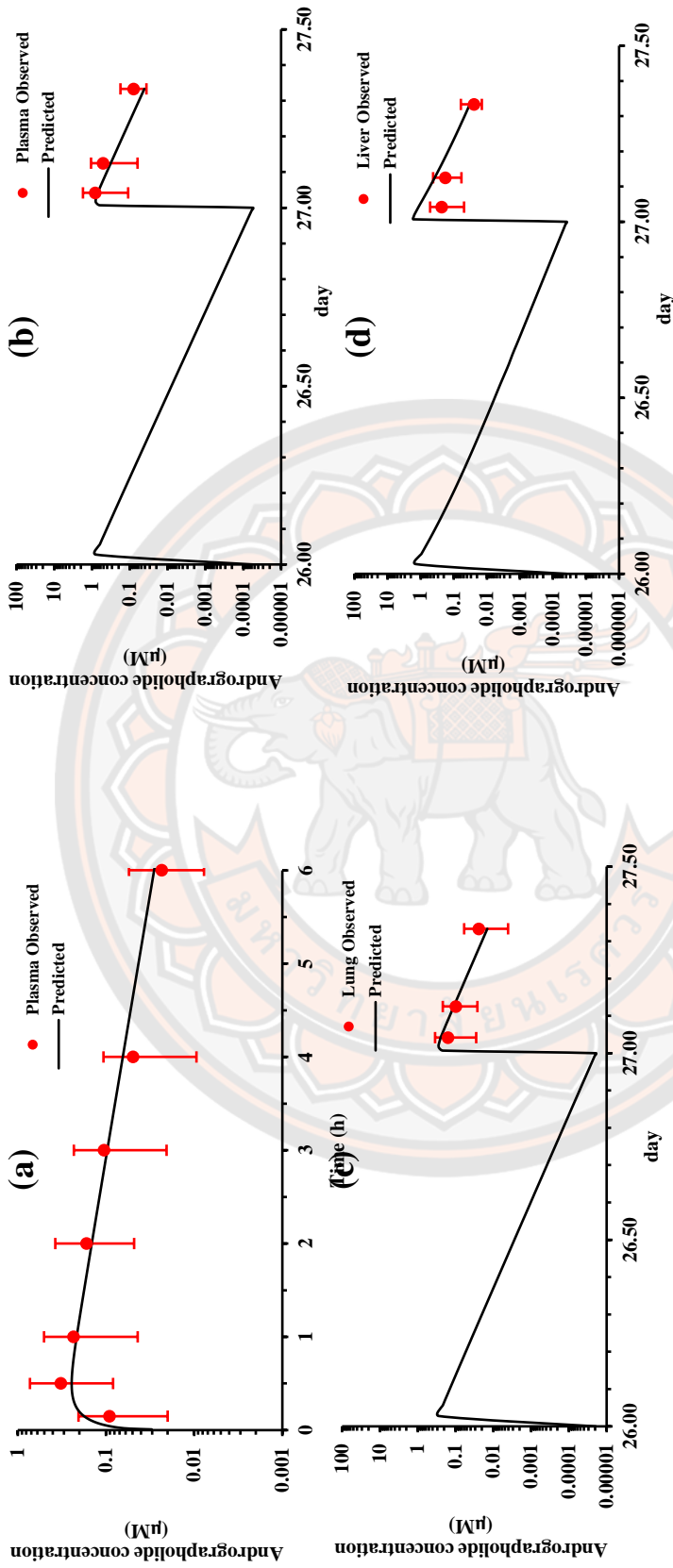
Figure 11 Predicted concentration-time profiles following (a) single oral administration of 30 mg/kg and multiple oral administration at 100 mg/kg in rat (b) plasma, (c) lung, and (d) liver. • - observed concentration obtained from Bera et al.(**35**), solid line- predicted data, error bar - standard deviation of the observed data
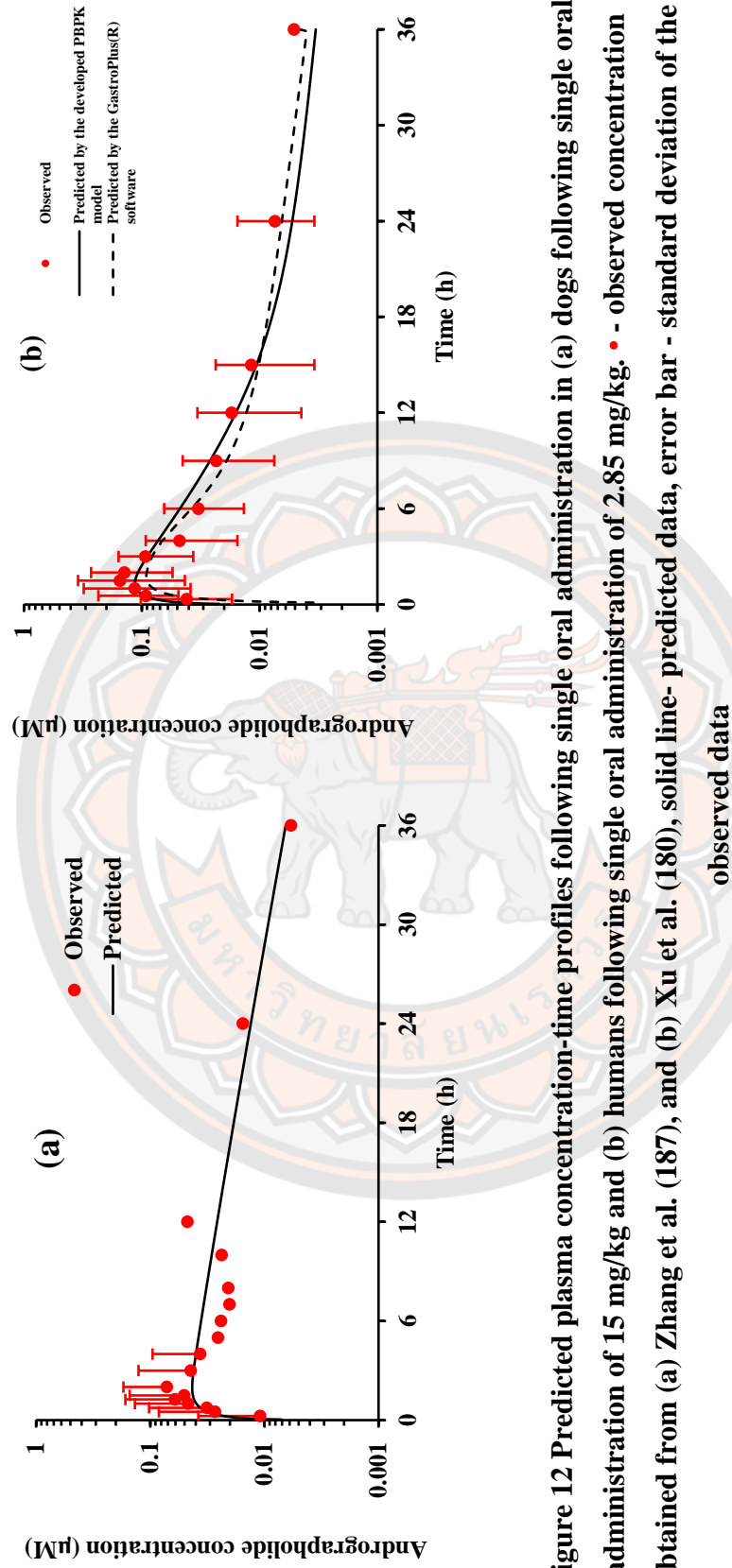
Figure 12 Predicted plasma concentration-time profiles following single oral administration in (a) dogs following single oral administration of 15 mg/kg and (b) humans following single oral administration of 2.85 mg/kg. ● - observed concentration obtained from (a) Zhang et al. (180), and (b) Xu et al. (187), and (b) Xu et al. (180), solid line- predicted data, error bar - standard deviation of the observed data

4. Evaluation of F_{oral} of the PBPK model

To evaluate the ability of the model for estimation of F_{oral} using oral data in mice and rats, the studies by Banerjee et al., Chen et al., Ye et al., and Yen et al were used. However, the ability of the model for F_{oral} estimation could not be evaluated in the dog and human because there are no studies that reported F_{oral} values. The reported %F_{oral} value of the pharmacokinetic study by Banerjee et al., Chen et al., Ye et al., and Yen et al., were 9.27%, 1.19%, 2.67%, and 3.00%, respectively (9, 25, 184, 210). Whereas, the predicted %F_{oral} value of such studies were 2.60%, 2.20%, 0.90%, and 1.20%, respectively. Although the estimated F_{oral} was within 3-fold of the observed values, the proportional of predicted and observed AUC were within 2-fold. The model predicted Andro levels in mouse and rat plasma were satisfactorily described when compared to the experimental dataset as illustrated in Figures 9b and 13a-c.

5. GastroPlus® Simulation

Following single dose of 200 mg Andro, Figure 12b demonstrated that the plasma concentration-time curve simulating by the developed PBPK model was comparable to the curve simulating by GastroPlus®. The predicted F_{oral}, F_{Dp} and F_H values by GastroPlus® were very close to those values predicted by the developed PBPK model (Table S4, S6). Only 55.2% of the 200 mg dose was predicted by GastroPlus® to be dissolved in intestinal lumen fluid, subsequently, the fraction of dose absorbed (F_A) was 0.552 (Figure 23). Based on the GastroPlus® simulation, about 75% of the F_A of Andro was absorbed into enterocytes in duodenum and jejunum, and the rested was absorbed in ileum. Figure 14 illustrated that F_{oral}, F_A and F_{Dp} but not F_G and F_H decreased with the increasing of doses in the range of 20 mg to 1000 mg.
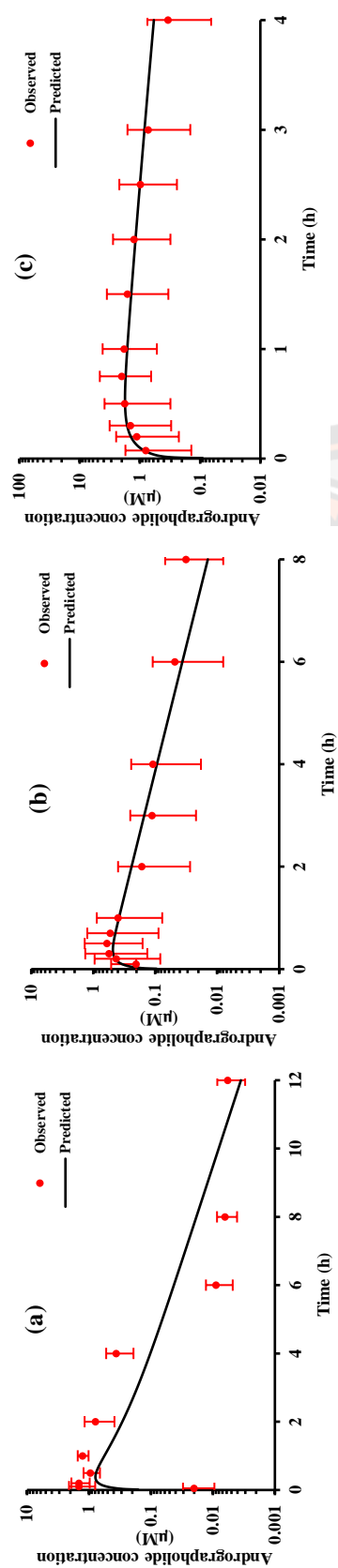
Figure 13 Predicted concentration-time profile in rat plasma following single oral administration at (a) 50 mg/kg, (b) 120 mg/kg, and (c) 300 mg/kg. • - observed data acquired from (a) Chen et al., 2014, (b) Ye et al., 2011, and (c) Yen et al., 2018, solid line- predicted data, error bar - standard deviation of the observed data
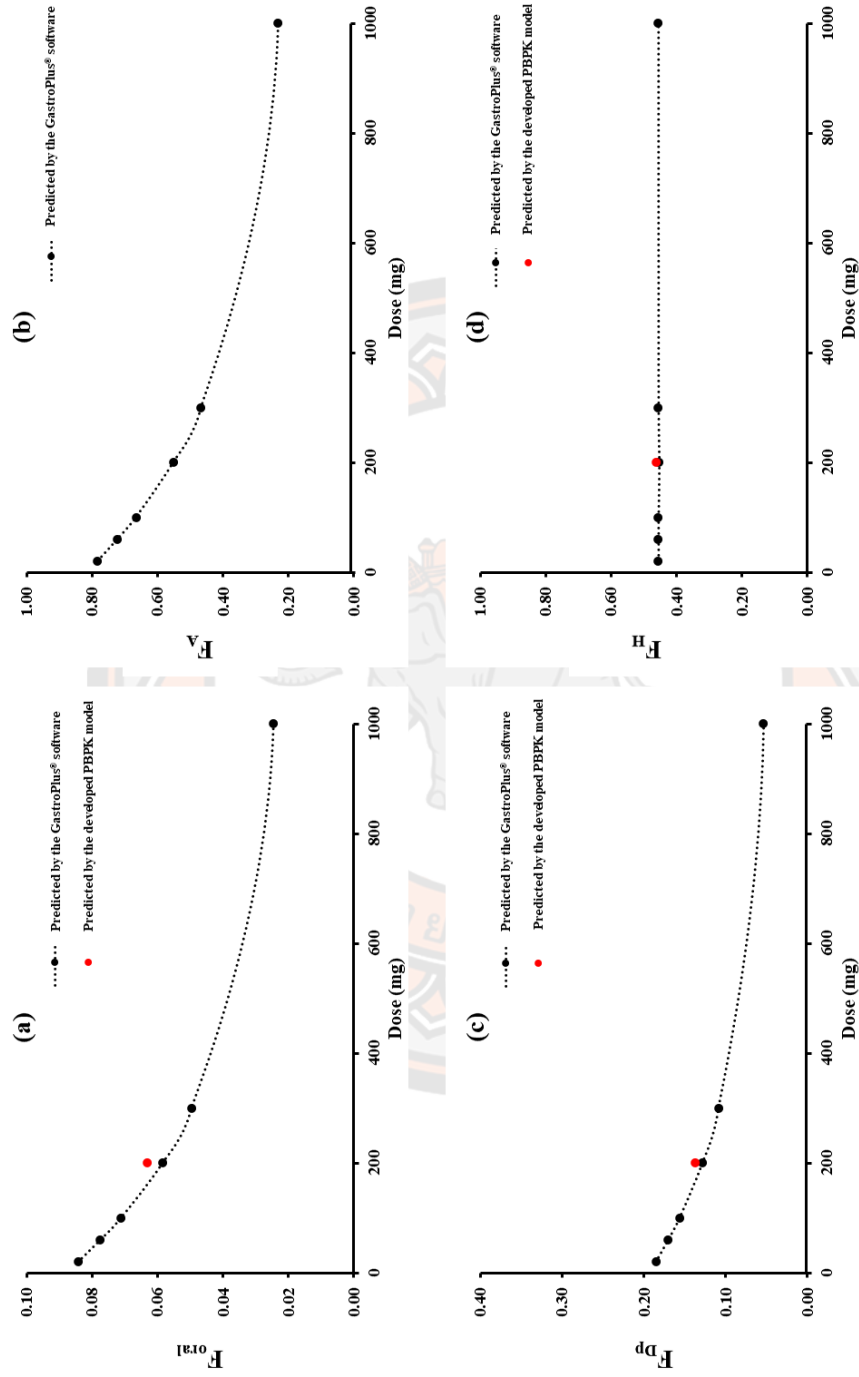
Figure 14 Comparison of the predicted (a) oral bioavailability (F_{oral}), (b) fraction of dose absorbed (F_A), (c) the fraction of dose reaching the portal vein (F_{Dp}), and (d) the fraction of dose escaping hepatic first-pass metabolism (F_H) values at different dosages of andrographolide using GastroPlus® software

6. Sensitivity Analysis

The SA was conducted both in mouse and human. The NSC values for the mouse and the human PBPK model regarding AUC and C_{max} were calculated as shown in Table 19. After intravenous administration of Andro in the mouse, dose dependent of NSC regarding AUC was observed. After intravenous injection of 5 mg/kg in mouse, the body weight, f_{up}, fraction of blood flow rate for fat, liver, slowly perfused organ and rapidly perfused organ had a relatively high impact on the simulated blood AUC when the absolute NSC more than 0.5. Additionally, the fraction volume for fat had been demonstrated a moderately impact on the blood AUC while the other fraction volume did not show any else impaction on the model output. After the higher dose (500 mg/kg), the blood AUC was dependent on the same parameters. However, the fraction volume for fat demonstrated relatively high with the absolute NSC value of 5.2 while the fraction volume for liver, rapidly perfused organ, venous blood, and arterial blood had additionally moderately impacted on the model output.

After single oral administration of 2.86 mg/kg of Andro in humans, the physiological parameters including the fraction volume for fat, the fraction blood flow rate for liver, fat, slowly perfused organ, and rapidly perfused organ demonstrated relatively high impact (absolute NSC >0.5) on plasma AUC while other fraction volumes did not show any impaction on plasma AUC. These values also demonstrated the impaction on the maximum Andro concentration in plasma ($C_{max, plasma}$) and lung (C_{max, Lu_u}) with the same manner to impact on AUC. The results came out the way it should, that the blood flow rate for each tissue should have a moderate to high impact on the model. Since our developed PBPK model was constructed based on the perfused-limited assumption.

In addition, the SA results in humans, the biochemical parameters including F_{Dp}, and f_{up} had a relatively high impact on both plasma AUC and $C_{max, plasma}$ whereas f_{up} had a moderate impact on C_{max, Lu_u}. The K_m had a moderate impact on both plasma AUC, $C_{max, plasma}$, and C_{max, Lu_u}. Although a parameter that represents the absorption process of Andro such as k_a value had a slight impact on plasma AUC, it demonstrated a relatively high impact on $C_{max, plasma}$, and C_{max, Lu_u}. Additionally, the partition coefficient for each tissue had a low impact on all model output. Therefore,

the uncertainty of the model output after single oral administration in a human was heavily dependent on the values of F_{Dp} and k_a. Due to no report of the values of both parameters, thus, the estimation of both parameters was needed as previously mentioned in Method section 3.2.2.3.

Herb-drug interaction assessment

Based on the preliminary herb-drug interaction assessment of Andro, multiple oral administration of Andro at 60-1400 mg q 8 h did not produce the possible interaction followed the EMA guideline and the US FDA criteria. Since the *x* value of Andro at 1400 mg was 0.09 while the *R* value was 1.09. Although increasing the dosage might seem to be unlikely the possible interaction followed the EMA guideline, the herb-drug interaction caused by Andro might appear when using the US FDA criterion. Therefore, the maximum therapeutic dosage regimen should be within 1400 mg q 8 h.

Simulation of Dosage Regiment Design in Humans

Figure 15a demonstrated the prediction of free Andro concentrations in lungs after the oral administration of Andro at 60 mg q 8 h and 200 mg q 8 h. It indicates that only a small fraction of simulated healthy humans who orally administer 60 mg q 8 h of Andro achieved the efficacy threshold (IC_{50} equal to 0.034 µM). Whereas oral administration of 200 mg q 8 h of Andro provided enough concentrations of free Andro for the majority of the healthy humans to achieve the efficacy threshold in lungs but lower than the toxicity threshold in lungs (CC_{50} equal to 58.3 µM). The simulated $C_{max, ss}$ and $C_{min, ss}$ of free Andro in the liver after oral administration of 200 mg q 8 h were 0.085 ± 0.042 µM and 0.035 ± 0.044 µM, respectively. The $C_{max, ss}$ was lower than the toxicity threshold in the liver (CC_{50} equal to 44.6 µM). Therefore, this dose might be the appropriate dosage regimen in COVID-19 patients who have mild to severe symptoms with or without lung infection.

Unfortunately, even though Andro has several pharmacological activities such as anti-influenza virus, anti-platelet aggregation, anti-malaria activity, and anti-inflammatory in lungs, the predicted $C_{min, ss}$ of free Andro in human plasma and lungs after multiple oral administration of Andro at 1400 mg q 8 h for 5 days were 0.312

and 0.291 µM. The model predicted were lower than the efficacy threshold which was assumed to be the reported IC_{50} values of Andro against influenza virus thorough NF-κB inhibition pathway (15.0 µM), anti-platelet aggregation (35.0 µM), anti-malaria activity (9.10 µM), and anti-inflammatory in lungs thorough TNF-α inhibition pathway which is beneficial for asthma treatment (0.60 µM).

Table 19 Sensitivity analysis of the certain parameters in mice and humans after receiving a single intravenous and single oral dose of Andro, respectively

	Mice				Humans					
	(iv administration at 5 mg/kg)		(iv administration at 500 mg/kg)		(po administration at 2.86 mg/kg)					
	Response: AUC_{Blood}		Response: AUC_{Blood}		Response: AUC_{Plasma}		Response: $C_{max,\,plasma}$		Response: $C_{max,\,Lu\_u}$	
	Parameter	Rank	Parameter	Rank	Parameter	Rank	Parameter	Rank	Parameter	Rank
	BW	15.62	BW	-32.93	BW	<-0.01	BW	<-0.01	BW	<-0.01
Fraction blood flow										
	Q_{Li}	-1.17	Q_{Rp}	0.99	Q_{Li}	1.31	Q_F	-3.48	Q_F	-8.29
	Q_F	1.03	Q_{Sp}	0.99	Q_{Sp}	1.00	Q_{Li}	1.96	Q_{Li}	4.69
	Q_{Rp}	1.00	Q_{Li}	0.45	Q_{Rp}	1.00	Q_{Sp}	1.07	Q_{Sp}	2.36
	Q_{Sp}	0.99	Q_F	0.21	Q_F	0.87	Q_{Rp}	0.99	Q_{Rp}	2.55
Fraction volume										
	V_F	-0.47	V_F	-5.18	V_F	-0.57	V_{Rp}	-0.55	V_{Rp}	-1.32
	V_{Li}	-0.07	V_{Li}	-0.41	V_{Rp}	0.02	V_V	-0.34	V_V	-0.82
	V_{Rp}	-0.04	V_{Rp}	-0.38	V_V	-0.01	V_A	-0.34	V_A	-0.81
	V_V	-0.03	V_V	-0.29	V_A	-0.01	V_{Sp}	-0.24	V_{Sp}	-0.57
	V_A	-0.03	V_A	-0.28	V_{Li}	-0.01	V_{Li}	-0.12	V_{Li}	-0.29
	V_{Sp}	-0.01	V_{Sp}	-0.12	V_{Sp}	-0.01	V_{Lu}	-0.12	V_{Lu}	-0.28
	V_{Lu}	-0.01	V_{Lu}	-0.10	V_{Lu}	<-0.01	V_F	-0.04	V_F	-0.09
Biochemical										
	f_{up}	-1.33	f_{up}	1.55	F_{Dp}	7.38	F_{Dp}	7.42	F_{Dp}	7.41
	V_{max}	-0.05	P_{Sp}	-0.19	f_{up}	-2.08	ka	3.23	ka	3.23
	P_{Sp}	-0.02	V_{max}	-0.06	R_{bp}	-1.07	f_{up}	-1.77	f_{up}	0.46
	K_m	0.01	P_{Rp}	-0.05	K_m	0.31	R_{bp}	-1.07	P_{Sp}	-0.32
	P_{Rp}	<-0.01	P_{Li}	-0.02	ka	0.12	P_{Sp}	-0.32	K_m	0.26

Mice (iv administration at 5 mg/kg)		Mice (iv administration at 500 mg/kg)				Humans (po administration at 2.86 mg/kg)					
Response: AUC_{Blood}		Response: AUC_{Blood}		Response: AUC_{Plasma}		Response: AUC_{Plasma}		Response: $C_{max, plasma}$		Response: $C_{max\_Lu\_u}$	
Parameter	Rank	Parameter	Rank	Parameter	Rank	Parameter	Rank	Parameter	Rank	Parameter	Rank
P_{Li}	<-0.01	P_F	-0.01	P_{Sp}	-0.01	K_m	-0.01	K_m	0.26	P_{Rp}	-0.04
P_F	<-0.01	K_m	<-0.01	P_F	<-0.01	P_{Rp}	<-0.01	P_{Rp}	-0.04	P_{Lu}	<-0.01
P_{Lu}	<-0.01	P_{Lu}	<-0.01	V_{max}	<-0.01	P_{Lu}	<-0.01	P_{Lu}	<-0.01	P_{Li}	<-0.01
				P_{Rp}	<-0.01	P_{Li}	<-0.01	P_{Li}	<-0.01	V_{max}	<-0.01
				P_{Li}	<-0.01	V_{max}	<-0.01	V_{max}	<-0.01	P_F	<-0.01
				P_{Lu}	<-0.01	P_F	<-0.01	P_F	<-0.01	R_{bp}	-

AUC_{Blood} is the area under the curve of andrographolide concentration in blood from time zero to the last measured; AUC_{Lu_u} is area under the curve of free andrographolide concentration in lung from time zero to the last measured; AUC_{plasma} is the area under the curve of andrographolide concentration in plasma from time zero to the last measured; $C_{max, plasma}$ is the maximum andrographolide concentration in plasma; C_{max, Lu_u} is the maximum free andrographolide concentration in the lung. Results are expressed as the normalized sensitivity coefficient (NSC).
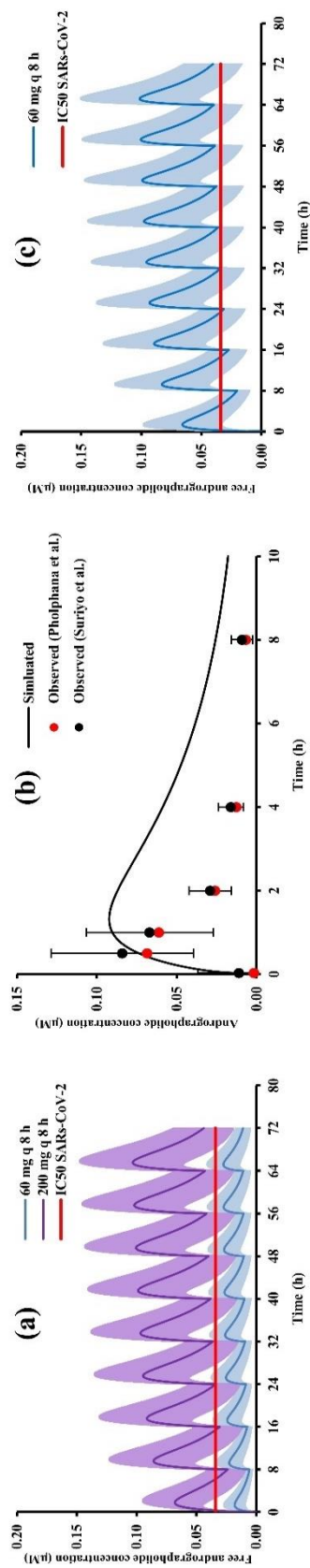
Figure 15 Monte Carlo simulation of dosage regiment design in humans. (a) Simulated free andrographolide concentration-time profile in lung humans after multiple oral administration of Andro at 60 mg q 8 h (Blue line) and 200 mg q 8 h (Purple line). The model output was expressed as mean with standard deviation. (b) Comparison model simulated andrographolide plasma concentration-time profiles in humans following oral administration of 1400 mg *A. paniculata* extract (equivalent to 32.64 mg of Andro). ● - observed data acquired from Pholphana et al. (211), ● - observed data acquired from Suriyo et al. (179), solid line- predicted data, error bar - standard deviation of the observed data. (c) Monte Carlo simulated free andrographolide concentration-time profile in lung humans following orally receiving of Andro at 60 mg q 8 h when the F_{Dp} value increasing 4.32-fold of Andro value (0.137)

CHAPTER V

DISCUSSION AND CONCLUSION

Discussion

In this study, we had collected the plasma and tissue concentration-time profiles of Andro in animals and humans using an electronic search in order to optimize the search and screen quality of the studies that were included for model development. Thus, our model was developed and evaluated based on available published data of the study using Andro, to avoid the possibility of either pharmacokinetic or pharmacodynamic interaction of Andro with other compounds in *A. paniculata* extract. Based on this PBPK model, the passive transport process mainly governs the distribution of Andro into each organ. Although, no study has investigated the degree of accumulation of Andro in fat, adding the fat compartment into the model is biologically plausible for the high lipophilic substance. The estimated partition coefficient of Andro for fat to blood is relatively high, thus it suggested that Andro might be extensively accumulated in fat.

To our knowledge, despite there were reported that 8.75% of Andro was renal excreted after oral consumption of *A. paniculata* extract, the percentage of renal excretion of Andro after the administration of Andro has not been assessed. In this reason, the addition of kidneys compartment to the model should be cautious. However, during the model development process, we tried to include a kidneys organ into the model, and we found that adding renal excretion into the model slightly increased goodness of fit but decreased precision of parameter estimation. It might be explained by a lack of available data on excreted Andro in urine after the administration of a Andro. Therefore, the renal excretion of Andro was not included in the developed model.

Enterohepatic recirculation is a feedback mechanism resulting from the combined role of the liver and intestine. This begins with drug absorption across the intestinal into the portal circulation before entering the liver. After that, the drug will be metabolized, followed by excretion through the bile duct and return to the

intestine, where the drug can be reabsorbed into the circulation (212). In accordance with Ye et al., only 5% of Andro was excreted thorough the bile duct after oral administration of Andro in rats [22]. Although the slight excretion thorough the bile duct was observed in an *in situ* study, the double peak of plasma concentration-time profiles after oral administration of Andro in rats was not observed. It was not only in rats, the double peak of plasma concentration-time profiles after oral administration of Andro in mice and humans were not observed also. Additionally, there have been no studies regarding the biliary excretion of Andro in either mice or humans. Therefore, we decided to develop the PBPK model without the biliary excretion in order to create the simplest model but essential elements characterizing a system. However, the biliary excretion of Andro in beagle dogs might be significant in the elimination process because the double peak of plasma concentration-time profile was observed after 12 h administered Andro (Figure 12a). In order to improve the fitting of the plot in the beagle dog, adding the biliary excretion into the model seemed to be reasonable.

The metabolism of Andro in the liver was well described by the developed PBPK model with the Michaelis-Menten equation. It is important to note that when using the first-order elimination equation instead of the Michaelis-Menten equation, the observed plasma concentrations of the validation of intravenous data in mice did not fit the model. However, the intravenous dose in the study using model development was 100 times higher than the intravenous dose in the study using model validation which shows in Table 15 (12, 34). This allowed us to note the significant differences in the clearance between both dosages using in the studies. Therefore, the Michaelis-Menten equation was tested and used to describe the metabolism of Andro in the model for mice, dogs, and humans. The estimated V_{max} from the iv PBPK model for mice (12.96 μmol/h) was in good agreement with the extrapolated V_{max} (7.3 μmol/h) from the mouse microsomal study (190). Based on our model, the saturation of the metabolism of Andro in humans would be observed at a very high dose (12 g q 8 h) which is unlikely to be used for therapeutic purposes. Whereas a study conducted by Wangboonskul et al. had previously mentioned the possibility of Andro having the saturation of metabolism processes after oral administration of high doses of *A. paniculata* tablets which are equivalent to 88.65 mg of Andro (213). However, there

is still no pharmacokinetic study of Andro in humans to confirm the saturation of metabolism of Andro.

The developed iv PBPK model had been applied to predict the plasma and tissue concentration-time profiles in either animals or humans following oral administration. Although the oral PBPK model assumed the simplest first-order absorption, the model predicted satisfactorily described the observed dataset (Figure 8-13). The predicted $\%F_{oral}$ values for mice and rats were not within 2-fold of the observed values but were within 3-fold of the observed values as mentioned in the result section. Although a 2-fold prediction error was acceptable for most drugs, 2.5-fold and 3-fold may be acceptable for drugs with high variability (194, 214).

However, even though the predicted $\%F_{oral}$ values from most of the studies that had only oral data were less than 10, the estimated $\%F_{oral}$ values of some studies in rats (Table S5) were higher than 50 which is abnormally high and reflects the unrealistic. These might be explained by the very high variation of the reported pharmacokinetic profiles among the oral studies in rats. The oral clearance (CL/F) of many studies was reanalyzed by using the non-compartmental method. The results (Table S5) showed that CL/F values had very high variation. Since the CL/F values were in the range of 0.04-79.35 L/h and the mean CL/F value was 17.23 L/h with the %CV of 141.50%. When the same values of disposition parameters were used in the oral PBPK model across all studies, the predicted $\%F_{oral}$ value of the studies, which had very low values of CL/F, were higher than others. Therefore, it was impossible for any model to fit all the data of those that had different pharmacokinetic profiles. A possible explanation of the very high variation of CL/F values among the studies in rats was the use of anesthesia during the studies. We found that most experiments that reported the use of anesthesia during experiments (Table S5) had lower CL/F values and had abnormally higher values of the estimated F_{oral}. The use of anesthesia was found to increase or decrease blood flow including liver blood flow (188). Based on our study, the pharmacokinetics of Andro was well described by the perfusion-limited PBPK model. Thus, blood flow was a rate-limiting step for the distribution of Andro into organs. According to the rat PBPK model, Andro had a moderate extraction ratio ($E_H = 0.524$), and thus the change of blood flow could affect both first-pass metabolism and hepatic metabolism.

One limitation of this study was that the oral PBPK model could not explain whether Andro is saturated in the absorption process. However, there has been a report of saturation of the absorption of Andro in the *A. paniculata* extract following the oral administration of 200 mg/kg in rats (36) while the saturation of Andro after oral intake of Andro has not been published. The saturation of absorption of Andro caused by the saturation of the uptake transporter is unlikely. Since Andro is high lipophilicity, the passive diffusion should be mainly responsible for the permeability of Andro into enterocytes. Additionally, the dissolution of Andro may become to hinder the precise prediction of Andro levels in plasma after oral administration since the dissolution profiles of Andro is low (a maximum of 17-30% release in different pH media) and the complete absorption model did not apply in our model (122, 201). According to Gao et al., in June 2021, a physiologically based absorption model (PBAM) with a classical three-compartment model has been published to describe the pharmacokinetics of Andro after oral administration in rats. The model modified the Nernst-Brunner dissolution rate equation into the absorption model. Therefore, the model was successfully used to simulate plasma concentration-time profiles after the oral administration of Andro and other modified cyclodextrin formulations in rats (201). In addition, the model is helpful for assessing the critical problem during *in vitro* formulations development. Due to the integration of the dissolution rate equation, it should be able to predict the saturation of absorption of Andro caused by the limit of solubility. The disadvantage of the model is that the first pass loss was not included in the model and was not able to predict the concentration of Andro in target organs. Therefore, integration of developed PBPK model by using the PBAM model instead of the first-order absorption should be further explored to improve the predictive performance of the model for oral formulations. This further modified model would be useful for prediction of the Andro concentrations in human target organ for newly developed oral formulation from the results of *in vitro* studies.

However, even though our developed PBPK model assumed the simplest first-order absorption, the model was able to predict F_{oral} within 3-fold of the observed value reported in mice and rat studies using different doses. In humans, there are no studies that reported the F_{oral} value, thus, it is reasonable to predict such value. The predicted F_{oral}, F_{Dp}, and F_H values after multiple oral administration of 200 mg Andro

were 0.063, 0.137, and 0.462, respectively. In order to confirm the precision of the developed model output, a mechanistically based simulation software namely GastroPlus® was used to predict such parameters. The predicted results were satisfactory because it was in good agreement with the F_{oral} (0.058), F_{Dp} (0.128), and F_H (0.455) values. In addition, based on simulated results from GastroPlus®, the saturation of the absorption of Andro occurred during the absorption of Andro from the gastrointestinal lumen to enterocytes. The F_{oral} and F_A values decreased when the dosage was increased as illustrated in Figure 14. Additionally, the low value of the predicted F_A by GastroPlus® at high dose suggested that decreasing F_A depends on the dose and limiting the dissolution of Andro in the gastrointestinal fluid.

According to the content described above, it is important to note that our PBPK model was developed using differential equations to describe the physiology/anatomy of different biological systems. Several *in vitro* and *in vivo* available data could be incorporated into the model to not only estimate pharmacokinetic parameters and plasma or drug levels in plasma and tissues but also to gain mechanistic insight into compound properties. Therefore, our model provided a mechanistic framework to understand and extrapolate pharmacokinetics and dose across *in vitro* and *in vivo* systems. Notably, our model also extrapolated dose across different species and populations.

Recently, the possibility of using Andro for COVID-19 treatment was widely discussed in Thailand. However, there is a limited amount of available published data on pharmacokinetics, pharmacodynamics, and clinical outcome in humans. Our study is the first to provide insight into pharmacokinetic information of Andro in human organs, especially in the lungs where is the important target for COVID-19 treatment. Using our developed PBPK model in mice and scale up to humans, the concentrations of Andro in the lungs were predictable. According to the reported IC_{50} (0.34 nmol/ml) against SAR-CoV-2 (204), the model predicted that the trough concentrations of free Andro at steady state ($C_{min, ss}$) of both plasma and the lungs following the oral Andro administration of 200 mg q 8 h were higher than the IC_{50} value in the majority of simulated humans as shown in Fig. 14a. Therefore, using the dosage regimen in humans, the efficacy of Andro in patients whose lungs were infected with SAR-CoV-2 might be expected. The dosages of Andro that are recommended in Thailand (60 mg

q 8 h) might be enough only in a minority of the simulated subjects (Figure 14a). Additionally, at 100 mg q 8 h might be enough in patients who have mild symptoms (The data did not show). However, as our model was developed and validated based on healthy subjects, severe COVID-19 patients with serious respiratory complications might lead to a change of Andro distribution into the lungs. Additionally, the appropriate dosage of Andro in obese patients should be further evaluated due to an estimated partition coefficient for fat to blood is relatively high. Therefore, the evaluation of the model in COVID-19 patients and obesity patients would be needed.

Based on the reported value of CC_{50} (204), the dosage regimens should not be equal or higher than 12 g q 8 h. The predicted concentrations in the liver of high dosage patients might induce hepatotoxicity. The selectivity index of Andro *in vitro* study over 380 indicates the safety of the compound (204), and its use for longer than 3 weeks should be done with caution. According to a small clinical trial with HIV positive patients, 4 of 13 patients who were administered Andro 5 mg/kg/day for 3 weeks and escalated to 10 mg/kg/day for 3 weeks had an Alanine Aminotransferase (ALT) level >100% above baseline at weeks 3rd and 5th and had an elevated value at week 6th. The mean ALT level of the patients at weeks 3rd and 6th were significantly higher than the mean baseline (17).

Herb-drug interaction can appear when herb and a given chemical drug are concomitantly consumed by either induction or inhibition of specific enzymes (138). Several *in vitro* studies using human liver microsome reported that the Andro has a weak inhibition to many CYP450 isoforms such as 1A2, 2B6, 2C9, 2E1, and 3A4 when IC_{50} values were >50 µM (215, 216). Additionally, Andro has been demonstrated moderate to strong inhibition on a phase II metabolism namely UGT2B7 when IC_{50} values were ≤10 µM (142, 143, 169, 216). In order to preliminary assess the possible interaction, the European Medicines Agency (EMA) guideline was applied to achieve the purpose. The herb-drug interaction is likely when a certain cut-off value (*x*) was ≥ 1. This is described by a basic model following condition is fulfilled: $([I]/K_i) \geq x$. The abbreviations have the following meanings: [I] is the unbound mean C_{max} in the liver, and K_i is the unbound inhibition contract (202). Based on the PBPK model simulated result, the unbound $C_{max, ss}$ in the human liver after oral administration of Andro at up to 20 mg q 8 h was 0.65 µM. The reported

unbound Ki value obtained by Uchaipichat et al. was 7.10 µM (142). Therefore, the calculated *x* value should be 0.09. This suggested that the herb-drug interaction is unlikely to appear. In order to confirm the possible interaction, a criterion that is recommended by the United States Food and Drug Administration (US FDA) was carried out. It has slight difference from the EMA guideline but both US FDA and EMA use a similar equation. The possible interaction is indicated when the *R* value was > 1.1. This is described by a basic model following condition is fulfilled: $R = 1+([I]/Ki)$ (202). When the equation was fulfilled by the same parameter values, a calculated *R* value was 1.09. Thus, the possible interaction is still unlikely to appear.

The mechanism-based PBPK model also was applied to predict the appropriate dosage regimen for influenza virus infection treatment, anti-platelet aggregation, anti-malaria activity, and asthma treatment. Unfortunately, the predicted $C_{min, ss}$ of free Andro in plasma and lungs in humans following repeated oral administration of 1400 mg Andro did not arrive at the efficacy threshold which was assumed to be the reported IC_{50} values of Andro. This might be overcome by co-administration of Andro and piperine which is a bioactive compound found in black pepper, long pepper, and other pepper. Since piperine could enhance the plasma concentration of Andro through P-gp inhibition potential (217). In addition, several studies reported that the Andro levels in plasma were a 3-fold increase in rats after single oral administration of the developed Andro formulation i.e., solid lipid nanoparticle, nanocrystals form, and nano-D-alpha-tocopherol polyethylene glycol 1000 succinate (29, 115, 118).

In order to solve the doubt whether oral administration of *A. paniculata* extract and Andro is different in term of the Andro level in human plasma, the developed PBPK model was applied. During model simulation, the distribution, metabolism parameters, as well as absorption rate constant, were not altered while the fraction Andro reaching the hepatic portal vein or F_{Dp} value was increased by 4.32-fold. Since a pharmacokinetic study by Chen et al. reported that the %F_{oral} value of Andro in rats after oral ingestion of Andro was 1.19% while the value in rats after oral intake of *A. paniculata* extract was 5.15% (9). The simulated Andro plasma concentration-time profile in humans following oral administration of 1400 mg *A. paniculata* extract (equivalent to 32.64 mg of Andro) was illustrated in Figure 14b.

The model simulated results turned out to be satisfactory, however, the model simulated showed some deviation in the terminal phase of the observed dataset acquired from Pholphana et al. (211), Suriyo et al. (179). According to Royal Thai Government Gazette (22), the dosage regimen of either *A. paniculata* powder or the crude extract should be dependent on the amount of Andro. The recommended dosage regimen of Andro has been 180 mg daily or 60 mg q 8 h. Therefore, our developed model was further applied to preliminary predict the Andro levels in human lungs after multiple oral dosing of 60 mg q 8 h. The simulated free Andro levels in human lungs after multiple oral administrations of *A. paniculata* extract which contains 60 mg of Andro was impressive because the predicted mean $C_{max, ss}$ and $C_{min, ss}$ had achieved the efficacy threshold but were lower than the toxicity threshold in lungs. Based on these results, it might suggest that consuming *A. paniculata* extract can provide higher Andro levels in human lungs than oral intake of Andro at the equivalent dose. However, the model simulated was not precise well because of two hypothesized factors. First, *A. paniculata* extract contains a large number of natural compounds, thus, the pharmacokinetics interaction between Andro and others is likely to appear. Second, the lack of actual Michaelis-Menten parameters for *A. paniculata* extract can misshape the fitting of plots also. This regard needs to be done in the future to improve the model simulation.

Conclusion

The perfusion limited PBPK model of Andro with a first-order absorption process was developed in mice and extrapolated to rats, dogs, and humans using all available information regarding the pharmacokinetics properties of Andro. Our model was successfully developed with various routes of administration following a single dose of intravenous, single oral administration, and multiple oral administration. The extrapolation PBPK model could be used to provide insight into the distribution of Andro in humans. Based on the simulation in humans, 200 mg q 8 h of Andro would provide concentration over IC_{50} value against SARS-CoV-2 activity in the lungs in the majority of healthy subjects. However, severe COVID-19 patients with respiratory defects might lead to the change of Andro distribution into the lungs, thus the prediction should be used with caution. The extensive accumulation of Andro in

fat was predicted, the appropriate dose of Andro for obese patients should be further explored. Unfortunately, although repeated oral intake of Andro at up to 1400 mg, the predicted $C_{min, ss}$ of free Andro in plasma and lungs did not over the efficacy threshold for anti-influenza virus activity, anti-platelet aggregation, anti-malaria activity, and anti-inflammatory in lungs. Additionally, the saturation of metabolism was observed after oral receiving of Andro at 12 g q 8 h whereas the saturation of absorption was still unclear. Notably, the possible herb-drug interaction of Andro is unlikely to appear after multiple oral administrations of 1400 mg Andro.
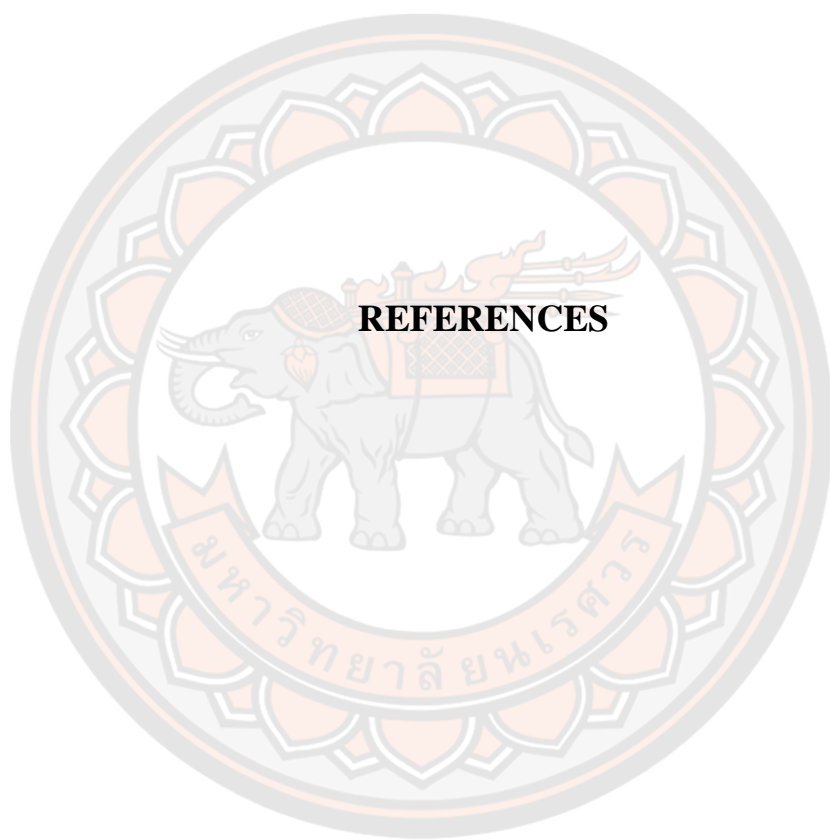
REFERENCES

REFERENCES

1.   Shi T-H, Huang Y-L, Chen C-C, Pi W-C, Hsu Y-L, Lo L-C, et al. Andrographolide and its fluorescent derivative inhibit the main proteases of 2019-nCoV and SARS-CoV through covalent linkage. Biochemical and Biophysical Research Communications. 2020;533(3):467-73.

2.   Huang J-T, Ran R-X, Lv Z-H, Feng L-N, Ran C-Y, Tong Y-Q, et al. Chronological Changes of Viral Shedding in Adult Inpatients With COVID-19 in Wuhan, China. Clin Infect Dis. 2020;71(16):2158-66.

3.   Jin Z, Du X, Xu Y, Deng Y, Liu M, Zhao Y, et al. Structure of Mpro from SARS-CoV-2 and discovery of its inhibitors. Nature. 2020;582(7811):289-93.

4.   Tahir ul Qamar M, Alqahtani SM, Alamri MA, Chen L-L. Structural basis of SARS-CoV-2 3CLpro and anti-COVID-19 drug discovery from medicinal plants. Journal of Pharmaceutical Analysis. 2020;10(4):313-9.

5.   Jutiviboonsuk A. The Role of Andrographis paniculata (Burm.f.) Wall. ex Nees in Drug Interactions. Siriraj Medical Journal. 2016;67(4):9.

6.   Organization WH. WHO Monographs on Selected Medicinal Plants. 2nd ed. Geneva: Switzerland; 2002. 12-24 p.

7.   Madav S, Tripathi HC, Mishra SK. Analgesic, Antipyretic And Antiulcerogenic Effects Of Andrographolide. Indian J Pharmaceut Sci. 1995;57:121-5.

8.   Bao Z, Guan S, Cheng C, Wu S, Wong S, Kemeny D, et al. A novel antiinflammatory role for andrographolide in asthma via inhibition of the nuclear factor-kappaB pathway. Am J Respir Crit Care Med. 2009;179(8):657-65.

9.   Chen HW, Huang CS, Li CC, Lin AH, Huang YJ, Wang TS, et al. Bioavailability of andrographolide and protection against carbon tetrachloride-induced oxidative damage in rats. Toxicology and Applied Pharmacology. 2014;280(1):1-9.

10.   Yu BC, Hung CR, Chen WC, Cheng JT. Antihyperglycemic effect of andrographolide in streptozotocin-induced diabetic rats. Planta Med. 2003;69(12):1075-9.

11.   Mishra K, Dash AP, Dey N. Andrographolide: A Novel Antimalarial Diterpene Lactone Compound from Andrographis paniculata and Its Interaction with Curcumin and Artesunate. Journal of tropical medicine. 2011;2011:579518.

12.   Banerjee M, Chattopadhyay S, Choudhuri T, Bera R, Kumar S, Chakraborty B, et al. Cytotoxicity and cell cycle arrest induced by andrographolide lead to programmed cell death of MDA-MB-231 breast cancer cell line. Journal of biomedical science. 2016;23:40.

13.   Akbarsha MA, Murugaian P. Aspects of the male reproductive toxicity/male antifertility property of andrographolide in albino rats: effect on the testis and the cauda epididymidal spermatozoa. Phytotherapy Research. 2000;14(6):432-5.

14.   Woo AY, Waye MM, Tsui SK, Yeung ST, Cheng CH. Andrographolide up-regulates cellular-reduced glutathione level and protects cardiomyocytes against hypoxia/reoxygenation injury. J Pharmacol Exp Ther. 2008;325(1):226-35.

15.   Zhang XF, Tan BK. Antihyperglycaemic and anti-oxidant properties of Andrographis paniculata in normal and diabetic rats. Clinical and Experimental Pharmacology and Physiology. 2000;27(5-6):358–63.

16.   Uttekar MM, Das T, Pawar RS, Bhandari B, Menon V, Nutan, et al. Anti-HIV activity of semisynthetic derivatives of andrographolide and computational study of HIV-1 gp120 protein binding. European journal of medicinal chemistry. 2012;56:368-74.

17.   Calabrese C, Berman SH, Babish JG, Ma X, Shinto L, Dorr M, et al. A phase I trial of andrographolide in HIV positive patients and normal volunteers. Phytother Res. 2000;14(5):333-8.

18.   Sukardiman, Ervina M, Fadhil Pratama MR, Poerwono H, Siswodihardjo S. The coronavirus disease 2019 main protease inhibitor from *Andrographis paniculata* (Burm. f) Ness. J Adv Pharm Technol Res. 2020;11(4):157-62.

19.   Shi TH, Huang YL, Chen CC, Pi WC, Hsu YL, Lo LC, et al. Andrographolide and its fluorescent derivative inhibit the main proteases of 2019-nCoV and SARS-CoV through covalent linkage. Biochem Biophys Res Commun. 2020;533(3):467-73.

20.   Sa-ngiamsuntorn K, Suksatu A, Pewkliang Y, Thongsri P, Kanjanasirirat P, Manopwisedjaroen S, et al. Anti-SARS-CoV-2 Activity of Andrographis paniculata Extract and Its Major Component Andrographolide in Human Lung Epithelial Cells

and Cytotoxicity Evaluation in Major Organ Cell Representatives. Journal of natural products. 2021.

21.   Rubin D, Chan-Tack K, Farley J, Sherwat A. FDA Approval of Remdesivir — A Step in the Right Direction. New England Journal of Medicine. 2020;383(27):2598-600.

22.   Royal Thai Government Gazette, 138. Sect. 120 (4 June 2021).

23.   Ciampi E, Uribe-San-Martin R, Carcamo C, Cruz JP, Reyes A, Reyes D, et al. Efficacy of andrographolide in not active progressive multiple sclerosis: a prospective exploratory double-blind, parallel-group, randomized, placebo-controlled trial. BMC Neurol. 2020;20(1):173.

24.   Liu X, Yu S, Guo S-W. A pilot study on the use of andrographolide to treat symptomatic adenomyosis. Gynecology and Minimally Invasive Therapy. 2014;3(4):119-26.

25.   Ye L, Wang T, Tang L, Liu W, Yang Z, Zhou J, et al. Poor oral bioavailability of a promising anticancer agent andrographolide is due to extensive metabolism and efflux by P-glycoprotein. Journal of pharmaceutical sciences. 2011;100(11):5007-17.

26.   Yang T, Sheng HH, Feng NP, Wei H, Wang ZT, Wang CH. Preparation of andrographolide-loaded solid lipid nanoparticles and their in vitro and in vivo evaluations: characteristics, release, absorption, transports, pharmacokinetics, and antihyperlipidemic activity. Journal of pharmaceutical sciences. 2013;102(12):4414-25.

27.   Artursson P, J. K. Correlation between oral drug absorption in humans and apparent drug permeability coefficients in human intestinal epithelial (Caco-2) cells. Biochemical and Biophysical Research Communications. 1991;175(3):880-5.

28.   Shekhawat PB, Pokharkar VB. Understanding peroral absorption: regulatory aspects and contemporary approaches to tackling solubility and permeability hurdles. Acta Pharmaceutica Sinica B. 2017;7(3):260-80.

29.   Qiao H, Chen L, Rui T, Wang J, Chen T, Fu T, et al. Fabrication and in vitro/in vivo evaluation of amorphous andrographolide nanosuspensions stabilized by d-alpha-tocopheryl polyethylene glycol 1000 succinate/sodium lauryl sulfate. International journal of nanomedicine. 2017;12:1033-46.

30.   Daodee S, Wangboonskul J, Jarukamjorn K, Sripanidkulchai BO, T. M. Membrane Transport of Andrographolide in Artificial Membrane and Rat Small Intestine. Pakistan Journal of Biological Sciences. 2007;10(12):2078-85.

31.   Pholphana N, Panomvana D, Rangkadilok N, Suriyo T, Puranajoti P, Ungtrakul T, et al. Andrographis paniculata: Dissolution investigation and pharmacokinetic studies of four major active diterpenoids after multiple oral dose administration in healthy Thai volunteers. Journal of Ethnopharmacology. 2016;194:513-21.

32.   Meili Chen, Chunying Xie, Liu L. Solubility of Andrographolide in Various Solvents from (288.2 to 323.2) K. Journal of Chemical & Engineering Data. 2010;55:5297–8.

33.   Banerjee M, Chattopadhyay S, Choudhuri T, Bera R, Kumar S, Chakraborty B, et al. Cytotoxicity and cell cycle arrest induced by andrographolide lead to programmed cell death of MDA-MB-231 breast cancer cell line. J Biomed Sci. 2016;23(1).

34.   Tu YS, Sun DM, Zhang JJ, Jiang ZQ, Chen YX, Zeng XH, et al. Preparation and characterisation of andrographolide niosomes and its anti-hepatocellular carcinoma activity. Journal of microencapsulation. 2014;31(4):307-16.

35.   Bera R, Ahmed SK, Sarkar L, Sen T, Karmakar S. Pharmacokinetic analysis and tissue distribution of andrographolide in rat by a validated LC-MS/MS method. Pharmaceutical Biology. 2014;52(3):321-9.

36.   Panossian A, Hovhannisyan A, Mamikonyan G, Abrahamian H, Hambardzumyan E, Gabrielian E, et al. Pharmacokinetic and oral bioavailability of andrographolide from Andrographis paniculata fixed combination Kan Jang in rats and human. Phytomedicine. 2000;7(5):351-64.

37.   Tian X, Liang S, Wang C, Wu B, Ge G, Deng S, et al. Regioselective glucuronidation of andrographolide and its major derivatives: metabolite identification, isozyme contribution, and species differences. AAPS Journal. 2015;17(1):156-66.

38.   Wangboonskul J, Daodee S, Jarukamjorn K, Sripanidkulchai B. Pharmacokinetic Study of Andrographis paniculata Tablets in Healthy Thai Male Volunteers. Thai Pharmaceutical and Health Science Journal. 2006;1(3):209-18.

39.   Nair A, Morsy MA, Jacob S. Dose translation between laboratory animals and human in preclinical and clinical phases of drug development. Drug development research. 2018;79(8):373-82.

40.   Jones HM, Mayawala K, Poulin P. Dose Selection Based on Physiologically Based Pharmacokinetic (PBPK) Approaches. AAPS Journal. 2012;15(2):377-87.

41.   Miller NA, Reddy MB, Heikkinen AT, Lukacova V, Parrott N. Physiologically Based Pharmacokinetic Modelling for First-In-Human Predictions: An Updated Model Building Strategy Illustrated with Challenging Industry Case Studies. Clinical Pharmacokinetics. 2019;58(6):727-46.

42.   Kuepfer L, Niederalt C, Wendl T, Schlender JF, Willmann S, Lippert J, et al. Applied Concepts in PBPK Modeling: How to Build a PBPK/PD Model. CPT: pharmacometrics & systems pharmacology. 2016;5(10):516-31.

43.   Jones H, Rowland-Yeo K. Basic concepts in physiologically based pharmacokinetic modeling in drug discovery and development. CPT: pharmacometrics & systems pharmacology. 2013;2:e63.

44.   Lowe PJ, Hijazi Y, Luttringer O, Yin H, Sarangapani R, Howard D. On the anticipation of the human dose in first-in-man trials from preclinical and prior clinical information in early drug development. Xenobiotica; the fate of foreign compounds in biological systems. 2007;37(10-11):1331-54.

45.   Joselin Solomon Jeeva J. Andrographis paniculata: A Review of its Traditional Uses, Phytochemistry and Pharmacology. Medicinal & Aromatic Plants. 2014;03.

46.   Kānphǣt TKWst. Thai herbal pharmacopoeia. Nonthaburi, Thailand : Dept. of Medical Sciences, Ministry of Public Health, 2018: Thailand; 2018.

47.   Tan WSD, Liao W, Zhou S, Wong WSF. Is there a future for andrographolide to be an anti-inflammatory drug? Deciphering its major mechanisms of action. Biochemical pharmacology. 2017;139:71-81.

48.   Akbar S. Andrographis paniculata: a review of pharmacological activities and clinical effects. Alternative Medicine Review. 2011;16(1):66-77.

49.   Poolsup N, Suthisisang C Fau - Prathanturarug S, Prathanturarug S Fau - Asawamekin A, Asawamekin A Fau - Chanchareon U, Chanchareon U. Andrographis paniculata in the symptomatic treatment of uncomplicated upper respiratory tract

infection: systematic review of randomized controlled trials. Journal of Clinical Pharmacy and Therapeutics. 2004(0269-4727 (Print)).

50.   Coon JT, Ernst E. Andrographis paniculata in the treatment of upper respiratory tract infections: a systematic review of safety and efficacy. Planta medica. 2004(0032-0943 (Print)).

51.   Maiti K, Gantait A, Kakali M, Saha BP, Mukherjee PK. Therapeutic Potentials of Andrographolide from Andrographis paniculata : A Review. Journal of Natural Remedies. 2006:13.

52.   Chen LX, Qu GX, Qiu F. Studies on flavonoids of Andrographis paniculata. China journal of Chinese materia medica. 2006;31(5):391-5.

53.   Chen LX, Qu GX, Qiu F. Studies on diterpenoids from Andrographis paniculata. China journal of Chinese materia medica. 2006;31(19):1594-7.

54.   Okhuarobo A, Falodun JE, Erharuyi O, Imieje V, Falodun A, Langer P. Harnessing the medicinal properties of Andrographis paniculata for diseases and beyond: a review of its phytochemistry and pharmacology. Asian Pac J Trop Dis. 2014;4(3):213-22.

55.   Jarukamjorn K, Nemoto N. Pharmacological Aspects of Andrographis paniculata on Health and Its Major Diterpenoid Constituent Andrographolide. Journal of Health Science. 2008;54:370-81.

56.   Niranjan A, Tewari S, Lehri A. Biological activities of Kalmegh (Andrographis paniculata Nees) and its active principles-A review. Indian Journal of Natural Products and Resources. 2010;1:125-35.

57.   Chao WW, Lin BF. Isolation and identification of bioactive compounds in Andrographis paniculata (Chuanxinlian). Chinese medicine. 2010;5:17.

58.   Lu WJ, Lee JJ, Chou DS, Jayakumar T, Fong TH, Hsiao G, et al. A novel role of andrographolide, an NF-kappa B inhibitor, on inhibition of platelet activation: the pivotal mechanisms of endothelial nitric oxide synthase/cyclic GMP. Journal of Molecular Medicine. 2011;89(12):1261-73.

59.   Jayakumar T, Hsieh C-Y, Lee J-J, Sheu J-R. Experimental and Clinical Pharmacology of Andrographis paniculata and Its Major Bioactive Phytoconstituent Andrographolide. Evidence-based complementary and alternative medicine : eCAM. 2013;2013:846740-.

60.   Jutiviboonsuk A. The Role of Andrographis paniculata (Burm.f.) Wall. ex Nees in Drug Interactions. 2016. 2016;67(4):9.

61.   Ashok K, Amit A, Sujatha M, Murali B, Anand MS. Effect of Aging on Andrographolide Content in Andrographis paniculata. Journal of Natural Medicines. 2002:3.

62.   Balap A, Atre B, Lohidasan S, Sinnathambi A, Mahadik K. Pharmacokinetic and pharmacodynamic herb-drug interaction of Andrographis paniculata (Nees) extract and andrographolide with etoricoxib after oral administration in rats. Journal of Ethnopharmacology. 2016;183:9-17.

63.   Bothiraja C, Shinde MB, Rajalakshmi S, Pawar AP. Evaluation of molecular pharmaceutical and in-vivo properties of spray-dried isolated andrographolide-PVP. Journal of Pharmacy and Pharmacology. 2009;61(11):1465-72.

64.   Megantara S, Mutakin, Levita J. Predcition of log p and spectrum of quercetine, glucosamine, and andrographolide and its correlation with laboratory analysis. International journal of pharmaceutics. 2016;8(11):33-7.

65.   Singh A, Singh VK, Quraishi MA. Aqueous Extract of Kalmegh (Andrographis paniculata) Leaves as Green Inhibitor for Mild Steel in Hydrochloric Acid Solution. International Journal of Corrosion. 2010;2010.

66.   Chen JX, Xue HJ, Ye WC, Fang BH, Liu YH, Yuan SH, et al. Activity of andrographolide and its derivatives against influenza virus in vivo and in vitro. Biological and Pharmaceutical Bulletin. 2009;32(8):1385-91.

67.   Vijayan M, Hahm B. Influenza Viral Manipulation of Sphingolipid Metabolism and Signaling to Modulate Host Defense System. Scientifica. 2014;2014:793815.

68.   German Advisory Committee Blood SAoPTbB. Human Immunodeficiency Virus (HIV). Transfus Med Hemother. 2016;43(3):203-22.

69.   Yahi N, Sabatier j-m, Nickel P, Mabrouk K, Gonzalez-Scarano F, Fantini J. Suramin inhibits binding of the V3 region of HIV-1 envelope glycoprotein gp120 to galactosylceramide, the receptor for HIV-1 gp120 on human colon epithelial cells. Journal of biological chemistry. 1994;269:24349-53.

70.   Sheeja K, Kuttan G. Activation of cytotoxic T lymphocyte responses and attenuation of tumor growth in vivo by Andrographis paniculata extract and andrographolide. Immunopharmacology and immunotoxicology. 2007;29(1):81-93.

71.   Amroyan E, Gabrielian E, Panossian A, Wikman G, Wagner H. Inhibitory effect of andrographolide from Andrographis paniculata on PAF-induced platelet aggregation. Phytomedicine. 1999;6(1):27-31.

72.   Thisoda P, Rangkadilok N, Pholphana N, Worasuttayangkurn L, Ruchirawat S, Satayavivad J. Inhibitory effect of Andrographis paniculata extract and its active diterpenoids on platelet aggregation. European journal of pharmacology. 2006;553(1):39-45.

73.   Yokoyama H, Ito N, Soeda S, Ozaki M, Suzuki Y, Watanabe M, et al. Prediction of antiplatelet effects of aspirin in vivo based on in vitro results. Clinical and Applied Thrombosis/Hemostasis. 2013;19(6):600-7.

74.   Lu WJ, Lin KH, Hsu MJ, Chou DS, Hsiao G, Sheu JR. Suppression of NF-κB signaling by andrographolide with a novel mechanism in human platelets: regulatory roles of the p38 MAPK-hydroxyl radical-ERK2 cascade. Biochemical pharmacology. 2012;84(7):914-24.

75.   Yang T, Shi HX, Wang ZT, Wang CH. Hypolipidemic effects of andrographolide and neoandrographolide in mice and rats. Phytotherapy Research. 2013;27(4):618-23.

76.   Subramanian R, Asmawi MZ, Sadikun A. Effect of Andrographolide and Ethanol Extract of Andrographis paniculata on Liver Glycolytic, Gluconeogenic, and Lipogenic Enzymes in a Type 2 Diabetic Rat Model. Pharmaceutical Biology. 2008;46(10-11):772-80.

77.   Subramanian R, Asmawi Mz Fau - Sadikun A, Sadikun A. In vitro alpha-glucosidase and alpha-amylase enzyme inhibitory effects of Andrographis paniculata extract and andrographolide. Acta Biochimica Polonica. 2008;5(0001-527X (Print)).

78.   Subramanian R, Asmawi MZ. Inhibition of α-Glucosidase by Andrographis paniculata. Ethanol Extract in Rats. Pharmaceutical Biology. 2006;44(8):600-6.

79.   Zhang Z, Jiang J Fau - Yu P, Yu P Fau - Zeng X, Zeng X Fau - Larrick JW, Larrick Jw Fau - Wang Y, Wang Y. Hypoglycemic and beta cell protective effects of andrographolide analogue for diabetes treatment. Journal of Translational Medicine. 2009(1479-5876 (Electronic)).

80.   Yu B-C, Hung C-R, Chen W-C, Cheng J-T. Antihyperglycemic Effect of Andrographolide in Streptozotocin-Induced Diabetic Rats. Planta medica. 2003;69(12):1075-9.

81.   Dandu AM, Inamdar NM. Evaluation of beneficial effects of antioxidant properties of aqueous leaf extract of Andrographis paniculata in STZ-induced diabetes. Pakistan journal of pharmaceutical sciences. 2009;22(1):49-52.

82.   Suh KN, Kain KC, Keystone JS. Malaria. CMAJ. 2004;170(11):1693-702.

83.   Misra P, Pal NL, Guru PY, Katiyar JC, Srivastava V, Tandon JS. Antimalarial Activity of Andrographis paniculata (Kalmegh) against Plasmodium berghei NK 65 in Mastomys natalensis. International Journal of Pharmacology. 1992;30(4):263-74.

84.   Widyawaruyanti A, Asrory M, Ekasari W, Setiawan D, Radjaram A, Tumewu L, et al. In vivo Antimalarial Activity of Andrographis Paniculata Tablets. Procedia Chemistry. 2014;13:101-4.

85.   Dai Y, Chen SR, Chai L, Zhao J, Wang Y, Wang Y. Overview of pharmacological activities of Andrographis paniculata and its major compound andrographolide. Critical reviews in food science and nutrition. 2019;59(sup1):S17-S29.

86.   Sharma JN, Al-Omran A, Parvathy SS. Role of nitric oxide in inflammatory diseases. Inflammopharmacology. 2007;15(6):252-9.

87.   Chiou WF, Chen CF, Lin JJ. Mechanisms of suppression of inducible nitric oxide synthase (iNOS) expression in RAW 264.7 cells by andrographolide. British journal of pharmacology. 2000;129(8):1553-60.

88.   Batkhuu J, Hattori K, Takano F, Fushiya S, Oshiman K, Fujimiya Y. Suppression of NO production in activated macrophages in vitro and ex vivo by neoandrographolide isolated from Andrographis paniculata. Biological and Pharmaceutical Bulletin. 2002;25(9):1169-74.

89.   Mah SH, Teh SS, Ee GC. Anti-inflammatory, anti-cholinergic and cytotoxic effects of Sida rhombifolia. Pharmaceutical Biology. 2017;55(1):920-8.

90.   Abu-Ghefreh AA, Canatan H, Ezeamuzie CI. In vitro and in vivo anti-inflammatory effects of andrographolide. International immunopharmacology. 2009;9(3):313-8.

91.   Bao Z, Guan S, Cheng C, Wu S, Wong SH, Kemeny DM, et al. A novel antiinflammatory role for andrographolide in asthma via inhibition of the nuclear factor-kappaB pathway. American journal of respiratory and critical care medicine. 2009;179(8):657-65.

92.   Gowthami M, Selvi ST, Kumar GS, Panneerselvam A. Phytochemical analysis and antibacterial properties of leaf extract of Azima tetracantha (Lam.). Asian Journal of Plant Science & Research. 2012;2.

93.   Tanwar J, Das S. Multidrug resistance: an emerging crisis. 2014;2014:541340.

94.   Kern WV. Management of Staphylococcus aureus bacteremia and endocarditis: progresses and challenges. Current opinion in infectious diseases. 2010;23(4):346-58.

95.   Banerjee M, Parai D, Chattopadhyay S, Mukherjee SK. Andrographolide: antibacterial activity against common bacteria of human health concern and possible mechanism of action. Folia microbiologica. 2017;62(3):237-44.

96.   Mandal SM, Migliolo L, Silva ON, Fensterseifer IC, Faria-Junior C, Dias SC, et al. Controlling resistant bacteria with a novel class of β-lactamase inhibitor peptides: from rational design to in vivo analyses. Scientific reports. 2014;4:6015.

97.   Suebsasana S, Pongnaratorn P, Sattayasai J, Arkaravichien T, Tiamkao S, Aromdee C. Analgesic, antipyretic, anti-inflammatory and toxic effects of andrographolide derivatives in experimental animals. Archives of pharmacal research. 2009;32(9):1191-200.

98.   Lin FL, Wu SJ, Lee SC, Ng LT. Antioxidant, antioedema and analgesic activities of Andrographis paniculata extracts and their active constituent andrographolide. Phytotherapy Research. 2009;23(7):958-64.

99.   Nanduri S, Nyavanandi VK, Thunuguntla SS, Kasu S, Pallerla MK, Ram PS, et al. Synthesis and structure-activity relationships of andrographolide analogues as novel cytotoxic agents. Bioorganic & medicinal chemistry letters. 2004;14(18):4711-7.

100.   Li J, Cheung H-Y, Zhang Z, Chan GKL, Fong W-F. Andrographolide Induces Cell Cycle Arrest at G2/M Phase and Cell Death in HepG2 Cells via Alteration of Reactive Oxygen Species. European journal of pharmacology. 2007;568:31-44.

101.   Jiang CG, Li JB, Liu FR, Wu T, Yu M, Xu HM. Andrographolide inhibits the adhesion of gastric cancer cells to endothelial cells by blocking E-selectin expression. Anticancer research. 2007;27(4b):2439-47.

102.   Singha PK, Roy S, Dey S. Protective activity of andrographolide and arabinogalactan proteins from Andrographis paniculata Nees. against ethanol-induced toxicity in mice. Journal of Ethnopharmacology. 2007;111(1):13-21.

103.   Shi G, Zhang Z, Zhang R, Zhang X, Lu Y, Yang J, et al. Protective effect of andrographolide against concanavalin A-induced liver injury. Naunyn-Schmiedeberg's archives of pharmacology. 2012;385(1):69-79.

104.   Badimon L, Padró T, Vilahur G. Atherosclerosis, platelets and thrombosis in acute ischaemic heart disease. Eur Heart J Acute Cardiovasc Care. 2012;1(1):60-74.

105.   Nugroho AE, Andrie M, Warditiani NK, Siswanto E, Pramono S, Lukitaningsih E. Antidiabetic and antihiperlipidemic effect of Andrographis paniculata (Burm. f.) Nees and andrographolide in high-fructose-fat-fed rats. Indian Journal of Natural Products and Resources. 2012;44(3):377-81.

106.   Xia YF, Ye BQ, Li YD, Wang JG, He XJ, Lin X, et al. Andrographolide attenuates inflammation by inhibition of NF-kappa B activation through covalent modification of reduced cysteine 62 of p50. Journal of immunology. 2004;173(6):4207-17.

107.   Matsuda T, Kuroyanagi M, Sugiyama S, Umehara K, Ueno A, Nishi K. Cell differentiation-inducing diterpenes from Andrographis paniculata Nees. Chemical and Pharmaceutical Bulletin (Tokyo). 1994;42(6):1216-25.

108.   Lim JC, Chan TK, Ng DS, Sagineedu SR, Stanslas J, Wong WS. Andrographolide and its analogues: versatile bioactive molecules for combating inflammation and cancer. Clinical and Experimental Pharmacology and Physiology. 2012;39(3):300-10.

109.   Bothiraja C, Pawar AP, Shende VS, Joshi PP. Acute and subacute toxicity study of andrographolide bioactive in rodents: Evidence for the medicinal use as an alternative medicine. Comparative Clinical Pathology. 2012;22(6):1123-8.

110. Dawoud H, Shayoub M. Acute Toxicity Studies of Ethanolic Extract of Eucalyptus Camaldulensis Dehnh Leaves. Journal of Network Communications and Emerging Technologies. 2015;2.

111. Calabrese C, Berman SH, Babish JG, Ma X, Shinto L, Dorr M, et al. A phase I trial of andrographolide in HIV positive patients and normal volunteers. Phytotherapy Research. 2000;14(5):333-8.

112. Yen CC, Chen YC, Wu MT, Wang CC, Wu YT. Nanoemulsion as a strategy for improving the oral bioavailability and anti-inflammatory activity of andrographolide. International journal of nanomedicine. 2018;13:669-80.

113. Yen CC, Liang YK, Cheng CP, Hsu MC, Wu YT. Oral bioavailability enhancement and anti-fatigue assessment of the andrographolide loaded solid dispersion. International Journal of Molecular Sciences. 2020;21(7).

114. Zhao Q, Ding J, Jin H, Ding L, Ren N. A green method using a micellar system for determination of andrographolide and dehydroandrographolide in human plasma. Journal of chromatographic science. 2013;51(4):341-8.

115. Ma Y, Yang Y, Xie J, Xu J, Yue P, Yang M. Novel nanocrystal-based solid dispersion with high drug loading, enhanced dissolution, and bioavailability of andrographolide. International journal of nanomedicine. 2018;13:3763-79.

116. Chen Y, Liu Y, Xu J, Xie J, Ma Y, Yue P, et al. Design and evaluation of nanocomposite microparticles to enhance dissolution and oral bioavailability of andrographolide. Powder Technol. 2018;323:219-29.

117. Suo XB, Zhang H, Wang YQ. HPLC determination of andrographolide in rat whole blood: study on the pharmacokinetics of andrographolide incorporated in liposomes and tablets. Biomedical Chromatography. 2007;21(7):730-4.

118. Parveen R, Ahmad FJ, Iqbal Z, Samim M, Ahmad S. Solid lipid nanoparticles of anticancer drug andrographolide: formulation, in vitro and in vivo studies. Drug development and industrial pharmacy. 2014;40(9):1206-12.

119. Chellampillai B, Pawar AP. Improved bioavailability of orally administered andrographolide from pH-sensitive nanoparticles. European journal of drug metabolism and pharmacokinetics. 2011;35(3-4):123-9.

120.   Ren K, Zhang Z, Li Y, Liu J, Zhao D, Zhao Y, et al. Physicochemical characteristics and oral bioavailability of andrographolide complexed with hydroxypropyl-beta-cyclodextrin. Pharmazie. 2009;64(8):515-20.

121.   Savjani KT, Gajjar AK, Savjani JK. Drug solubility: importance and enhancement techniques. ISRN pharmaceutics. 2012;2012:195727.

122.   Thingale AD, Shaikh KS, Channekar PR, Galgatte UC, Chaudhari PD, Bothiraja C. Enhanced hepatoprotective activity of andrographolide complexed with a biomaterial. Drug delivery. 2015;22(1):117-24.

123.   Chanchal G, Pratibha S, Saurabh S, G. M. Stability indicating studies of Andrographis paniculata extract by validate HPTLC protocol. Journal of Pharmacognosy and Phytochemistry. 2016;5(6):337-44.

124.   Mahar Doan KM, Humphreys JE, Webster LO, Wring SA, Shampine LJ, Serabjit-Singh CJ, et al. Passive permeability and P-glycoprotein-mediated efflux differentiate central nervous system (CNS) and non-CNS marketed drugs. Journal of Pharmacology and Experimental Therapeutics. 2002;303(3):1029-37.

125.   Annegers J. Total Body Water in Rats and in Mice. Proceedings of the Society for Experimental Biology and Medicine. 1954;87(2):454-6.

126.   Yang T, Xu C, Wang ZT, Wang CH. Comparative pharmacokinetic studies of andrographolide and its metabolite of 14-deoxy-12-hydroxy-andrographolide in rat by ultra-performance liquid chromatography-mass spectrometry. Biomedical Chromatography. 2013;27(7):931-7.

127.   Shukla B, Visen P, K Patnaik G, Dhawan BN. Choleretic Effect of Andrographolide in Rats and Guinea Pigs 11992. 146-9 p.

128.   Zhao HY, Hu H, Wang YT. Comparative metabolism and stability of andrographolide in liver microsomes from humans, dogs and rats using ultra-performance liquid chromatography coupled with triple-quadrupole and Fourier transform ion cyclotron resonance mass spectrometry. Rapid Communications in Mass Spectrometry. 2013;27(12):1385-92.

129.   He X, Li J, Gao H, Qiu F, Hu K, Cui X, et al. Four new andrographolide metabolites in rats. Tetrahedron. 2003;59(34):6603-7.

130.   He X, Li J, Gao H, Qiu F, Cui X, X. Y. Six New Andrographolide Metabolites in Rats. Chemical and Pharmaceutical Bulletin. 2003;51(5):586—9.

131.   He X, Li J, Gao H, Qiu F, Hu K, Cui X, et al. Identification of a rare sulfonic acid metabolite of andrographolide in rats. Drug Metabolism and Disposition. 2002;31(8).

132.   Cui L, Qiu F, Wang N, X. Y. Four New Andrographolide Metabolites in Human Urine. Chemical and Pharmaceutical Bulletin. 2004;52(6):772-5.

133.   Cui L, Qiu F, Yao X. Isolation and identification of seven glucuronide conjugates of andrographolide in human urine. Drug Metabolism and Disposition. 2005;33(4):555-62.

134.   Cui L, Chan W, Qiu F, Cai Z, X. Y. Identification of Four Urea Adducts of Andrographolide in Humans. Drug Metabolism Letters. 2008;2(4):261-8.

135.   Qiu F, Cui L, Chen L, Sun J, Yao X. Two novel creatinine adducts of andrographolide in human urine. Xenobiotica; the fate of foreign compounds in biological systems. 2012;42(9):911-6.

136.   Li X, Hu J, Wang B, Sheng L, Liu Z, Yang S, et al. Inhibitory effects of herbal constituents on P-glycoprotein in vitro and in vivo: herb-drug interactions mediated via P-gp. Toxicology and Applied Pharmacology. 2014;275(2):163-75.

137.   Jaruchotikamol A, Jarukamjorn K, Sirisangtrakul W, Sakuma T, Kawasaki Y, Nemoto N. Strong synergistic induction of CYP1A1 expression by andrographolide plus typical CYP1A inducers in mouse hepatocytes. Toxicology and Applied Pharmacology. 2007;224(2):156-62.

138.   Pekthong D, Blanchard N, Abadie C, Bonet A, Heyd B, Mantion G, et al. Effects of Andrographis paniculata extract and Andrographolide on hepatic cytochrome P450 mRNA expression and monooxygenase activities after in vivo administration to rats and in vitro in rat and human hepatocyte cultures. Chemico-biological interactions. 2009;179(2-3):247-55.

139.   Ooi JP, Kuroyanagi M, Sulaiman SF, Muhammad TS, Tan ML. Andrographolide and 14-deoxy-11, 12-didehydroandrographolide inhibit cytochrome P450s in HepG2 hepatoma cells. Life sciences. 2011;88(9-10):447-54.

140.   ABIDIN SZ, LIEW WL, ISMAIL S, CHAN KL, MAHMUD R. Inhibitory effects of active constituents and extracts of Andrographis paniculata on UGT1A1, UGT1A4, and UGT2B7 enzyme activities. International Journal of Pharmacy and Pharmaceutical Sciences. 2014;6(6).

141.   Ma HY, Sun DX, Cao YF, Ai CZ, Qu YQ, Hu CM, et al. Herb-drug interaction prediction based on the high specific inhibition of andrographolide derivatives towards UDP-glucuronosyltransferase (UGT) 2B7. Toxicology and Applied Pharmacology. 2014;277(1):86-94.

142.   Uchaipichat V. In vitro inhibitory effects of major bioactive constituents of Andrographis paniculata, Curcuma longa and Silybum marianum on human liver microsomal morphine glucuronidation: A prediction of potential herb-drug interactions arising from andrographolide, curcumin and silybin inhibition in humans. Drug Metabolism Pharmacokinetics. 2018;33(1):67-76.

143.   Abdullah NH, Ismail S. Inhibition of UGT2B7 Enzyme Activity in Human and Rat Liver Microsomes by Herbal Constituents. Molecules (Basel, Switzerland). 2018;23(10).

144.   Chang KT, Lii CK, Tsai CW, Yang AJ, Chen HW. Modulation of the expression of the pi class of glutathione S-transferase by Andrographis paniculata extracts and andrographolide. Food Chemical Toxicology. 2008;46(3):1079-88.

145.   Chien CF, Wu YT, Lee WC, Lin LC, Tsai TH. Herb-drug interaction of Andrographis paniculata extract and andrographolide on the pharmacokinetics of theophylline in rats. Chemico-biological interactions. 2010;184(3):458-65.

146.   Balap A, Lohidasan S, Sinnathambi A, Mahadik K. Pharmacokinetic and Pharmacodynamic Interaction of Andrographolide and Standardized Extract of Andrographis paniculata (Nees) with Nabumetone in Wistar Rats. Phytotherapy Research. 2017(1099-1573 (Electronic)).

147.   Samala S, Veeresham C. Pharmacokinetic and Pharmacodynamic Interaction of Boswellic Acids and Andrographolide with Glyburide in Diabetic Rats: Including Its PK/PD Modeling. Phytotherapy Research. 2016;30(3):496-502.

148.   Zhang X, Zhang X, Wang X, Zhao M. Influence of andrographolide on the pharmacokinetics of warfarin in rats. Pharmaceutical Biology. 2018;56(1):351-6.

149.   Wongnawa M, Soontaro P, Riditid W, Wongpoowarak P, Ruengkittisakul S. The effects of Andrographis paniculata (Burm.f.) Nees on the pharmacokinetics and pharmacodynamics of midazolam in healthy volunteers2012. 533-9 p.

150.   Lipscomb JC, Haddad S, Poet T, Krishnan K. Physiologically-based pharmacokinetic (PBPK) models in toxicity testing and risk assessment. Advances in experimental medicine and biology. 2012;745:76-95.

151.   Krishnan K, Andersen M. Physiologically Based Pharmacokinetic and Toxicokinetic Models. Principles and Methods in Toxicology. 2007:232-91.

152.   Ramsey JC, Andersen ME. A physiologically based description of the inhalation pharmacokinetics of styrene in rats and humans. Toxicology and Applied Pharmacology. 1984;73(1):159-75.

153.   Brightman FA, Leahy DE, Searle GE, Thomas S. Application of a generic physiologically based pharmacokinetic model to the estimation of xenobiotic levels in rat plasma. Drug Metabolism and Disposition. 2006;34(1):84-93.

154.   Pilari S, Huisinga W. Lumping of physiologically-based pharmacokinetic models and a mechanistic derivation of classical compartmental models. Journal of pharmacokinetics and pharmacodynamics. 2010;37(4):365-405.

155.   Kagan L, Gershkovich P, Wasan KM, Mager DE. Physiologically based pharmacokinetic model of amphotericin B disposition in rats following administration of deoxycholate formulation (Fungizone(R)): pooled analysis of published data. AAPS Journal. 2011;13(2):255-64.

156.   Brown RP, Delp MD, Lindstedt SL, Rhomberg LR, Beliles RP. Physiological parameter values for physiologically based pharmacokinetic models. Toxicology and industrial health. 1997;13(4):407-84.

157.   Lyons MA, Reisfeld B, Yang RS, Lenaerts AJ. A physiologically based pharmacokinetic model of rifampin in mice. Antimicrobial agents and chemotherapy. 2013;57(4):1763-71.

158.   Bi Y, Deng J, Murry DJ, An G. A Whole-Body Physiologically Based Pharmacokinetic Model of Gefitinib in Mice and Scale-Up to Humans. AAPS Journal. 2016;18(1):228-38.

159.   Poulin P, Theil FP. Prediction of pharmacokinetics prior to in vivo studies. 1. Mechanism-based prediction of volume of distribution. Journal of pharmaceutical sciences. 2001;91(1):129-56.

160.   Poulin P, Theil FP. Prediction of pharmacokinetics prior to in vivo studies. II. Generic physiologically based pharmacokinetic models of drug disposition. Journal of pharmaceutical sciences. 2002;91(5):1358-70.

161.   Peters SA. Physiologically-based pharmacokinetic (PBPK) modeling and simulations : principles, methods, and applications in the pharmaceutical industry. Canada: John Wiley & Sons, Inc., Hoboken, New Jersey; 2012.

162.   B M, Clewell H, Lavé T, E M. Physiologically Based Pharmacokinetic Modeling: A Tool for Understanding ADMET Properties and Extrapolating to Human. 2013.

163.   Espié P, Tytgat D, Sargentini-Maier M-L, Poggesi I, Watelet J-B. Physiologically based pharmacokinetics (PBPK). Drug Metab Rev. 2009;41(3):391-407.

164.   Krishnan K, Loizou G, Spendiff M, Lipscomb J, Andersen M. PBPK modeling: A primer. Quantitative Modeling in Toxicology. 2010:19-58.

165.   Poulin P, Theil FP. A priori prediction of tissue:plasma partition coefficients of drugs to facilitate the use of physiologically-based pharmacokinetic models in drug discovery. Journal of pharmaceutical sciences. 2000;89(1):16-35.

166.   Huang XH, Li J. Pharmacokinetic-Pharmacodynamic Modeling and Simulation. Am J Pharm Educ. 2007;71(1):18.

167.   WHO. Characterization and application of physiologically based phamacokinetic models in risk assessment. Geneva: World Health Organization; 2010.

168.   Li M, Gehring R, Riviere JE, Lin Z. Development and application of a population physiologically based pharmacokinetic model for penicillin G in swine and cattle for food safety assessment. Food and Chemical Toxicology. 2017;107(Pt A):74-87.

169.   Abduljalil K, Cain T, Humphries H, Rostami-Hodjegan A. Deciding on success criteria for predictability of pharmacokinetic parameters from in vitro studies: an analysis based on in vivo observations. Drug Metabolism and Disposition. 2014;42(9):1478-84.

170.   Covington TR, Gearhart JM. Sensitivity and Monte Carlo analysis techniques and their use in uncertainty, variability, and population analysis. In: Fisher JW, Gearhart JM, Lin Z, editors. Physiologically Based Pharmacokinetic (PBPK) Modeling. Cambridge: Academic Press; 2020. p. 211-42.

171.   Thomas RS, Yang RS, Morgan DG, Moorman MP, Kermani HR, Sloane RA, et al. PBPK modeling/Monte Carlo simulation of methylene chloride kinetic changes in mice in relation to age and acute, subchronic, and chronic inhalation exposure. Environ Health Perspect. 1996;104(8):858-65.

172.   Clewell HJ, Gearhart JM, Gentry PR, Covington TR, VanLandingham CB, Crump KS, et al. Evaluation of the uncertainty in an oral reference dose for methylmercury due to interindividual variability in pharmacokinetics. Risk Analysis. 1999;19(4):547-58.

173.   Jiang Y, Wang F, Xu H, Liu H, Meng Q, Liu W. Development of andrographolide loaded PLGA microspheres: optimization, characterization and in vitro-in vivo correlation. International journal of pharmaceutics. 2014;475(1-2):475-84.

174.   Zhang J, Li Y, Gao W, Repka MA, Wang Y, Chen M. Andrographolide-loaded PLGA-PEG-PLGA micelles to improve its bioavailability and anticancer efficacy. Expert Opin Drug Deliv. 2014;11(9):1367-80.

175.   Maiti K, Mukherjee K, Murugan V, Saha BP, Mukherjee PK. Enhancing bioavailability and hepatoprotective activity of andrographolide from Andrographis paniculata, a well-known medicinal food, through its herbosome. Journal of the science of food and agriculture. 2010;90(1):43-51.

176.   Song B, Wang J, Lu SJ, Shan LN. Andrographolide solid dispersions formulated by Soluplus to enhance interface wetting, dissolution, and absorption. J Appl Polym Sci. 2019.

177.   Xu J, Ma Y, Xie Y, Chen Y, Liu Y, Yue P, et al. Design and Evaluation of Novel Solid Self-Nanodispersion Delivery System for Andrographolide. AAPS PharmSciTech. 2017;18(5):1572-84.

178.   Du H, Yang X, Li H, Han L, Li X, Dong X, et al. Preparation and evaluation of andrographolide-loaded microemulsion. Journal of microencapsulation. 2012;29(7):657-65.

179.   Syukri Y, Martien R, Lukitaningsih E, Nugroho AE. Novel Self-Nano Emulsifying Drug Delivery System (SNEDDS) of andrographolide isolated from Andrographis paniculata Nees: Characterization, in-vitro and in-vivo assessment. J Drug Deliv Sci Technol. 2018;47:514-20.

180.   Xu L, Xiao DW, Lou S, Zou JJ, Zhu YB, Fan HW, et al. A simple and sensitive HPLC-ESI-MS/MS method for the determination of andrographolide in human plasma. Journal of Chromatography B: Analytical Technologies in the Biomedical and Life Sciences. 2009;877(5-6):502-6.

181.   Gu Y, Ma J, Liu Y, Chen B, Yao S. Determination of andrographolide in human plasma by high-performance liquid chromatography/mass spectrometry. Journal of Chromatography B: Analytical Technologies in the Biomedical and Life Sciences. 2007;854(1-2):328-31.

182.   Bormann I. Digitizelt (version 2.3.3) 2012. Available from: http://www.digitizeit.de/.

183.   Jiang Y, Wang F, Xu H, Liu H, Meng Q, Liu W. Development of andrographolide loaded PLGA microspheres: optimization, characterization and in vitro-in vivo correlation. Int J Pharmacol. 2014;475(1-2):475-84.

184.   Yen CC, Chen YC, Wu MT, Wang CC, Wu YT. Nanoemulsion as a strategy for improving the oral bioavailability and anti-inflammatory activity of andrographolide. Int J Nanomedicine. 2018;13:669-80.

185.   Ren K, Zhang Z Fau - Li Y, Li Y Fau - Liu J, Liu J Fau - Zhao D, Zhao D Fau - Zhao Y, Zhao Y Fau - Gong T, et al. Physicochemical characteristics and oral bioavailability of andrographolide complexed with hydroxypropyl-beta-cyclodextrin. Die Pharmazie. 2009;64(8):515-20.

186.   Song B, Wang J, Lu SJ, Shan LN. Andrographolide solid dispersions formulated by Soluplus to enhance interface wetting, dissolution, and absorption. Journal of Applied Polymer Science. 2019;137:48354.

187.   Zhang Y, Hu X, Liu X, Dandan Y, Di D, Yin T, et al. Dry state microcrystals stabilized by an HPMC film to improve the bioavailability of andrographolide. International journal of pharmaceutics. 2015;493(1-2):214-23.

188.   Brown RP, Delp MD, Lindstedt SL, Rhomberg LR, Beliles RP. Physiological parameter values for physiologically based pharmacokinetic models. Toxicol Ind Health. 1997;13(4):407-84.

189.   McNally K, Cotton R, Loizou GD. A Workflow for Global Sensitivity Analysis of PBPK Models. Frontiers in pharmacology. 2011;2:31.

190.   Tian X, Liang S, Wang C, Wu B, Ge G, Deng S, et al. Regioselective glucuronidation of andrographolide and its major derivatives: metabolite identification, isozyme contribution, and species differences. AAPS J. 2015;17(1):156-66.

191.   Campbell J, Van Landingham C, Crowell S, Gentry R, Kaden D, Fiebelkorn S, et al. A preliminary regional PBPK model of lung metabolism for improving species dependent descriptions of 1,3-butadiene and its metabolites. Chemico-biological interactions. 2015;238:102-10.

192.   Zhang H, Gao N, Tian X, Liu T, Fang Y, Zhou J, et al. Content and activity of human liver microsomal protein and prediction of individual hepatic clearance in vivo. Sci Rep. 2015;5(1):17671.

193.   Sloczynska K, Gunia-Krzyzak A, Koczurkiewicz P, Wojcik-Pszczola K, Zelaszczyk D, Popiol J, et al. Metabolic stability and its role in the discovery of new chemical entities. Acta Pharm. 2019;69(3):345-61.

194.   Abduljalil K, Cain T, Humphries H, Rostami-Hodjegan A. Deciding on success criteria for predictability of pharmacokinetic parameters from *In vitro* studies: An analysis based on *in vivo* observations. Drug Metab Dispos. 2014;42(9):1478-84.

195.   Fàbrega F, Nadal M, Schuhmacher M, Domingo JL, Kumar V. Influence of the uncertainty in the validation of PBPK models: A case-study for PFOS and PFOA. Regul Toxicol Pharmacol. 2016;77:230-9.

196.   Chiu WA, Barton HA, DeWoskin RS, Schlosser P, Thompson CM, Sonawane B, et al. Evaluation of physiologically based pharmacokinetic models for use in risk assessment. J Appl Toxicol. 2007;27(3):218-37.

197.   Peters SA. Variability, uncertainty, and sensitivity analysis. Physiologically-Based Pharmacokinetic (PBPK) Modeling and Simulations: Principles, Methods, and Applications in the Pharmaceutical Industry. New Jersey: John Wiley & Sons, inc.; 2012. p. 161-81.

198.   Bi Y, Deng J, Murry DJ, An G. A Whole-Body Physiologically Based Pharmacokinetic Model of Gefitinib in Mice and Scale-Up to Humans. AAPS J. 2016;18(1):228-38.

199.   Clewell HJ, 3rd, Lee TS, Carpenter RL. Sensitivity of physiologically based pharmacokinetic models to variation in model parameters: methylene chloride. Risk Anal. 1994;14(4):521-31.

200.   SimulationsPlus. Better Decisions through Better Science. User Manual for GastroPlus Version 9.8. Simulations Plus: Lancaster, CA, USA2020.

201.   Gao H, Su Y, wang W, Xiong W, Sun X, Ji Y, et al. Integrated computer-aided formulation design: A case study of andrographolide/ cyclodextrin ternary formulation. Asian Journal of Pharmaceutical Sciences. 2021.

202.   Heuberger J, Schmidt S, Derendorf H. When is protein binding important? Journal of pharmaceutical sciences. 2013;102(9):3458-67.

203.   Suriyo T, Pholphana N, Ungtrakul T, Rangkadilok N, Panomvana D, Thiantanawat A, et al. Clinical Parameters following Multiple Oral Dose Administration of a Standardized Andrographis paniculata Capsule in Healthy Thai Subjects. Planta medica. 2017;83(9):778-89.

204.   Sa-Ngiamsuntorn K, Suksatu A, Pewkliang Y, Thongsri P, Kanjanasirirat P, Manopwisedjaroen S, et al. Anti-SARS-CoV-2 activity of *Andrographis paniculata* extract and its major component andrographolide in human lung epithelial cells and cytotoxicity evaluation in major organ cell representatives. J Nat Prod. 2021;84(4):1261-70.

205.   Taubenberger JK, Morens DM. The pathology of influenza virus infections. Annu Rev Pathol. 2008;3:499-522.

206.   Xia YF, Ye BQ, Li YD, Wang JG, He XJ, Lin X, et al. Andrographolide Attenuates Inflammation by Inhibition of NF- B Activation through Covalent Modification of Reduced Cysteine 62 of p50. Journal of immunology. 2004;173(6):4207-17.

207.   Price PS, Conolly RB, Chaisson CF, Gross EA, Young JS, Mathis ET, et al. Modeling interindividual variation in physiological factors used in PBPK models of humans. Crit Rev Toxicol. 2003;33(5):469-503.

208.   Zhang J, Li Y, Gao W, Repka MA, Wang Y, M. C. Andrographolide-loaded PLGA-PEG-PLGA micelles to improve its bioavailability and anticancer efficacy. Expert opinion on drug delivery. 2014;11(9):1367-80.

209. Xu FF, Fu SJ, Gu SP, Wang ZM, Wang ZZ, He X, et al. Simultaneous determination of andrographolide, dehydroandrographolide and neoandrographolide in dog plasma by LC-MS/MS and its application to a dog pharmacokinetic study of Andrographis paniculata tablet. Journal of Chromatography B: Analytical Technologies in the Biomedical and Life Sciences. 2015;990:125-31.

210. Banerjee M, Parai D, Chattopadhyay S, Mukherjee SK. Andrographolide: antibacterial activity against common bacteria of human health concern and possible mechanism of action. Folia Microbiol. 2017;62(3):237-44.

211. Pholphana N, Panomvana D, Rangkadilok N, Suriyo T, Ungtrakul T, Pongpun W, et al. A Simple and Sensitive LC-MS/MS Method for Determination of Four Major Active Diterpenoids from Andrographis paniculata in Human Plasma and Its Application to a Pilot Study. Planta medica. 2016;82(1-2):113-20.

212. Taft DR. Chapter 9 - Drug Excretion. In: Hacker M, Messer W, Bachmann K, editors. Pharmacology. San Diego: Academic Press; 2009. p. 175-99.

213. Wangboonskul J, Daodee S, Jarukamjorn K, Sripanidkulchai B. Pharmacokinetic study of *Andrographis paniculata* tablets in healthy Thai male volunteers. Thai Pharm Health Sci J. 2016;1(3):209-18.

214. Gibson PG, Qin L, Puah SH. COVID-19 acute respiratory distress syndrome (ARDS): Clinical features and differences from typical pre-COVID-19 ARDS. Med J Aust. 2020;213(2):54-6.e1.

215. Pekthong D, Martin H, Abadie C, Bonet A, Heyd B, Mantion G, et al. Differential inhibition of rat and human hepatic cytochrome P450 by Andrographis paniculata extract and andrographolide. Journal of Ethnopharmacology. 2008;115(3):432-40.

216. Ramasamy S, Kiew LV, Chung LY. Inhibition of human cytochrome P450 enzymes by Bacopa monnieri standardized extract and constituents. Molecules (Basel, Switzerland). 2014;19(2):2588-601.

217. Izgelov D, Domb AJ, Hoffman A. The effect of piperine on oral absorption of cannabidiol following acute vs. chronic administration. European journal of pharmaceutical sciences : official journal of the European Federation for Pharmaceutical Sciences. 2020;148:105313.

APPENDIX
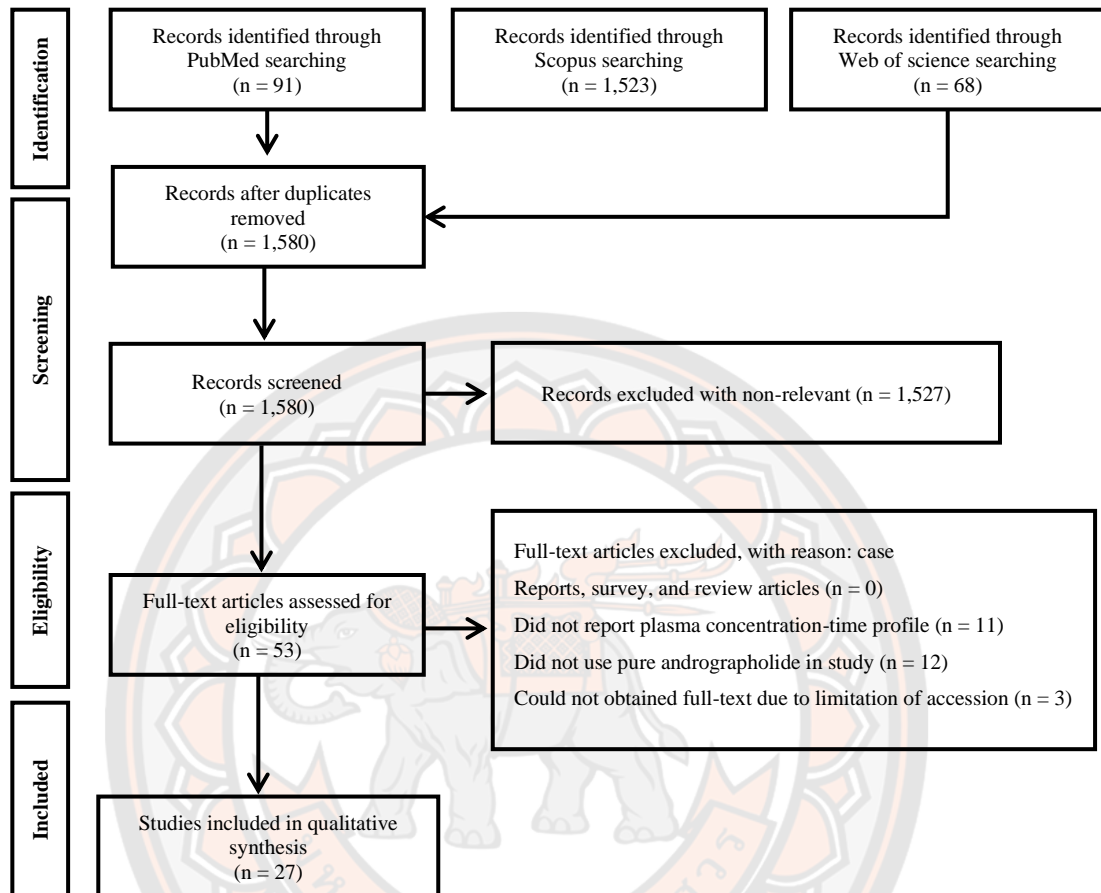
APPENDIX A ELECTRONIC SEARCH FLOW DIAGRAM

Figure 16 Electronic search flow diagram for collection of pharmacokinetic datasets in animals and humans

APPENDIX B SINGLE ORGAN MODEL CONSTRUCTION STAGE

Single organ model Parameterization

The species-specific physiological parameters were mentioned previously. The permeability surface area of tissue (PA_T; cm^3/s) was calculated *via* the following equation:

$$PA_T = P_{app} \times SA \times organ\,weight\,(g) \qquad\qquad Eq.\ 1$$

where P_{app} is apparent permeability (cm/s); SA is the surface area of the organ (cm^2/g) (186). The P_{app} value of mice kidneys cell line was reported as 7 x 10^{-6} cm/s (2). The kidney's surface area was 0.26 cm^2/g (189). The calculated permeability surface area of kidneys was applied to be an initial value for all permeability-limited models. The partition coefficient of tissues to plasma and the fraction unbound in tissues were calculated using Poulin's equations (156).

According to Panossian et al. (36), only 10 % of unchanged Andro was found in rat urine after oral administration of *A. paniculata* extract. Therefore, the renal elimination might be described by the following equation:

$$CL_{total} \times fr \qquad\qquad Eq.\ 2$$

where CL_{total} was the total clearance, and the fraction renal elimination (*fr*) was 0.10. The CL_{total} was computed from PK solver software using the mode of non-compartment analysis based on the dataset from Tu et al. (34). This value was 0.023 L/h.

Model Estimation

In this stage, the disposition parameters including the P_T, f_{uT}, PA_T, $k_{a,T}$, and $k_{d,T}$ values were estimated, whereas the metabolism parameters were fixed.

Mathematical presented in the Single organ model.

The bi-exponential equation (Eq. 3) was used to described Andro plasma concentration-time profile.

$$C_{pl} = A \cdot e^{-\alpha t} + B \cdot e^{-\beta t} \qquad \text{Eq. 3}$$

where C_{pl} is a concentration of Andro in plasma (µmol/L) while A, α, B, and β are constant values obtained from PK solver software using the mode of two-compartment analysis based on the dataset from Tu et al. (34).

Non-elimination organs

Based on a tissue distribution study by Tu et al. (34), the non-elimination organs consisted of lungs, heart, and spleen.

Perfusion-limited model:

The change in the amount of Andro versus time in tissues $\left(\frac{dA_T}{dt}\right)$ after intravenous administration was calculated as followed:

$$\frac{dA_T}{dt} = Q_T * \left(C_{pl} - \frac{C_T}{P_T}\right) \qquad \text{Eq. 4}$$

where A_T is the amount of Andro in the tissues (µmol), Q_T is the blood flow of the tissues (L/h), P_T is the partition coefficient of tissues to plasma.

The concentration of Andro in the tissues (C_T) was calculated as followed:

$$C_T = \frac{C_T}{V_T} \qquad \text{Eq. 5}$$

where V_T is the volume of the tissues (L).

Permeability-limited model:

The change in the amount of Andro versus time in extravascular space of tissues ($\frac{dA_{T,exv}}{dt}$) after intravenous administration was calculated as followed:

$$\frac{dA_{T,vas}}{dt} = Q_T \times \left(C_{pl} - C_{T,vas}\right) - PA_T \times \left(\left(C_{T,vas} \times f_{up}\right) - \left(C_{T,exv} \times f_{uT}\right)\right) \quad \text{Eq. 6}$$

$$\frac{dA_{T,exv}}{dt} = PA_T \times \left(\left(C_{T,vas} \times f_{up}\right) - \left(C_{T,exv} \times f_{uT}\right)\right) \quad \text{Eq. 7}$$

where $C_{T,vas}$ is a concentration of Andro in vascular space of the tissues, $C_{T,exv}$ is a concentration of Andro in extravascular space of the tissues, $A_{T,vas}$ is the amount of Andro in vascular space of the tissues, $A_{T,exv}$ is the amount of Andro in extravascular space of the tissues; f_{uT} is fraction unbound in tissues, $V_{T,vas}$ is a volume of vascular space of the tissues, $V_{T,exv}$ is a volume of extravascular space of the tissues, f_{up} is fraction unbound in plasma, and PA_T is permeability surface area of tissues.

The concentration of Andro in the extravascular space of the tissues ($C_{T,exv}$) was calculated as followed:

$$C_{T,exv} = \frac{A_{T,exv}}{V_{T,exv}} \quad \text{Eq. 8}$$

where $V_{T,exv}$ is a volume of extravascular space of the tissues (L).

Permeability-limited with binding tissue model:

The change in the amount of Andro versus time in extravascular space of the tissues ($\frac{dA_{T,exv}}{dt}$) after intravenous administration was calculated as followed:

$$\frac{dA_{T,vas}}{dt} = Q_T \times \left(C_{pl} - C_{T,vas}\right) - PA_T \times \left(\left(C_{T,vas} \times f_{up}\right) - \left(C_{T,exv} \times f_{uT}\right)\right) \quad \text{Eq. 9}$$

$$\frac{dA_{T,exv}}{dt} = PA_T \times \left(\left(C_{T,vas} \times f_{up}\right) - \left(C_{T,exv} \times f_{uT}\right)\right) - \left(K_{a,T} \times \left(C_{T,exv} \times f_{uT}\right) \times V_{T,exv}\right) - \left(K_{d,T} \times A_{T,D}\right) \quad \text{Eq. 10}$$

$$\frac{dA_{T,D}}{dt} = \left(K_{a,T} \times \left(C_{T,exv} \times f_{uT}\right) \times V_{T,exv}\right) - \left(K_{d,T} \times A_{T,D}\right) \quad \text{Eq. 11}$$

where $A_{T,D}$ is the amount of Andro in the deep in tissue; $V_{T,exv}$ was the volume of tissue extravascular space; $k_{a,T}$ is the association rate constant; $k_{d,T}$ is the dissociation rate constant. The concentration of Andro in the extravascular space of the tissues was described in Eq. 8.

Liver organ

Perfusion-limited model:

The change in amount of Andro versus time in liver ($\frac{dA_{Li}}{dt}$) after intravenous administration was calculated as followed:

$$\frac{dA_{Li}}{dt} = Q_{Li} * \left(C_{pl} - \frac{C_{Li}}{P_{Li}}\right) - \left(\frac{V_{max} \times \left(\frac{C_{Li}}{P_{Li}} \times f_{up}\right)}{K_m + \left(\frac{C_{Li}}{P_{Li}} \times f_{up}\right)}\right) \quad \text{Eq. 12}$$

where A_{Li} is the amount of Andro in the liver (µmol), Q_{Li} is the blood flow of the liver (L/h), P_{Li} is the partition coefficient liver to plasma, V_{max} is the maximum velocity of Andro, and K_m is the binding affinity of Andro which obtained from Tian et al. (Tian, 2015 #192).

The concentration of Andro in the liver (C_{Li}) was calculated as followed:

$$C_{Li} = \frac{C_{Li}}{V_{Li}}$$
Eq. 13

where V_{Li} is the volume of the liver (L).

Permeability-limited model:

The change in the amount of Andro versus time in extravascular space of liver ($\frac{dA_{Li,exv}}{dt}$) after intravenous administration was calculated as followed:

$$\frac{dA_{Li,vas}}{dt} = Q_{Li} \times (C_{pl} - C_{Li,vas}) - PA_{Li} \times ((C_{Li,vas} \times f_{up}) - (C_{Li,exv} \times f_{uLi})) -$$
$$\left(\frac{V_{max} \times (C_{Li,exv} \times f_{uLi})}{K_m + (C_{Li,exv} \times f_{uLi})}\right)$$
Eq. 14

$$\frac{dA_{Li,exv}}{dt} = PA_{Li} \times ((C_{Li,vas} \times f_{up}) - (C_{Li,exv} \times f_{uLi}))$$
Eq. 15

where $C_{Li,vas}$ is a concentration of Andro in vascular space of the liver, $C_{Li,exv}$ is a concentration of Andro in extravascular space of the liver, $A_{Li,vas}$ is the amount of Andro in vascular space of the liver, $A_{Li,exv}$ is the amount of Andro in extravascular space of the liver; f_{uLi} is fraction unbound in the liver, $V_{Li,vas}$ is a volume of vascular space of the liver, $V_{Li,exv}$ is a volume of extravascular space of the liver, f_{up} is fraction unbound in plasma, and PA_{Li} is permeability surface area of the liver.

The concentration of Andro in the extravascular space of the liver ($C_{Li,exv}$) was calculated as followed:

$$C_{Li,exv} = \frac{A_{Li,exv}}{V_{Li,exv}}$$
Eq. 16

where $V_{Li,exv}$ is a volume of extravascular space of the liver (L).

Permeability-limited with binding tissue model:

The change in the amount of Andro versus time in the extravascular space of the liver ($\frac{dA_{Li,exv}}{dt}$) after intravenous administration was calculated as followed:

$$\frac{dA_{Li,vas}}{dt} = Q_{Li} \times \left(C_{pl} - C_{Li,vas}\right) - PA_{Li} \times \left(\left(C_{Li,vas} \times f_{up}\right) - \left(C_{Li,exv} \times f_{uLi}\right)\right) \quad \text{Eq. 17}$$

$$\frac{dA_{Li,exv}}{dt} = PA_{Li} \times \left(\left(C_{Li,vas} \times f_{up}\right) - \left(C_{Li,exv} \times f_{uLi}\right)\right) - \left(K_{a,Li} \times \left(C_{Li,exv} \times f_{uLi}\right) \times \right.$$
$$\left. V_{Li,exv}\right) - \left(K_{d,Li} \times A_{Li,D}\right) - \left(\frac{V_{max} \times \left(C_{Li,exv} \times f_{uLi}\right)}{K_m + \left(C_{Li,exv} \times f_{uLi}\right)}\right) \qquad \text{Eq. 18}$$

$$\frac{dA_{Li,D}}{dt} = \left(K_{a,Li} \times \left(C_{Li,exv} \times f_{uLi}\right) \times V_{Li,exv}\right) - \left(K_{d,Li} \times A_{Li,D}\right) \qquad \text{Eq. 19}$$

where $A_{Li, D}$ is the amount of Andro in the deep in the liver; $V_{Li, exv}$ was the volume of liver extravascular space; $k_{a, Li}$ is the association rate constant; $k_{d, Li}$ is the dissociation rate constant. The concentration of Andro in the extravascular space of the liver was described in Eq. 16.

Kidneys organ

Perfusion-limited model:

The change in the amount of Andro versus time in kidneys ($\frac{dA_{Kd}}{dt}$) after intravenous administration was calculated as followed:

$$\frac{dA_{Kd}}{dt} = Q_{Kd} * \left(C_{pl} - \frac{C_{Kd}}{P_{Kd}}\right) - \left(\left(CL_{total} \times fr\right) \times \frac{C_{Kd}}{P_{Kd}} \times f_{up}\right) \qquad \text{Eq. 20}$$

where A_{Kd} is the amount of Andro in the kidneys (µmol), Q_{Kd} is the blood flow of the kidneys (L/h), P_{Kd} is the partition coefficient of kidneys to plasma, CL_{total} is the total clearance, and fr is the fraction renal elimination.

The concentration of Andro in the kidneys (C_{Kd}) was calculated as followed:

$$C_{Kd} = \frac{C_{Kd}}{V_{Kd}}$$ Eq. 21

where V_{Kd} is the volume of the kidneys (L).

Permeability-limited model:

The change in the amount of Andro versus time in extravascular space of kidneys ($\frac{dA_{Kd,exv}}{dt}$) after intravenous administration was calculated as followed:

$$\frac{dA_{Kd,vas}}{dt} = Q_{Kd} \times (C_{pl} - C_{Kd,vas}) - PA_{Kd} \times \left((C_{Kd,vas} \times f_{up}) - (C_{Kd,exv} \times f_{uKd})\right) - \left((CL_{total} \times fr) \times (C_{Kd,exv} \times f_{uKd})\right)$$ Eq. 22

$$\frac{dA_{Kd,exv}}{dt} = PA_{Kd} \times \left((C_{Kd,vas} \times f_{up}) - (C_{Kd,exv} \times f_{uLi})\right)$$ Eq. 23

where $C_{Kd,vas}$ is a concentration of Andro in vascular space of the kidneys, $C_{Kd,exv}$ is a concentration of Andro in extravascular space of the kidneys, $A_{Kd,vas}$ is the amount of Andro in vascular space of the kidneys, $A_{Kd,exv}$ is the amount of Andro in extravascular space of the kidneys; f_{uKd} is fraction unbound in kidneys, $V_{Kd,vas}$ is a volume of vascular space of the kidneys, $V_{Kd,exv}$ is a volume of extravascular space of the kidneys, f_{up} is fraction unbound in plasma, and PA_{Kd} is permeability surface area of kidneys.

The concentration of Andro in the extravascular space of the kidneys ($C_{Kd,exv}$) was calculated as followed:

$$C_{Kd,exv} = \frac{A_{Kd,exv}}{V_{Kd,exv}}$$ Eq. 24

where $V_{Kd,exv}$ is a volume of extravascular space of the kidneys (L).

Permeability-limited with binding tissue model:

The change in the amount of Andro versus time in extravascular space of the kidneys ($\frac{dA_{Kd,exv}}{dt}$) after intravenous administration was calculated as followed:

$$\frac{dA_{Kd,vas}}{dt} = Q_{Kd} \times \left(C_{pl} - C_{Kd,vas}\right) - PA_{Kd} \times \left(\left(C_{Kd,vas} \times f_{up}\right) - \left(C_{Kd,exv} \times f_{uKd}\right)\right)$$

<div align="right">Eq. 25</div>

$$\frac{dA_{Kd,exv}}{dt} = PA_{Kd} \times \left(\left(C_{Kd,vas} \times f_{up}\right) - \left(C_{Kd,exv} \times f_{uKd}\right)\right) - \left(K_{a,Kd} \times \left(C_{Kd,exv} \times \right.\right.$$
$$\left.f_{uKd}\right) \times V_{Kd,exv}\right) - \left(K_{d,Kd} \times A_{Kd,D}\right) - \left(\left(\left(CL_{total} \times fr\right) \times \left(C_{Kd,exv} \times f_{uKd}\right)\right)\right)$$

<div align="right">Eq. 26</div>

$$\frac{dA_{Kd,D}}{dt} = \left(K_{a,Kd} \times \left(C_{Kd,exv} \times f_{uKd}\right) \times V_{Kd,exv}\right) - \left(K_{d,Kd} \times A_{Kd,D}\right) \qquad \text{Eq. 27}$$

where $A_{Kd,\,D}$ is the amount of Andro in the deep in kidneys; $V_{Kd,\,exv}$ was the volume of kidneys extravascular space; $k_{a,\,Kd}$ is the association rate constant; $k_{d,\,Kd}$ is the dissociation rate constant. The concentration of Andro in the extravascular space of the kidneys was described in Eq. 24.
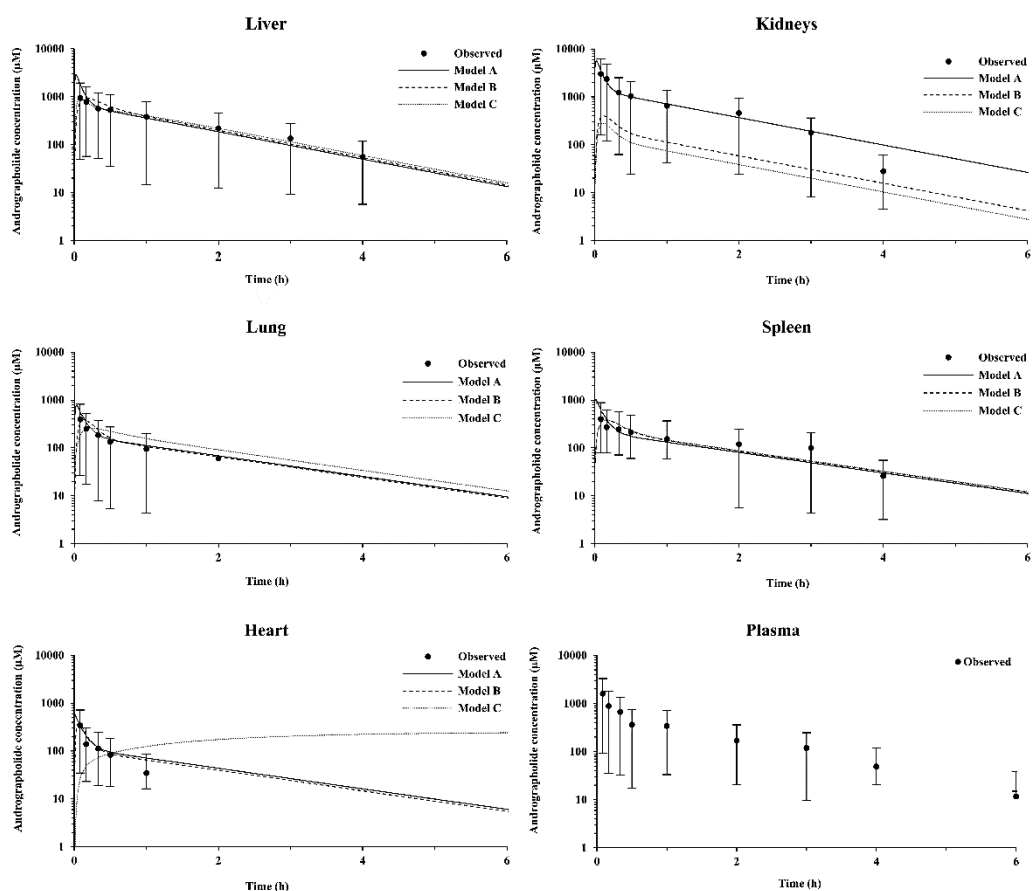
Figure 17 Comparison of single organ model predicted andrographolide levels in liver, kidneys, heart, lung, and spleen over time in mice following intravenous injection at 500 mg/kg. andrographolide levels in plasma are described by a bi-exponential equation. • - observed data, error bar - standard deviation of the observed data. Model A represents perfusion-limited model, Model B represents permeability-limited model, and Model C represents permeability-limited with binding tissues model

Table 20 Estimated disposition parameters used in Single organ model

Assumption	Parameter (unit)	Estimated values (%CV)	AIC values
Liver			
Perfusion-limited	P_{Li}	1.990 (8.65%)	-10.69
Permeability-limited	PA_{Li} (L/h)	0.142 (18.19%)	-13.93
	$f_{u,Li}$	0.046 (16.96%)	
	PA_{Li} (L/h)	0.317 (7.45%)	
	$f_{u,Li}$	0.093 (6.49%)	
Permeability-limited with binding tissues	$k_{a,Li}$ (h^{-1})	166.98 (8.05%)	-37.01
	$k_{d,Li}$ (h^{-1})	4.748 (10.35%)	
Kidneys			
Perfusion-limited	P_{Kd}	0.712 (5.35%)	-4.67
Permeability-limited	PA_{Kd} (L/h)	0.295 (212.0%)	21.37
	$f_{u,Kd}$	0.991 (188.6%)	
	PA_{Kd} (L/h)	0.021 (>1000%)	
	$f_{u,Kd}$	9.052 (303.6%)	
Permeability-limited with binding tissues	$k_{a,Kd}$ (h^{-1})	0.120 (>1000%)	26.14
	$k_{d,Kd}$ (h^{-1})	50.04 (>1000%)	
Lungs			
Perfusion-limited	P_{Lu}	0.036 (5.20%)	-23.65
Permeability-limited	PA_{Lu} (L/h)	0.010 (24.3%)	-20.07
	$f_{u,Lu}$	1.925 (6.20%)	
	PA_{Lu} (L/h)	854.8 (NAN)	
	$f_{u,Lu}$	22.15 (NAN)	
Permeability-limited with binding tissues	$k_{a,Lu}$ (h^{-1})	2459.0 (NAN)	-3.20
	$k_{d,Lu}$ (h^{-1})	169000 (NAN)	
Spleen			
Perfusion-limited	P_{Sl}	0.021 (12.24%)	-16.20
Permeability-limited	PA_{Sl} (L/h)	157.7 (>1000%)	-17.04
	$f_{u,Sl}$	25.87 (9.30%)	
	PA_{Sl} (L/h)	277.0 (NAN)	
Permeability-limited with binding tissues	$f_{u,Sl}$	25.35 (NAN)	-13.18

Assumption	Parameter (unit)	Estimated values (%CV)	AIC values
	$k_{a, Sl}$ (h^{-1})	7669.0 (NAN)	
	$k_{d, Sl}$ (h^{-1})	2975.0 (NAN)	
Heart			
Perfusion-limited	P_{Hr}	0.017 (8.85%)	-16.73
Permeability-limited	PA_{Hr} (L/h)	0.060 (441.3%)	-16.13
	$f_{u, Hr}$	40.96 (16.6%)	
Permeability-limited with binding tissues	PA_{Hr} (L/h)	0.001 (NAN)	7.29
	$f_{u, Hr}$	0.0003 (NAN)	
	$k_{a, Hr}$ (h^{-1})	0.0005 (NAN)	
	$k_{d, Hr}$ (h^{-1})	0.834 (NAN)	

NAN is Not a number; P is partition coefficient tissue/plasma; PA is permeability surface area; f_u is the fraction unbound in tissues; k_a and k_d are a rate of constant.
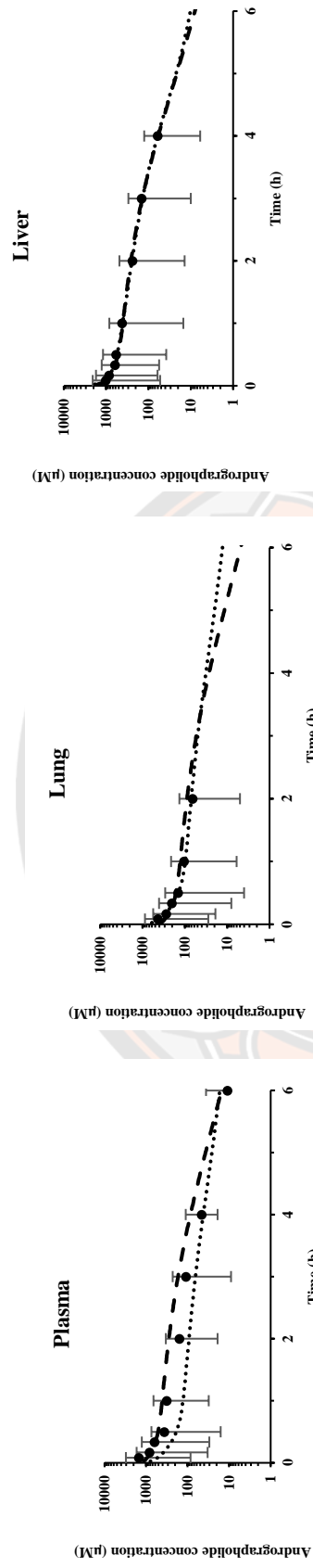
APPENDIX C PBPK MODEL DEVELOPMENT STAGE

Figure 18 Comparison of PBPK model predicted andrographolide levels in plasma, lung, and liver over time in mice following intravenous injection at 500 mg/kg. Closed cycle with error bar (standard deviation) is plasma, lung, and liver concentration levels of andrographolide in mice acquired from Tu et al. (34). Dashed lines and dotted lines represent andrographolide concentration levels in various organs which predicted using the PBPK model that is modified the liver structure as a permeability-limited model, and permeability-limited with binding tissue, respectively

Figure 19 Predicted concentration-time profile in rat plasma following single oral administration at 10 mg/kg. • - observed data acquired from (a) Xu et al., 2016, (b) Chellampillai et al., 2011, and (c) Parveen et al., 2014, solid line- predicted data, error bar - standard deviation of the observed data

Figure 20 Predicted concentration-time profile in rat plasma following single oral administration at 20 mg/kg. • - observed data acquired from (a) Ma et al., 2018, and (b) Chen et al., 2018, solid line- predicted data, error bar - standard deviation of the observed data
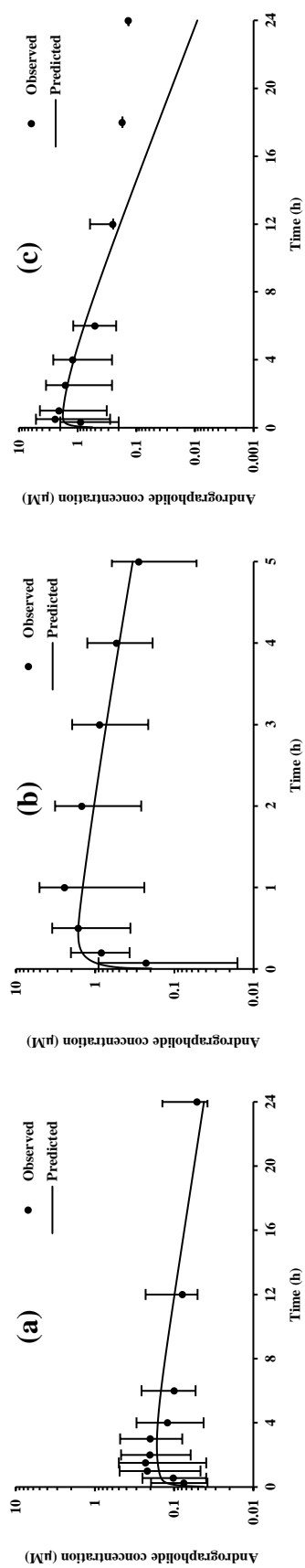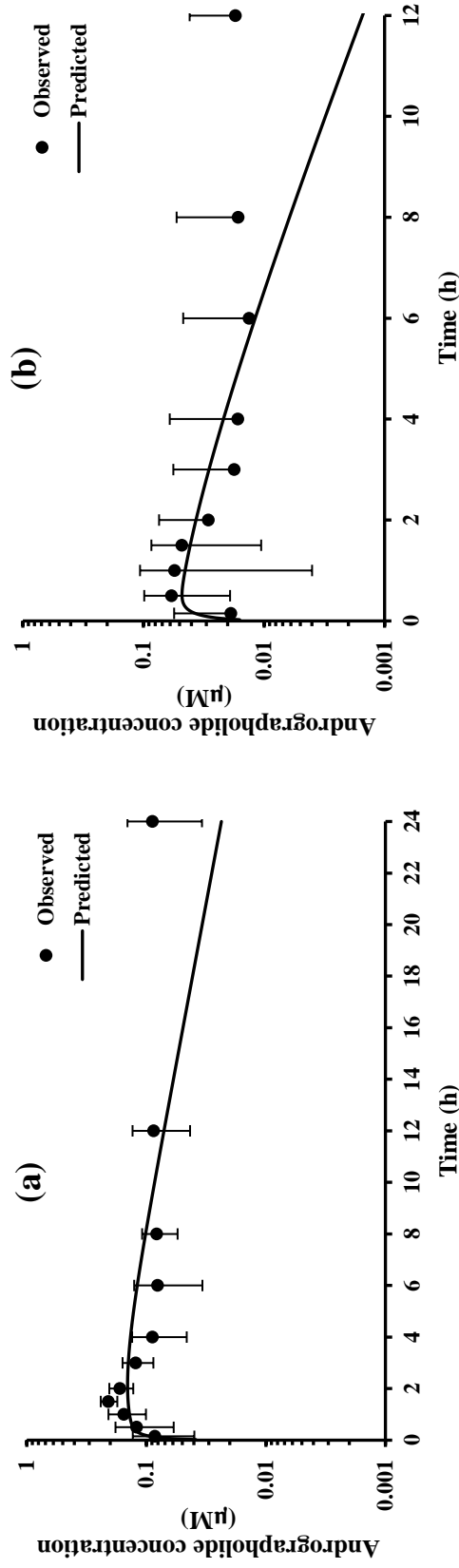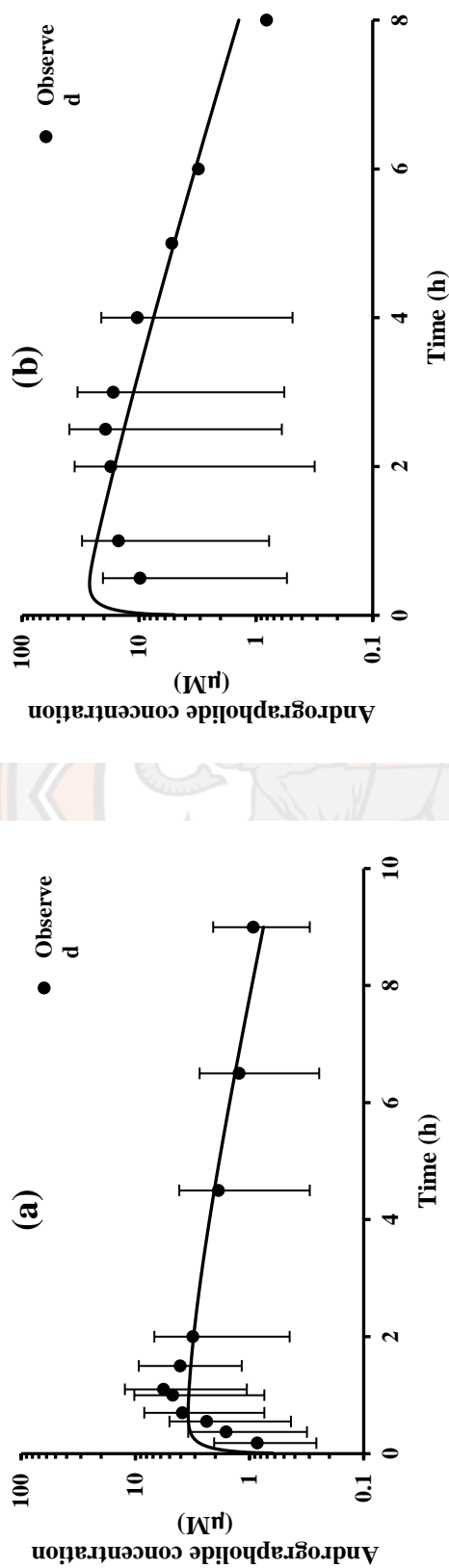
Figure 21 Predicted concentration-time profile in rat plasma following single oral administration at 25 mg/kg. • - observed data acquired from (a) Ren et al., 2009, and (b) Maiti et al., 2010, solid line- predicted data, error bar - standard deviation of the observed data
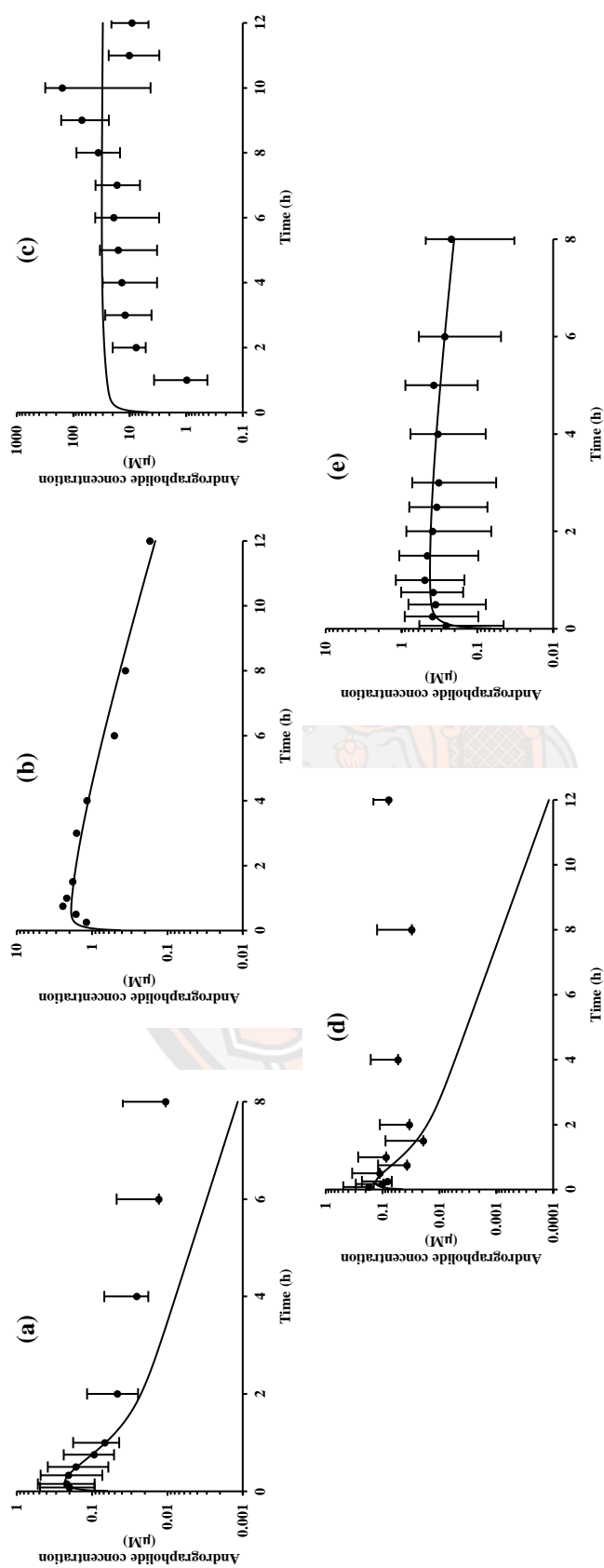
Figure 22 Predicted concentration-time profile in rat plasma following single oral administration at (a) 40 mg/kg, (b) 50 mg/kg, (c) 60 mg/kg, (d) 100 mg/kg, and (e) 300 mg/kg. • - observed data acquired from (a) Qiao et al., 2017, (b) Song et al., 2019, (c) Balap et al., 2016 (d) Yang et al., 2013, (e) Yen et al., 2020, solid line- predicted data, error bar - standard deviation of the observed data

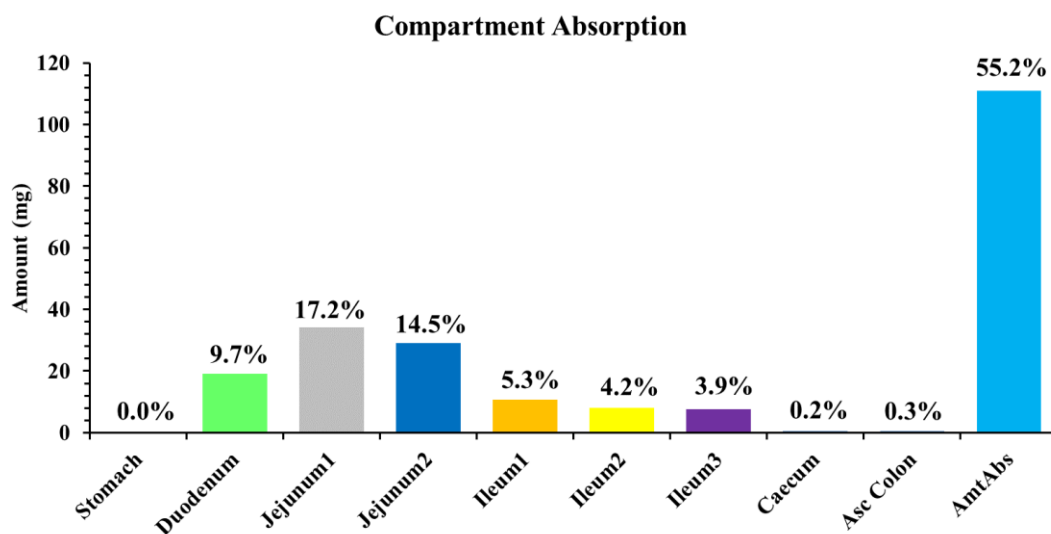**Figure 23 A generated bar graph by GastroPlus® software represents the amount of andrographolide that is absorbed in each human intestinal segment after single oral administration 200 mg of andrographolide**

Table 21 Estimated disposition and metabolism parameters used in PBPK model development

Modified liver structure model	Parameter (unit)	Estimated values (%CV)	AIC values
Perfusion-limited model	P_{Lu}	0.346 (5.0%)	250.72
	P_{Rp}	1.326 (595.0%)	
	P_{Sp}	0.424 (382.6%)	
	P_F	27.040 (8.3%)	
	P_{Li}	1.460 (10.1%)	
	V_{max} (μmol/h)	12.96 (2.7%)	
Permeability-limited model	P_{Lu}	0.316 (16.12%)	266.50
	P_{Rp}	3.244 (397.9%)	
	P_{Sp}	0.526 (603.9%)	
	P_F	21.11 (14.50%)	
	$f_{u,Li}$	0.872 (14.58%)	
	PA_{Li} (L/h)	1.000 (381.2%)	
	V_{max} (μmol/h)	7.493 (5.42%)	
Permeability-limited with binding tissue model	P_{Lu}	0.765 (25.38%)	258.92
	P_{Rp}	2.285 (64.20%)	
	P_{Sp}	1.285 (24.10%)	
	P_F	73.30 (22.83%)	
	$f_{u,Li}$	0.285 (15.25%)	
	PA_{Li} (L/h)	2.923 (1701.0%)	
	$k_{a,Li}$ (h^{-1})	54.50 (36.52%)	
	$k_{d,Li}$ (h^{-1})	3.052 (17.41%)	
	V_{max} (μmol/h)	5.117 (6.82%)	

P is partition coefficient tissue/plasma; $f_{u,T}$ is fraction unbound in tissue; PA is permeability surface area; k_a and k_d are constant values; V_{max} is the maximum velocity. The subscription following Lu, Li, Rp, Sp, and F are lung, liver, rapidly perfused organ, slowly perfused organ, and fat, respectively.

Table 22 Species chemical parameters used in model simulation in humans using GastroPlus® software

Description of parameters	Symbol	Humans	Method/Reference
Biochemical			
Log of partition coefficient between n-octanol and water	log P	2.51	This value was acquired from Megantara et al. (2016)
Log of partition of a chemical compound between the lipid and aqueous phases	log D	1.45[a]	This value was calculated based on an equation by Poulin et al. (2001)
Log of basic dissociation constant	pKb	-	This value was neglected because andrographolide has been considered as a neutral compound (Gao et al., 2021)
Partition coefficient tissue: blood			
Lung	P_{Lu}	6.32	
Fat	P_F	18.22	
Liver	P_{Li}	7.31	
Muscle	P_{Mus}	2.98	
Spleen	P_{Sl}	5.33	
Heart	P_{Hr}	3.89	These values were predicted based
Brain	P_{Br}	1.34	on equations from Lukacova et al.
Kidneys	P_{Kd}	7.95	using GastroPlus® software
Skin	P_{Sk}	2.45	
ReproOrg	P_{Re}	7.95	
Red marrow	P_{RM}	1.39	
Yellow marrow	P_{YM}	0.69	
Rest of body	P_{ROB}	5.33	
Protein binding			
Fraction unbound in plasma	f_{up}	0.45	This value was acquired from Panossian et al. (2000)
Blood to plasma ratio	R_{bp}	0.93	This value was acquired from Bera et al. (2014)
Metabolism parameters			
Intrinsic clearance (L/h)	CL_{int}	204.7[d]	This value was calculated based on V_{max}/K_m which is obtained from Tian et al. (2015)
Systemic clearance (L/h)	CL_{sys}	41.95	Predicted by GastroPlus® software
Absorption parameters			
Permeability in duodenum segment (cm/s)	$P_{eff, duo}$	$4.60*10^{-4}$	These values were scaled up

Description of parameters	Symbol	Humans	Method/Reference
Permeability in jejunum1 segment (cm/s)	$P_{eff, je1}$	$2.08*10^{-4}$	based on Gao et al. (2021) using
Permeability in jejunum2 segment (cm/s)	$P_{eff, je2}$	$2.08*10^{-4}$	equation follows; $P_{eff, human} =$
Permeability in ileum1 segment (cm/s)	$P_{eff, il1}$	$0.70*10^{-4}$	$3.6*P_{eff, rat} + 0.03*10^{-4}$
Permeability in ileum2 segment (cm/s)	$P_{eff, il2}$	$0.70*10^{-4}$	
Permeability in ileum3 segment (cm/s)	$P_{eff, il3}$	$0.96*10^{-4}$	
Permeability in caecum segment (cm/s)	$P_{eff, cae}$	$0.96*10^{-4}$	
Permeability in colon segment (cm/s)	$P_{eff, col}$	$0.18*10^{-4}$	

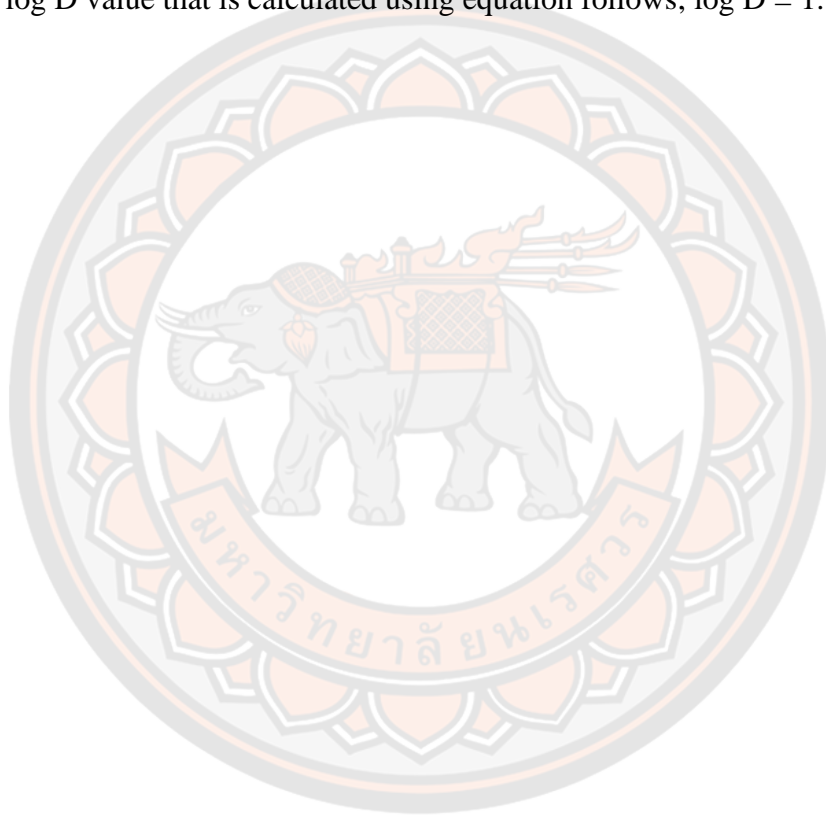[a] is the log D value that is calculated using equation follows; log D = 1.115*log P-1.35

Table 23 Values and distributions of parameters used in Monte Carlo analysis

Parameter	SYM	Distribution	Mean	SD	CV	1.0th	99.0th
Body weight (kg)		Lognormal	70.0	7.00	0.10	50.00	90.00
Fraction blood flow							
Rapidly perfused	Q_{RpC}	Normal	0.430[a]	0.073	0.17[e]	0.211	0.649
Slowly perfused	Q_{SpC}	Normal	0.291[a]	0.172	0.59[e]	0.024	0.806
Fat	Q_{FC}	Normal	0.052[a]	0.012	0.24[e]	0.015	0.089
Liver	Q_{LiC}	Normal	0.227[a]	0.050	0.22[e]	0.077	0.377
Fraction volume							
Lung	V_{LuC}	Normal	0.008[a]	0.001	0.13[e]	0.005	0.011
Rapidly perfused	V_{RpC}	Normal	0.093[a]	0.012	0.13[e]	0.057	0.129
Slowly perfused	V_{SpC}	Normal	0.580[a]	0.099	0.17[e]	0.284	0.876
Fat	V_{FC}	Normal	0.214[a]	0.064	0.30[e]	0.021	0.407
Liver	V_{LiC}	Normal	0.026[a]	0.004	0.16[e]	0.014	0.038
Venous	V_{VC}	Normal	0.059[a]	0.006	0.11[e]	0.040	0.078
Arterial	V_{AC}	Normal	0.020[a]	0.002	0.11[e]	0.013	0.027
Partition coefficient tissue: plasma							
Lung	P_{Lu}	Lognormal	0.346[b]	0.069	0.20[f]	0.190	0.502
Rapidly perfused	P_{Rp}	Lognormal	1.326[b]	0.265	0.20[f]	0.729	1.923
Slowly perfused	P_{Sp}	Lognormal	0.424[b]	0.085	0.20[f]	0.233	0.615
Fat	P_F	Lognormal	27.04[b]	5.408	0.20[f]	14.87	39.21
Liver	P_{Li}	Lognormal	1.460[b]	0.292	0.20[f]	0.584	2.117
Protein binding							
Fraction unbound in plasma	f_{up}	Lognormal	0.450	0.135	0.30[f]	0.045	0.855
Blood to plasma ratio	R_{bp}	Lognormal	0.930	0.279	0.30[f]	0.874	0.986
Metabolism parameters							
Maximum velocity (µmol/h)	V_{max}	Lognormal	626.5	187.9	0.30[f]	62.65	1190.4
Binding affinity (µmol/L)	K_m	Lognormal	3.06	0.918	0.30[f]	0.306	5.814
Absorption parameters							
Absorption rate constant (h⁻¹)	k_a	Lognormal	0.245[b]	0.074	0.30[f]	0.025	0.466
Fraction dose reaching the hepatic portal	F_{Dp}	Lognormal	0.170[c]	0.051	0.30[f]	0.017	0.323
vein	F_{Dp}	Lognormal	0.137[d]	0.041	0.30[f]	0.014	0.260

[a] is the mean values of physiological parameters obtained by Brown et al., 1997

[b] is the values obtained the developed PBPK model

[c] is the value obtained by the GastroPlus® software at the dose of 60 mg

[d] is the value obtained by the developed PBPK model at the dose of 200 mg

[e] is the CV of all physiological parameter values were suggested by Price et al., 2003

[f] is the CV of partition coefficient and other chemical specific parameter values were suggested by Li et al., 2017

Table 24 The estimated oral bioavailability, absorption constant, and oral clearance from different pharmacokinetics studies in rats

Blood simple techniques	Anesthetic agent	Anesthesia used	CL/F	Estimated			Author (published year)
				F_{oral}	F_{Dp} (%CV)	k_a in h^{-1} (%CV)	
Retro orbital plexus	Ether (light)	Inhalation	0.040	217.3	456.2 (4667%)	0.002 (4714%)	Balap et al. (2006)
Jugular vein blood sample collection	Ether	Inhalation	0.170	2.652	5.568 (13.4%)	0.606 (19.9%)	Maiti et al. (2010)
Tail vein blood sample collection	NA	Local	0.330	0.867	1.821 (15.7%)	0.333 (22.1%)	Parveen et al. (2014)
Tail vein blood sample collection	NA	Local	0.590	0.604	1.268 (15.3%)	0.301 (20.1%)	Ren et al. (2009)
Retro orbital puncture technique	Ether (mild)	Inhalation	1.010	0.359	0.754 (15.1%)	0.630 (21.7%)	Chellampillai et al. (2011)
Retro orbital puncture technique	NA	NA (G/I)	1.580	0.222	0.467 (15.0%)	0.078 (18.3%)	Xu et al. (2016)
Retro orbital puncture technique	NA	NA (G/I)	1.980	0.059	0.124 (24.6%)	0.146 (33.1%)	Ma et al. (2018)
Retro orbital puncture technique	NA	NA (G/I)	2.900	0.133	0.280 (6.5%)	0.358 (8.9%)	Song et al. (2019)
Jugular vein blood sample collection	NA	NA	9.560	0.001	0.002 (23.2%)	3.284 (39.5%)	Yang et al. (2013)
Retro orbital puncture technique	NA	NA (G/I)	9.940	0.007	0.015 (19.2%)	0.538 (30.4%)	Chen et al. (2018)
Jugular vein cannulation	-	Not use	13.56	0.022	0.046 (20.9%)	1.225 (24.4%)	Chen et al. (2014)
Jugular vein cannulation	-	Not use	34.96	0.009	0.018 (11.2%)	0.209 (15.6%)	Yen et al. (2020)
Jugular vein cannulation	-	Not use	41.00	0.012	0.025 (7.4%)	0.616 (11.0%)	Yen et al. (2018)
Retro orbital puncture technique	NA	NA (G/I)	61.45	0.009	0.018 (8.4%)	0.921 (12.0%)	Ye et al. (2011)
Retro orbital puncture technique	NA	NA (G/I)	79.35	0.003	0.007 (3.9%)	3.802 (7.0%)	Qiao et al. (2017)

F_{oral} is the fraction of andrographolide orally absorbed; F_H (0.476) is the fraction of andrographolide that escaped hepatic first-pass metabolism; F_{Dp} is fraction andrographolide reaching the hepatic portal vein; E_H (0.524) is hepatic extraction ratio; k_a is absorption constant; CL/F is oral clearance calculated by non-compartment analysis, NA is Not data available, G/I is general anesthesia or inhalation anesthesia.

Table 25 Comparison of the predicted fraction of dose absorbed (F_A), the fraction of dose reaching the portal vein (F_{Dp}), the fraction of dose escaping hepatic first-pass metabolism (F_H), and oral bioavailability (F_{oral}) values at different dosages of andrographolide using GastroPlus® software

Dose (mg)	F_H	F_{Dp}	F_A	F_{oral}
Predicted by the GastroPlus® software				
20	0.455	0.185	0.783	0.084
60	0.455	0.170	0.722	0.077
100	0.455	0.156	0.666	0.071
200	0.455	0.128	0.552	0.058
300	0.455	0.109	0.466	0.050
1000	0.455	0.054	0.231	0.024
10000	0.455	0.008	0.036	0.004
Predicted by the developed PBPK model				
200	0.462	0.137	NA	0.063

F_H value is calculated by F_{oral}/F_{Dp}
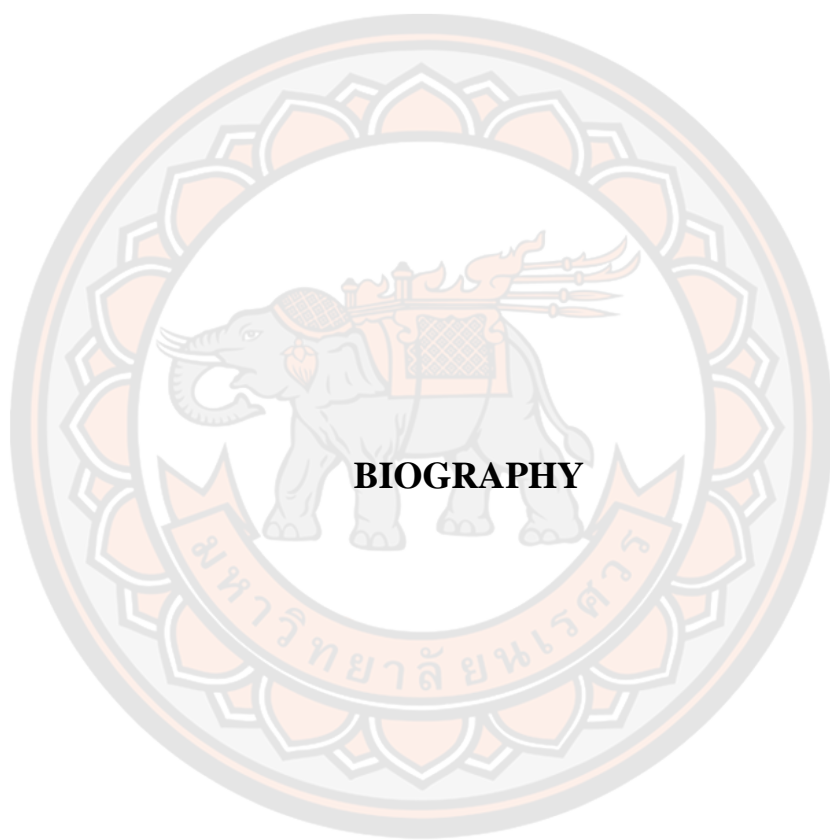
BIOGRAPHY

BIOGRAPHY

Name-Surname   Taman Talapphetsakun

Date of Birth

Address

Work Experience   2017 - 2019 Royal Thai Massage for Therapy
                        301/59 Moo.7 Tha Pho, Mueang Phitsanulok,
                        Phitsanulok 65000

Education Background   2015   B.S. (Applied Thai Traditional Medicine)
                                 Mae Fah Luang University